UNIVERSITÀ DELLA CALABRIA

Dipartimento di Ingegneria Civile

Dottorato di Ricerca in
INGEGNERIA CIVILE E INDUSTRIALE
XXXI CICLO

EXPERIMENTAL AND NUMERICAL MODELING OF SOLITARY WAVE LOADS ON HORIZONTAL CIRCULAR CYLINDERS

SSD ICAR/02

Coordinatore: **Prof. Ing. Franco Furgiuele**

Supervisore: **Ing. Francesco Aristodemo**

Dottorando: **Ing. Giuseppe Tripepi**

– Novembre 2018 –

ai miei genitori,
ai miei nonni

Ringraziamenti

Sommario

L A tesi di dottorato è stata sviluppata attraverso uno studio sperimentale e numerico delle forze idrodinamiche orizzontali e verticali indotte da onde solitarie su un cilindro sommerso ad asse orizzontale.

I test di laboratorio sono stati effettuati presso il canale ondogeno del Laboratorio Grandi Modelli Idraulici (GMI) del Dipartimento di Ingegneria Civile dell'Università della Calabria. Nella fase di progettazione del modello fisico, sono stati posizionati una serie di trasduttori di pressione in corrispondenza della superficie esterna del cilindro. Inoltre, sono state installate quattro sonde resistive per misurare l'elevazione della superficie libera in prossimità del cilindro. Per verificare il corretto spostamento del generatore d'onda si è inserito un sensore ad ultrasuoni dietro la pala ondogena. I test di laboratorio sono stati eseguiti variando gli attacchi ondosi e la posizione verticale del cilindro rispetto al fondo. Complessivamente, considerando tutti gli affondamenti esaminati, sono stati effettuati un totale di 134 test sperimentali.

Le simulazioni numeriche sono state invece effettuate utilizzando due diversi modelli. Esse, a differenza dei test sperimentali, hanno permesso di studiare in dettaglio il campo di moto vicino al cilindro e di estendere i campi di misura sperimentale. Il primo è un modello SPH per fluido debolmente comprimibile. Al fine di migliorare i risultati numerici ed evitare campi di moto spuri nei pressi del cilindro, un cosiddetto algoritmo di *packing* è stato adoperato per inizializzare le particelle lagrangiane del modello SPH. La componente acustica del campo di pressione numerico è stata filtrata utilizzando la trasformata Wavelet. Il modello lagrangiano SPH è stato adoperato solo per il primo affondamento, quello in cui il cilindro è posizionato a metà profondità rispetto al tirante idrico. L'alto onere computazionale del modello SPH ha indotto l'utilizzo di un secondo modello numerico. Il modello utilizzato per confrontare i risultati sperimentali per gli altri affondamenti è il modello open source OlaFlow. Dopo aver validato i modelli numerici, è stato possibile allargare l'intervallo di calcolo effettuando simulazioni aggiuntive. Considerando l'intero dataset, sono state effettuate un totale di 176 simulazioni numeriche.

Il buon accordo tra le forze sperimentali e numeriche e il campo cinematico indisturbato in corrispondenza dell'asse trasversale del cilindro hanno permesso la corretta

calibrazione dei coefficienti idrodinamici nelle equazioni semi-empiriche di Morison e trasversale attraverso diversi metodi nel dominio del tempo. La tesi inoltre presenta un metodo alternativo (Gurnari e Filianoti, 2017) per stimare la forza idrodinamica orizzontale. Tale metodo si basa sul concetto che un'onda solitaria, passando sul cilindro, rallenta la propria velocità. La corretta applicazione di tale modello è possibile dopo la calibrazione del cosiddetto fattore di rallentamento. Nel presente lavoro di tesi, viene proposta una nuova formulazione del metodo semi-analitico trasversale utilizzando una formula diversa per il calcolo della forza di lift. Tale formulazione risulta efficace per stimare in modo corretto il picco della forza verticale per due affondamenti del cilindro prossimi al fondo. Le analisi sperimentali e numeriche hanno mostrato il confronto tra gli andamenti temporali delle forze sperimentali e numeriche per ogni affondamento considerato di due test rappresentativi. Globalmente, sono stati analizzati i picchi di forza in funzione delle diverse ampiezze dell'onda solitaria. Sono stati analizzati inoltre i contributi delle singole componenti di forza rispetto ai valori massimi della forza orizzontale e verticale. Le variazioni nel tempo della forza orizzontale sperimentale sono state confrontate con la soluzione di Gurnari e Filianoti (2017) per i casi estremi esaminati (cilindro a metà profondità e cilindro sul fondo). Il confronto tra gli esperimenti e l'equazione di Gurnari e Filianoti (2017) è stato effettuato in relazione ai picchi di forza orizzontale per tutti i test relativi ai due affondamenti precedentemente menzionati.

Abstract

THE present thesis deals with an experimental and numerical study on the horizontal and vertical hydrodynamic forces induced by solitary waves on submerged horizontal circular cylinders.

Laboratory tests were performed in the wave flume of the University of Calabria. A battery of pressure transducers was mounted along the external contour of a cylinder while four wave gauges were located close to the cylinder. The correct displacement of the wavemaker was checked by an ultrasonic sensor located behind the paddle. A number of 134 experimental tests were conducted in the wave channel taking into account different wave attacks and five depths of the cylinder location ranging between half water depth and the bottom of the flume.

From the numerical viewpoint, two different numerical models were adopted. The first one is the diffusive weakly-compressible Smoothed Particle Hydrodynamics (SPH) model. To improve the results and prevent spurious flows near the cylindrical contour, a packing algorithm has been applied to initialize the SPH fluid particles. The acoustic components occurring in the numerical pressure field were filtered through the application of Wavelet Transform. The numerical simulations provided to investigate in detail the flow field near the cylinder not modeled by the laboratory investigation. This Lagrangian model was used only in the case where the cylinder was placed at half water depth. The high time consuming of the SPH simulations led to adopt another numerical approach. In this context, the Eulerian OlaFlow model was used to investigate the other four depths of the cylinder. With respect to the experimental tests, additional numerical simulations were performed to extend the range of the analysis. Considering all the five positions of the cylinder, a total of 176 numerical simulations were carried out.

The good agreement between experimental and numerical forces and kinematics at the cylinder has allowed the calibration of the hydrodynamic coefficients in the Morison and transverse semi-empirical equations by different time-domain methods. The present thesis has showed an alternative method (Gurnari and Filianoti, 2017) to assess the horizontal forces. Based on the concept that a solitary wave is subjected to a slowdown passing over the cylinder, this formulation was used after the experimental calibration of the speed drop factor. In this work, an extension of the transverse for-

mulation which considered a new form of the lift force was also presented. For two specific depths, this formulation resulted necessary to model correctly the peaks and the phase shifts of the vertical forces.

The experimental and numerical analysis were presented comparing the time variation of the experimental and numerical simulations for two test cases at each depth. The overall analysis of the peaks forces was evaluated as a function of the wave amplitude. In addition, the weight of the different force components, i.e. drag, lift and horizontal and vertical inertia, was evaluated and analyzed with respect to the maximum values of the horizontal and vertical force. The time variation of the horizontal forces calculated by the Gurnari and Filianoti (2017) solution was compared with the experimental ones for the two vertical extreme positions of the cylinder. The comparison between the experimental and the Gurnari and Filianoti (2017) equation was performed in relation to the horizontal force peaks.

Contents

Introduction

1.1   Solitary waves and cylindrical structures in marine environment

Recent catastrophic events, such as those that occurred in the Indian Ocean and Japan a few years ago, brought increasing attention of the scientific community to analyze the tsunami properties and their interaction with structures.

Tsunamis are very long waves that are principally generated by earthquakes, landslides or volcanic eruptions. These waves propagate with high celerity across the ocean for long distances. In deep waters, the wavelength of a tsunami can reach hundreds of kilometers with speeds higher than 800 km/h. The wave height, that in deep ocean is usually lower than one meter, grow up when the wave approaches the shoreline. The shoaling effect reduces the speed of the wave and increase the wave height. Tsunami waves have an enormous energy, indeed they can penetrate inland for a long distance, erode sediments from the seafloor, cause loss of life and produce damages to the coastal and marine infrastructures (Fig. 1.1).

In this context, in the present thesis the attention is focused to study the interaction between tsunami waves and a particular type of marine structures, the horizontal cylindrical ones. The horizontal cylindrical bodies are abundantly present in the marine environment in the offshore platforms that usually are employed in oil industry, in platforms for broadcasting, radar surveillance, space operations and oceanographic research. Over the past few decades, with the development of marine engineering, several types of offshore facilities and marine pipelines have had a rapid growth (Fig. 1.2). Moreover, another horizontal cylindrical structure, which has recently attracted the interest of many researchers, is the Submerged Floating Tunnels (SFT) (e.g., [68], [66]). This tunnel is an innovative concept for crossing waterways, utilizing the law of buoyancy to support the structure at a moderate depth. Nowadays, this structure, known as Archimedes bridge, has never been used before even for small length but recently
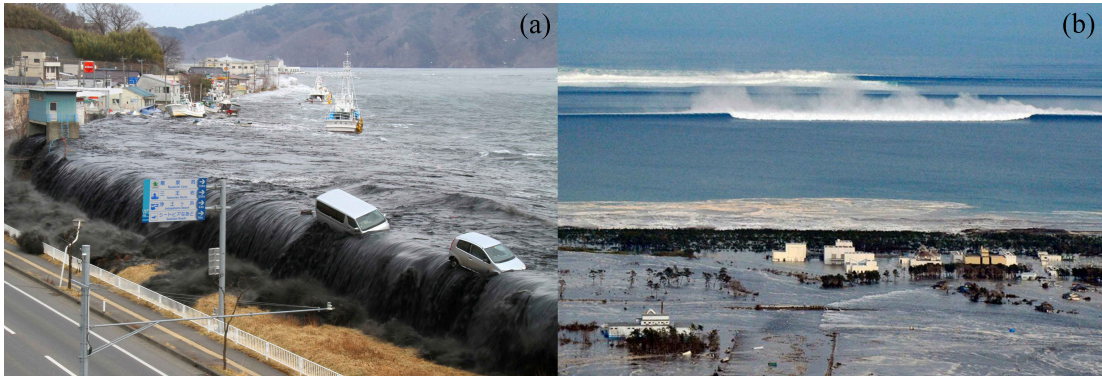
Figure 1.1: *Tsunami in Japan 2011.*

engineers seem to agree that this elegant solution offers answers to specific problems, such as that of Norwegian fjords (Fig. 1.3).

The occurrence of tsunami events in coastal areas is a source of additional risk for already-vulnerable marine structures subjected to the action of wind waves and/or currents. Hence, the stability of marine structures under tsunami action depends on the accurate assessment of the hydrodynamic forces. The reproduction of catastrophic tsunami waves was observed to be dependent upon the magnitude of the specific source, and the resulting shapes of surface elevation can be quite different to lead to a generalized modeling of tsunami waves (e.g., [22, 64]). Owing to its robust and suitable approach, the modeling of the leading wave of a tsunami event is usually reproduced by the generation of solitary waves both experimentally (e.g., [60]) and numerically (e.g., [80]). Indeed, if the tsunami in the open ocean has approximately a sinusoidal shape, it become more peaked when tsunami waves approach the coast. As a result, the wave trough disappears and only a positive peak remains. However, the simulation of tsunami-like waves can also be performed for instance by bores characterized by unsteady flow fields (e.g., [76]) or by rigid or deformable bodies falling into water masses (e.g. [22]).
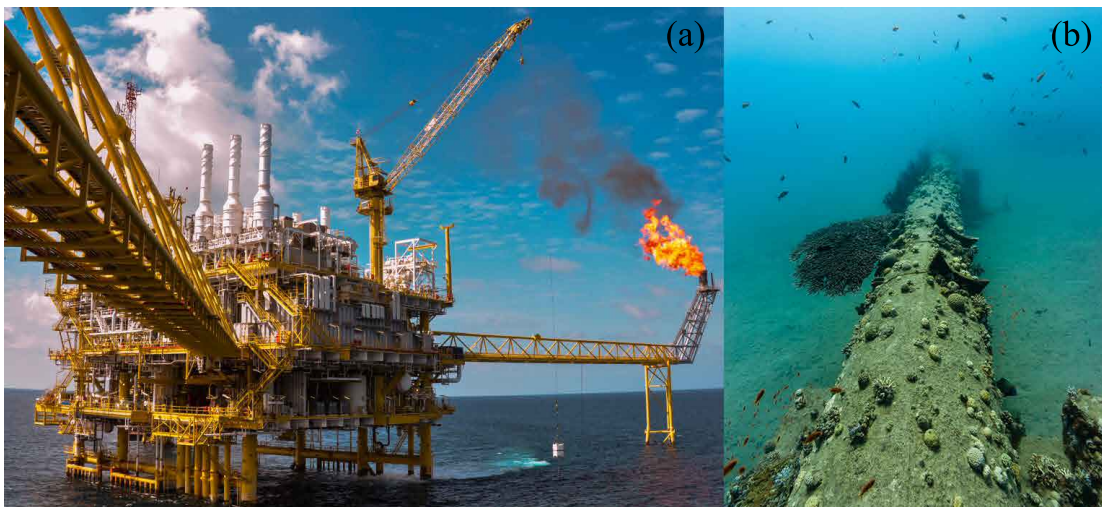
Figure 1.2: *(a) Offshore platform; (b) submarine pipeline.*

Several numerical and experimental studies have been performed to analyze the interaction between solitary waves and structures in marine environment such as breakwaters [45], bottom-mounted rectangular blocks [26] or flat plates [65]. In the case of cylindrical structures, the flow field generated by the presence of a semi-circular cylinder placed on the bed was analyzed by Gsell et al. [31] through the coupling of VOF with IBM approaches. A FEM model was developed by Zhao et al. [82] to investigate the solitary wave scattering by a circular cylinder array and by Sun et al. [72] to study the impact of solitary waves at single and twin vertical rectangular cylinders. Even if many analytical, numerical and experimental approaches have been presented in literature for horizontal circular cylinders subjected to current flows or regular and irregular waves (see, e.g., the comprehensive books of Sarpkaya and Isaacson [62] and Sumer and Fredsoe [69]), little attention was addressed to the case of solitary waves. For bottom-mounted cylinders under the above kind of incident flows, i.e. currents and wind waves, values of hydrodynamic coefficients in Morison-type equations (e.g., [54]) were deduced from field tests [30] as well as small- and large-scale laboratory experiments, and for wide ranges of Keulegan–Carpenter (KC) and Reynolds (Re) numbers [5, 7, 14, 16, 17, 55, 63]. More complex models as compared to Morison-type ones and dealing with an improved description of flow-cylinder interaction processes have been also developed [6].

A first pioneering work on solitary waves acting on horizontal cylinders refers to the experimental investigation performed by Sibley et al. [67] where the solitary wave was reproduced manually using a rigid vertical barrier. Consequently, a well-defined assessment of only horizontal hydrodynamic forces was lacking in the above study. Regarding numerical studies, Xiao et al. [81] have analyzed a solitary wave hitting a horizontal cylinder located just below the free surface by a VOF model, while Lin and Liao [43] used a vortex method to simulate the interaction of solitary waves with a horizontal cylinder located near the bed. The latter study was restricted to a unique forcing by changing only the distance of the cylinder from the bottom.

Figure 1.3: *Rendering of the Submerged Floating Tunnels by Norwegian Public Road Administration.*

1.2 Structure of the contents

The contents of the thesis are presented in the following way. In chapter 2, the adopted equations to reproduce a solitary wave in the flume are recalled. Here, it is shown the time variation of the surface elevation, the free steam kinematic field at the transversal axis of the cylinder and the law to generate a solitary wave

In chapter 3, a review of the hydrodynamics around the horizontal circular cylinder is illustrated. Specifically, this chapter describes the near flow field induced by regular, irregular and solitary waves. In this section, the classical Morison and transverse semi-empirical equations to calculate the horizontal and vertical hydrodynamic forces are introduced. An alternative equation called GF2017, based on the concept that a solitary wave is subjected to a slowdown passing over the cylinder, is presented in order to calculate the horizontal loads. In addition, an extension of the transverse formulation which considers a new form of the lift force is proposed.

In chapter 4 the experimental campaign in a wave channel to study the solitary wave forces on a horizontal cylinder is described. The hardware/software instrumentation, the experimental setup and the characteristics of the laboratory tests are presented in this section. Chapter 4 also indicates all the details to calculate the experimental hydrodynamic forces from the dynamic pressure deduced by the transducer records.

Chapter 5 illustrates two different numerical approaches to support and extend the experimental research and investigate the near flow field not modeled by the laboratory investigation. The first numerical model adopted to reproduce the interaction between the cylinder and the solitary waves is the Lagrangian meshless method Smoothed Particle Hydrodynamics (SPH). To prevent spurious flows near the cylindrical contour, a packing algorithm is applied to initialize the Lagrangian fluid particles. The acoustic components occurring in the numerical pressure field are filtered through the application of Wavelet Transform. The other numerical model used in the present thesis is the free and open source Eulerian method OlaFlow.

Finally, chapter 6 describes the numerical and experimental results on the features of horizontal and vertical forces at the horizontal cylinder for the action of solitary waves, the resulting near flow field, the calibration of the hydrodynamic coefficients in the Morison and transverse models as well as in the GF2017 scheme and their application to analyze the effect of drag, inertia and lift force components. Five different depths of the cylinder are evaluated both experimentally and numerically. The analysis of the interaction between solitary wave and horizontal cylinder concerns 134 experimental tests and 176 numerical simulations. Indeed, additional numerical simulations are performed to extend the range of the analysis.

Theory of solitary waves

2.1 Introduction

Although some differences have been highlighted in simulating tsunami-like waves in coastal waters [57], the reproduction of a leading wave of a tsunami event is commonly performed through the generation of solitary waves both through laboratory experiments (e.g., [60]) and numerical simulations (e.g., [80]). The use of solitary waves is due to the strong analytical background of this theory.

The solitary wave is represented as a single elevation of water above the undisturbed water level which propagates without changing its shape in a plane channel, as represented in the xz domain of Fig. 2.1, in which η is the surface elevation, A is the wave amplitude, d is the depth and c is the celerity.
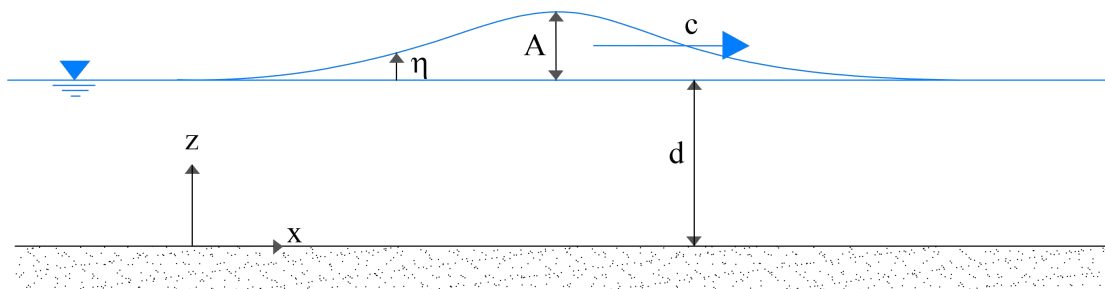
Figure 2.1: *Sketch of solitary wave in constant water depth.*

In 1834, solitary waves were first identified by John Scott Russell. The Scottish en-

gineer, while conducting his experiments in hydrodynamics, discovered this new phenomenon that he called "Wave of Translation". In 1845, he generated solitary waves in a long narrow water flume. After the experimental investigation, Russel obtained a relationship between the water depth, the celerity and the wave amplitude [61]:

$$c = \sqrt{g(d + A)} \tag{2.1}$$

The extensive investigation conducted by the author directed him to discover some characteristics of the solitary wave. He noticed, as expressed in Eq. 2.1, that the celerity depends on the size of the wave. Moreover, Russel observed that the solitary waves which cross each other do not change their shape but undergo a phase shift.

In those years, his contemporaries did not understand the importance of his experiments because seemed in contrast with the classical theories of hydrodynamics. Only in the 1871, Joseph Boussinesq published the first mathematical theory to support Russell's experimental observation [11], and in 1877 introduced the KdV equations [12]. In 1876, Lord Rayleigh in his work [59] mentioned Scott Russell's name and also admitted that the first theoretical treatment was by Joseph Boussinesq. Some years later, in 1876, Korteweg and de Vries assumed that the wave was independent of the cross-channel direction and also that the horizontal current was independent of the depth [41]. The authors obtained a non-linear equation to describe the Russell's experiments. This work, although was not the first theoretical treatment of this subject, represents a significant event in the history of the development of soliton theory.

2.2 Surface elevation

Boussinesq [11] and Rayleigh [59] showed that the surface elevation, η, is equal to:

$$\eta(t) = A sech^2(\beta ct/2) \tag{2.2}$$

where β represents the outskirts decay coefficient and c is the wave celerity. The value of the outskirts decay coefficient changes in the different historical approaches (e.g., [11] [59] [29]). In according with the Boussinesq theory, Goring [29] defines the outskirts decay coefficient as:

$$\beta_B = 2\sqrt{\frac{3A}{4d^3}} \tag{2.3}$$

The Rayleigh formulation is slightly different and the β coefficient is evaluated as:

$$\beta_R = 2\sqrt{\frac{3A}{4d^2(A + d)}} \tag{2.4}$$

The value of β_R is smaller than β_B and this involves more volume of water in the wave. The comparison between the different surface elevation formulas are shown in Fig. 2.2

In addition, the β coefficient is linked also with the wave number, k, through the following relationship:

$$\beta = 2k \tag{2.5}$$
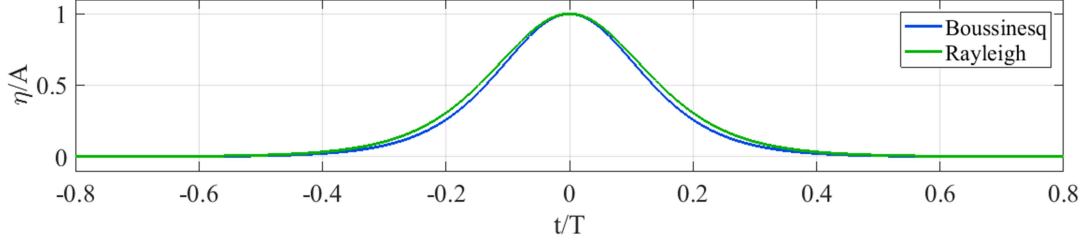
Figure 2.2: *Surface elevation. Comparison between Boussinesq and Rayleigh formulation for a representative test case (A/d = 0.175).*

The length of a solitary wave is theoretically infinite, so it is necessary to define an apparent wave length, $L = 2\pi/k$. The apparent wave length is deduced considering that at a distance of $L/2$ away from the wave crest, the value of η is reduced to 1% of its maximum value (e.g., [23]). Note that other heuristic approaches to define the finite wave length (e.g., [46]) lead to negligible differences in defining a finite time window to study the investigated phenomenon, i.e. the wave forces induced by solitary waves on horizontal circular cylinders. In this context, an apparent wave period is then defined as $T = L/c$.

2.3 Kinematic field

In accordance with the Rayleigh's theory and for $A/d < 0.25$, the values of horizontal, u, and vertical, v, velocity are determined as follows (e.g., [42]):

$$
\begin{cases}
\frac{u(t)}{c} = \left\{ \frac{A}{d} + 3\left(\frac{A}{d}\right)^2 \left[\frac{1}{6} - \frac{1}{2}\left(\frac{z}{d}\right)^2 \right] \right\} \frac{\eta(t)}{A} \\
\qquad - \left(\frac{A}{d}\right)^2 \left[\frac{7}{4} - \frac{9}{4}\left(\frac{z}{d}\right)^2 \right] \left(\frac{\eta(t)}{A}\right)^2 \\
\frac{v(t)}{c} = \sqrt{3\frac{A}{d}} \left(\frac{z}{d}\right) \left(\frac{\eta(t)}{A}\right) tanh\left(-\sqrt{\frac{3A}{4d}}\frac{ct}{d}\right) \\
\qquad \left\{ 1 + \frac{A}{2d}\left[1 - \frac{7\eta(t)}{A} - \left(\frac{z}{d}\right)^2\left(1 - \frac{3\eta(t)}{A}\right) \right] \right\}
\end{cases}
\tag{2.6}
$$

where z is the vertical coordinate taken from the bottom (see Fig. 2.1). The time variation of the horizontal an vertical velocities are shown in Fig. 2.3 for the representative test case $A/d = 0.175$ and $z = 0.2$ m.

It is worth noting that Eqs. 2.6 represent a second-order solution which provides for a small velocity gradient along the depth. By considering the mentioned apparent wave length, this is in agreement with finite water depth conditions close to shallow ones which will be reproduced both experimentally and numerically. The undisturbed kinematic field at the transversal cylinder axis will be successively adopted in semi-empirical formulas for the calibration of the hydrodynamic coefficients to assess the wave forces well. With reference to a value of $z = 0.2$ m, the values of the horizontal acceleration, a_H, and the vertical acceleration, a_V, are respectively derived from u and v and displayed in Fig. 2.4.
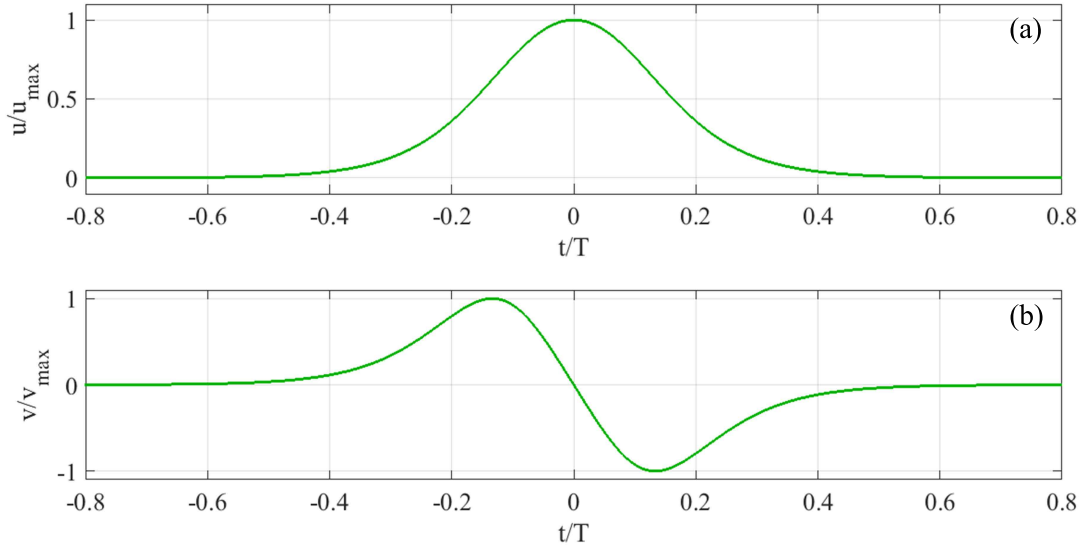
Figure 2.3: *Time variation of free stream kinematic field for A/d = 0.175. (a) Horizontal velocity, u; (b) Vertical velocity, v .*
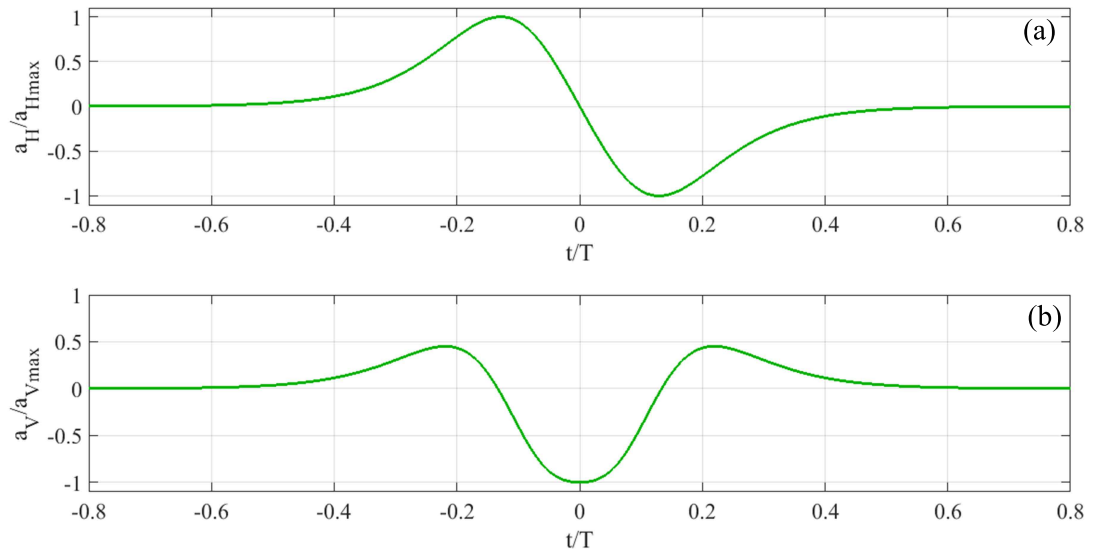
Figure 2.4: *Time variation of free stream kinematic field for A/d = 0.175. (a) Horizontal acceleration, a_H; (b) Vertical acceleration, a_V.*

2.4   Generation at laboratory scale

The first experiments were performed by Russell [61], who generated solitary waves by allowing a square block to fall into the water. Many years later, Daily and Stephan [21] obtained a solitary wave moving in vertical direction a piston rising from the bottom of the tank. The first studies in which the solitary wave was generated using a piston-type wavemaker were performed by Goring [29]. The classical procedure for solitary wave generation consists in matching the paddle velocity at each position in time with the vertically averaged horizontal velocity of the wave. From a mathematical viewpoint, this is expressed as:

$$dX/dt = \bar{u}(X, t) \tag{2.7}$$

where X is the paddle displacement and $\bar{u}$ is the average velocity over the depth. Rearranging Eq. 2.7 after a change of variables from x,t to $\theta = ct\text{-}X$, t, we obtain:

$$dX/d\theta = \frac{\bar{u}((\theta(X))}{c - \bar{u}((\theta(X))} \tag{2.8}$$

In according to the Boussinesq [11] and Rayleigh [59] solitary wave theory, the depth-averaged horizontal velocity has the form:

$$\bar{u}(\theta) = \frac{c\eta(\theta)}{d + \eta(\theta)} \tag{2.9}$$

Integrating Eq. 2.8 with Eqs. 2.2 and 2.9, the paddle motion of the piston-type wavemaker suitable to reproduce a solitary wave follows the expression [32]:

$$X(t) = \frac{2A}{\beta d} tanh\{\beta[ct - X(t)]/2\} \tag{2.10}$$

The total stroke of the paddle S can be deduced analytically from Eq. 2.10 and is equal to:

$$S = \frac{4A}{\beta d} \tag{2.11}$$

After the truncation of the infinite theoretical law of motion, the duration τ of the paddle displacement can be written as:

$$\tau = \frac{4}{\beta c} \left(tanh^{-1}(0.999) + \frac{A}{d} \right) \tag{2.12}$$

Goring [29], in his research, first addressed the problem of the minimizing trailing waves in solitary wave generation. Usually, after the passage of the solitary wave, spurious non-linear oscillations are observed in the wave flume. The author adopted the procedure based on the Boussinesq theory and by referring Eqs. 2.1 and 2.3 obtained the following simplified paddle law motion:

$$X_B(t) = S_G tanh \left[7.6 \left(\frac{t}{\tau} - \frac{1}{2} \right) \right] \tag{2.13}$$

where the total stoke of the paddle results:

9

$$S_G = 4\sqrt{\frac{Ad}{3}} \tag{2.14}$$

Guzien and Barthelemy [32], with the aim to generate a solitary wave as pure as possible, used Rayleigh theory to reproduce this wave along a plane channel. The purpose of the researchers was to minimize the trailing waves but also to generate a wave with a stable amplitude during its propagation. Their study showed that, using the Rayleigh theory, the reproduced solitary wave was higher and moved faster than the Boussinesq generated waves [32]. The total stroke of the paddle for the Rayleigh theory is given by:

$$S_R = 4\sqrt{\frac{A(A+d)}{3}} \tag{2.15}$$

while the paddle position X_R is expressed by Eq. 2.10 where the outskirts decay coefficient is β_R. For small displacements, after linearization, the paddle position can be assumed as:

$$X_R(t) = \frac{2A}{d\beta_R} \frac{d\,tanh(\beta_R ct/2)}{d + A\left[1 - tanh^2(\beta_R ct/2)\right]} \tag{2.16}$$

In the present thesis, the non-linear form of the horizontal motion law deduced by the Rayleigh's solution is chosen to reproduce the solitary wave (see Eq. 2.10). The time law of the horizontal displacement of the wavemaker for a representative test case (A/d = 0.175) is illustrated in Figure 2.5 where the time $t_X = 0$ corresponds to a wavemaker displacement $X = S/2$.
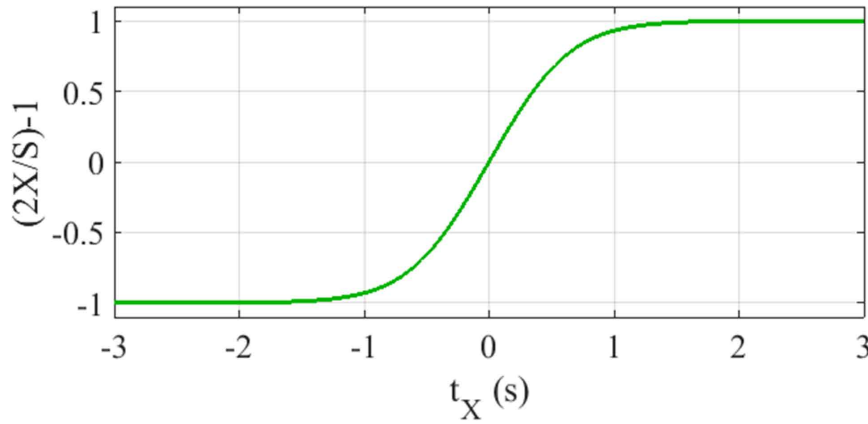
Figure 2.5: *Time law of horizontal displacement of wavemaker, X, for A/d = 0.175.*

Horizontal circular cylinders

3.1 Hydrodynamics around horizontal circular cylinders

The hydrodynamic aspects for a circular cylinder subject to wave action are essential for the definition of the flow field. The oscillatory flow changes the trajectory and overtakes the obstacle when meets a cylinder. When the flow shows not negligible velocities, patterns of vortices are present in the wake region. The vortex formation in this context is very important to understand the physical problem and assess the hydrodynamic forces. In the shallow ($d/L < 0.04$) and intermediate ($0.04 < d/L < 0.5$) waters, where d is the water depth and L the wave length, the effect of the wave motion occurs for the entire depth. Indeed, for the deep waters ($d/L > 0.5$), the flow field around the cylindrical structures placed on the bottom derive from the high hydrostatic pressure. In this section a brief recall of the hydrodynamics around the circular cylinder will be presented.

3.2 Near flow field induced by regular waves

The flow field induced by waves on cylindrical structures depends on the values of two non-dimensional parameters, the Reynolds number, Re, and the Keulegan-Carpenter number, KC. These parameters are defined as:

$$Re = \frac{u_{max}D}{\nu} \tag{3.1}$$

$$KC = \frac{u_{max}T}{D} \tag{3.2}$$

in which u_{max} is the maximum velocity, T is the period of the oscillatory flow, D is the diameter of the cylinder and ν is the kinematic viscosity of the fluid. Low values of

KC number mean that the orbital motion of the water particles is small in comparison with the total width of the cylinder. When KC number is large, the water particles travel quite big distances related to the diameter of the cylinder. So, for a low KC number, separation behind the cylinder may not even occur. Instead, for a large KC the flow results in separation and subsequent vortex shedding. In Figure 3.1 Sumer and Fredsoe [69] summarize the changes occurring in the flow as the KC number is increased from zero. In this case, the value of the Re number is 10^3.
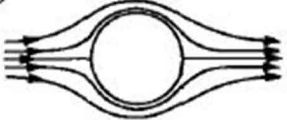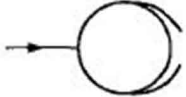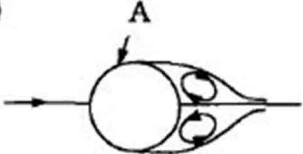
a)	No separation. Creeping (laminar) flow.	KC < 1.1
b)	Separation with Honji vortices. See Figs. 3.3 and 3.4	1.1 < KC < 1.6
c)	A pair of symmetric vortices	1.6 < KC < 2.1
d) A	A pair of symmetric vortices. Turbulence over the cylinder surface (A).	2.1 < KC < 4
e)	A pair of asymmetric vortices	4 < KC < 7
f)	Vortex shedding	7 < KC Shedding regimes

Figure 3.1: *Regimes of flow around a circular cylinder in oscillatory flow [69].*

As shown in Fig. 3.1a for very small values of KC no separation occurs and the flow is creeping. When KC is increased to 1.1, the first separation appears. For 1.1 < KC < 1.6 (Fig. 3.1b), the flow regime is defined for the Honji instability [38]. In

this range of KC, the two-dimensional flow over the cylinder surface breaks into a three-dimensional flow pattern. These regular streaks present mushroom-shape vortices. With a further increase of KC, separation occurs in the form of a pair of symmetric vortices as show in Fig. 3.1c. For $KC = 2.1$ is possible to observe turbulence over the cylinder (Fig. 3.1d). In the range $4 < KC < 7$ the symmetry between the two attached vortices breaks down. In this flow regime appears the lift force and this is due to the asymmetry in the vortices (Fig. 3.1e). For $KC > 7$ the flow regime is called vortex-shedding regime. In this context it is well underline that other authors ([62], [9]) fix this value at $KC = 6$. The vortex-shedding regimes present a different configuration as a function of the KC number. In these flow regimes the vortex shedding appears during the course of each half period of the oscillatory motion. Williamson [78], after an extensive investigation, defines different vortex-shedding regimes. In particular, for $7 < KC < 15$, the vortex-shedding is characterized by a single-pair regime. The single-pair regime presents a subrange $7 < KC < 13$ which is known as the transverse-vortex street regime. In this case, a series of vortices convect out to one side of the cylinder in the form of a street. The difference in the other subrange ($13 < KC < 15$) is that the wake consists of a series of pairs convecting away each cycle at around $45°$ to the wave direction and this occurs at one side only. A double-pair vortex-shedding regime regarding the portion of the KC ranges between 15 and 24. This flow regime is featured by two vortex pairs convecting away from the cylinder. A schematic classification into three fundamental classes of vortex-flow regimes in regular waves grouped by Sumer and Fredsoe [69] is reported in Figure 3.2.
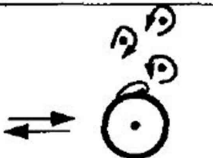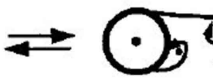
Regime of vortex motion	Pattern	KC range
Vortex pair		$O(1)<KC\leq 7$
Transverse vortex street		$7<KC\leq 15$
Vortex street		$KC>15$

Figure 3.2: *Classification of vortex-flow regime in regular waves [69].*

For further flow regimes, the number of vortex pairs will be increased by one each time the KC number is changed to a higher one. In the case of $24 < KC < 32$ the

number of vortex pairs will be three, four in the range of $32 < KC < 40$ and five in the range between 40 and 48. Hence, for every change of regime, there will be two more vortex sheddings in one full period. The vortex path in the transverse direction has a strong influence on the time series of the vertical hydrodynamic force acting on the cylinder. The peaks of the lift force are linked to the vortices around the cylindrical structure. In particular, the peak of the force which occurs after the flow reversal is related to the return of the shed vortex to the cylinder. The rest of the peaks in the lift direction is linked with the vortex shedding. For this reason, the lift force frequency is not the same to the vortex-shedding frequency.

3.2.1   Effect of wall proximity on flow regimes

There are mainly two effects of the wall proximity on the flow on a cylinder: the break-up of symmetry in the flow and the suppression of vortex shedding. These changes depend on the different values of the incoming wave height and on the distance between the wall and the cylinder. An investigation on the effect of the gap height was performed by Sumer et al. [70]. Figure 3.3 shows the vortex formation during regular waves with $KC = 4$ for different values of the gap-to-diameter ratio e/D, where e is the distance between the wall and the lower part of the cylinder.

The symmetry observed by the the authors in the formation and the motion of the vortices is clear in Figure 3.3a, when the cylinder is far from the sea bed ($e/D = 2$). In the other two cases, the asymmetry of the vortex evolution was highlighted by the arrows drawn by the authors. When the cylinder is placed on the bottom ($e/D = 0$), the vortex grows behind the cylinder each half period and is washed-over in the following half period [70].

The effect of the bottom on the flow field is clear also for higher values of KC number. The development of vortex patterns was illustrated in Figure 3.4 for $KC = 10$. In this flow regime, for a cylinder far from the bottom and under regular waves, the flow field is characterized by the formation of the transverse vortex street regime. This particular regime disappears when the gap-to-diameter ratio becomes less than about 1.7-1.8 [70]. In the case of $e/D = 0$, in comparison with Figure 3.3c, the evolution of vortex motion remains the same, regardless of the range of KC.

3.3   Near flow field induced by irregular waves

The flow regimes induced by irregular waves on horizontal circular cylinder are defined by the Re and KC numbers calculated considering the spectral characteristics of the random oscillatory flow. In the case of irregular waves, these non-dimensional parameters are evaluated as:

$$Re = \frac{u_{m0}D}{\nu} \tag{3.3}$$

$$KC = \frac{u_{m0}T_p}{D} \tag{3.4}$$

where u_{m0} is the significant velocity at the transversal axis of the cylinder ([13], [14]) and T_p is the peak wave period. The representative value for the velocity amplitude for random waves is given by:
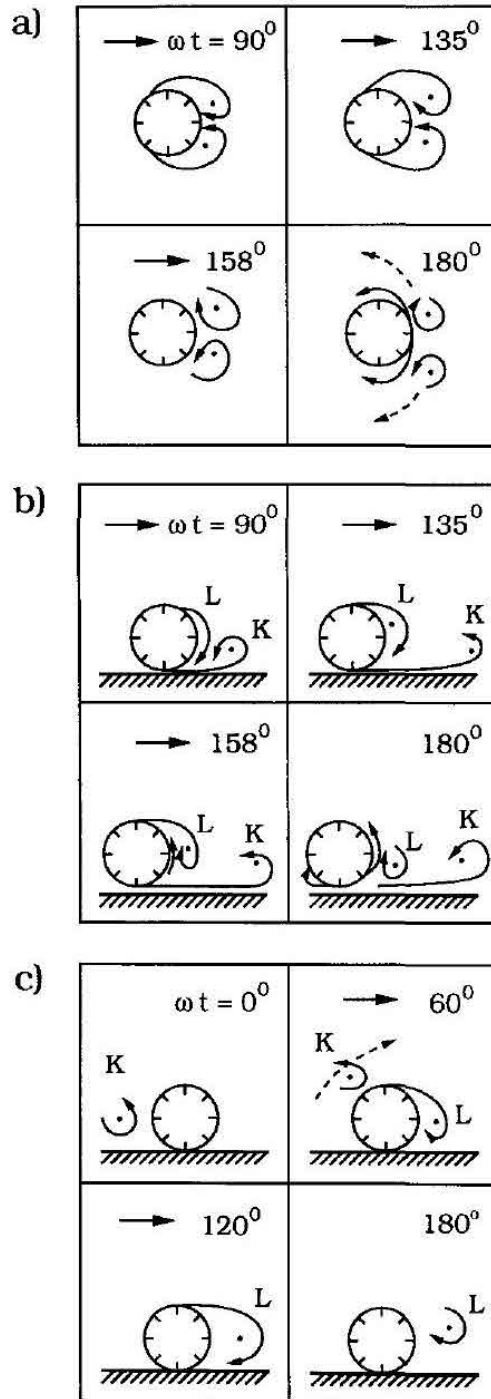
Figure 3.3: *Evolution of vortex in regular waves. KC = 4. (a) e/D = 2; (b) e/D = 0.1; (c) e/D = 0 [69].*

15

Figure 3.4: *Evolution of vortex in regular waves. KC = 10. (a) e/D = 1; (b) e/D = 0.1; (c) e/D = 0 [69].*

$$u_{m0} = \sqrt{2}\sigma_u \qquad (3.5)$$

where σ_u is the root-mean square value of the fluid velocity evaluated at the transversal axis of the cylinder.

The vortex-flow regime with the irregular waves is slightly different from the case of sinusoidal oscillatory flow. Sumer and Kozakiewicz [71] performed an experimental investigation to analyze the variation in the vortex-flow regimes. The authors, starting with a sinusoidal oscillatory flow, have reproduced random oscillatory flow with a narrow and broad band spectrum. A JONSWAP-type spectrum was used in the mentioned study. When the flow changes from regular oscillatory flow to random oscillatory flow, the degree of irregularity increases with the increasing of the spectral width parameter. Overall, an increasing of the irregularity of the waves reduces the occurrence of the fundamental vortex regimes. Only in the case of the transverse vortex street ($7 < KC$ < 15) there is a repeatable interaction between vortices of two successive half periods in sinusoidal flow. Nevertheless, this interaction is partially or at time completely prevented due to the randomly changing successive half periods of the motion. The reason is that the irregular waves break up the regular vortex regimes.

3.4 Near flow field induced by solitary waves

The flow field induced by solitary waves was studied in relation with the gap-to-diameter ratio. As performed by several authors who studied the interaction between solitary waves and marine structures (e.g., [26], [65], [72]), the non-dimensional wave amplitude, A/d, is considered as simple representative parameter to evaluate the features of the wave forces and coefficients with respect to Re and KC. The flow regime from solitary wave acting on circular cylinders has been numerically studied by Xiao et al. [81], Qu et al. [57] and Lin and Liao [43].

In the first two papers the authors have investigated the interaction between the solitary waves and the horizontal circular cylinder near the free surface. A representative test case in which the cylinder is near the free surface and quite far from the bottom is shown in Figure 3.5. The snapshots of vorticity contour were displayed in the time instant in which the surface elevation approaches its maximum value. In these numerical simulations [57], the values of A/d is equal to 0.2 while the gap-to-diameter ratio, e/D, ranges between 9.5 to 5.5 (Fig. 3.5). The incident solitary wave generated a pair of detached vortices in all numerical simulations. In the first case (Fig. 3.5a) is evident the influence of the free surface in the formation of the asymmetric vortices. In the other snapshots of the vorticity field the size of the two vortices, which rotate in the opposite direction, is similar. This flow field generated by the solitary waves, for this value of A/d, presents only a pair of vortices. This configuration is similar to the vortex-pair regime in the regular oscillation flow when the value of the Keulegan-Carpenter number is lower than 7.

Lio and Liao [43] focused their studies in analyzing the effects of gap-to-diameter ratio and incident wave height on vorticity patterns when a solitary wave is passing over a circular cylinder near the bottom. Figure 3.6 shows the vorticity field for different e/D and for a unique wave forcing, i.e. $A/d = 0.3$. During the passage of the solitary wave crest, the separated shear layer from the upper half of the cylinder rolls up
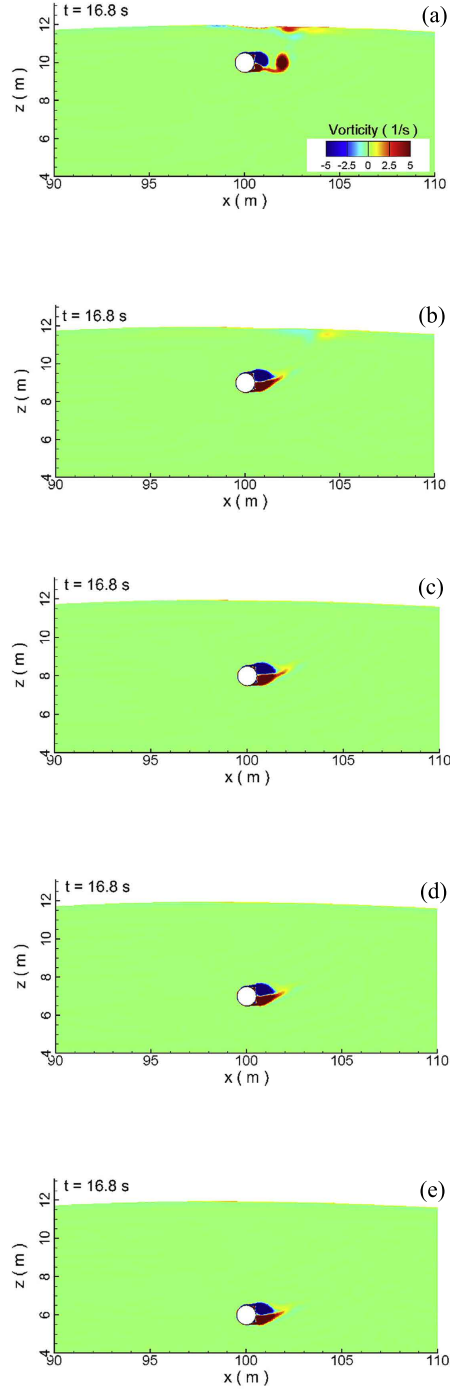
Figure 3.5: *Vorticity field with different gap-to-diameter ratio. A/d = 0.2. (a) e/D = 9.5; (b) e/D = 8.5 (c) e/D = 7.5; (d) e/D = 6.5; (e) e/D = 5.5 [57].*
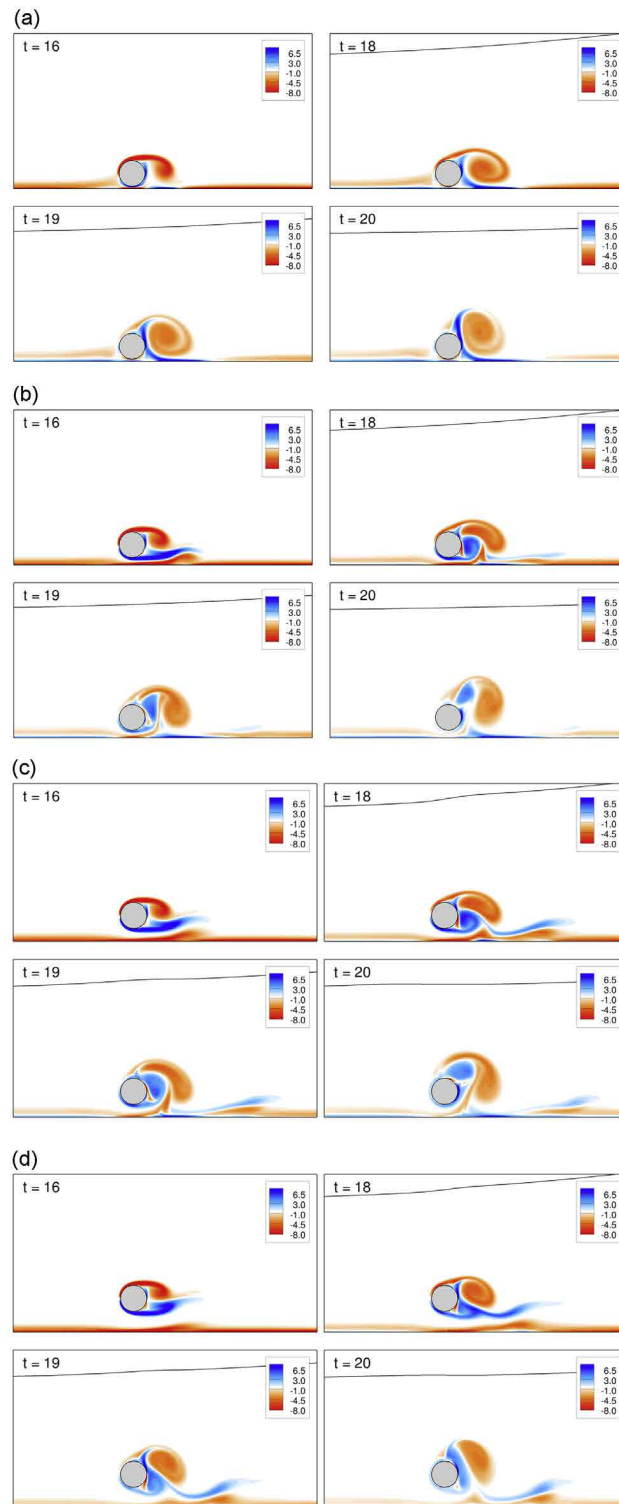
Figure 3.6: *Vorticity field with different gap-to-diameter ratio. A/d = 0.3. (a) e/D = 0.1; (b) e/D = 0.3 (c) e/D = 0.5; (d) e/D = 0.8 [43].*

and forms a main vortex with clockwise (negative) vorticity behind the cylinder. In this recirculating region, when the wave crest is already passed with respect to the cylinder, the secondary vortex with counterclockwise (positive) vorticity vertically passes through the main shear layer from the cylinder (Fig. 3.6a). An increasing of the gap height, i.e. $e/D = 0.3$, induces a stretching of the secondary vortex along the bottom. With the leaving of the wave crest (t $\geq$ 18 s) the secondary vortex is cut off by the clockwise vorticity. In the last two time instants (Fig. 3.6b, t = 19 s and t = 20 s) the primary and the secondary vortices work like a vortex dipole that moves in ascending way. Figure 3.6(c) and (d) show that with the increasing of the value of e/D the interaction between the cylinder and the seabed is weaker. Nevertheless, also in these cases, the vortices move upward like a vortex dipole similarly to the previous case [43]. Taking into account the effect of wave height in the vortices formation, the increasing in the values of A/d induces an enhance of the strength of the vortices. In all the cases, the vortices, that result well developed when the wave crest is away from the cylinder, influence the loads exerted on the cylindrical structure.

3.5 Classical semi-empirical equations of hydrodynamic forces

For the purposes of studying the hydrodynamic forces acting on a circular cylindrical structure, it is necessary to characterize the force regimes derived from the incident waves. In this context, it is significant to underline the differences between large and small bodies. Sarpkaya and Isaacson [62] described the generation mechanism of the wave forces on a cylindrical structure. The dominant cause of wave force generation is specified as a function of two non-dimensional parameters: KC and the diffraction parameter, D/L (Fig. 3.7).

The diffraction parameter is related to the intensity of scattered waves. The critical value of D/L which divides a small and a large body is about 0.2. In this case, KC becomes 2 at the most for the range of $D/L > 0.2$ due to the wave breaking. For this low value of KC number, the flow separation effect may be neglected in the wave force calculation. According to several authors ([62], [15], [69]), for $D/L > 0.2$ and $KC < 4$, the wave diffraction of the incident wave on the structure in a wide area prevails and the inertia forces result dominant. The loads on the large body are usually calculated using the diffraction theory (e.g., [9]). On the other hand, when the bodies are small, the Morison-type equations can be applied (e.g., [54]). In this case, the influence of the cylinder is bounded to a narrow area around the structure. For $D/L < 0.2$ and $KC > 4$ the hydrodynamic forces have two components: drag and inertia forces in horizontal direction, and lift and inertia forces in vertical direction.

3.5.1 The Morison equation

The Morison equation [54] represents an easy and widespread tool for predicting the horizontal force induced by waves and currents on cylindrical structures. The in-line force, F_H, is evaluated as the sum of a drag component, F_D, due to the resistance of an obstacle to the fluid motion, and an inertia component, F_{HI}, depending on the presence of an external horizontal acceleration at the body section. The expression for F_H reads as:
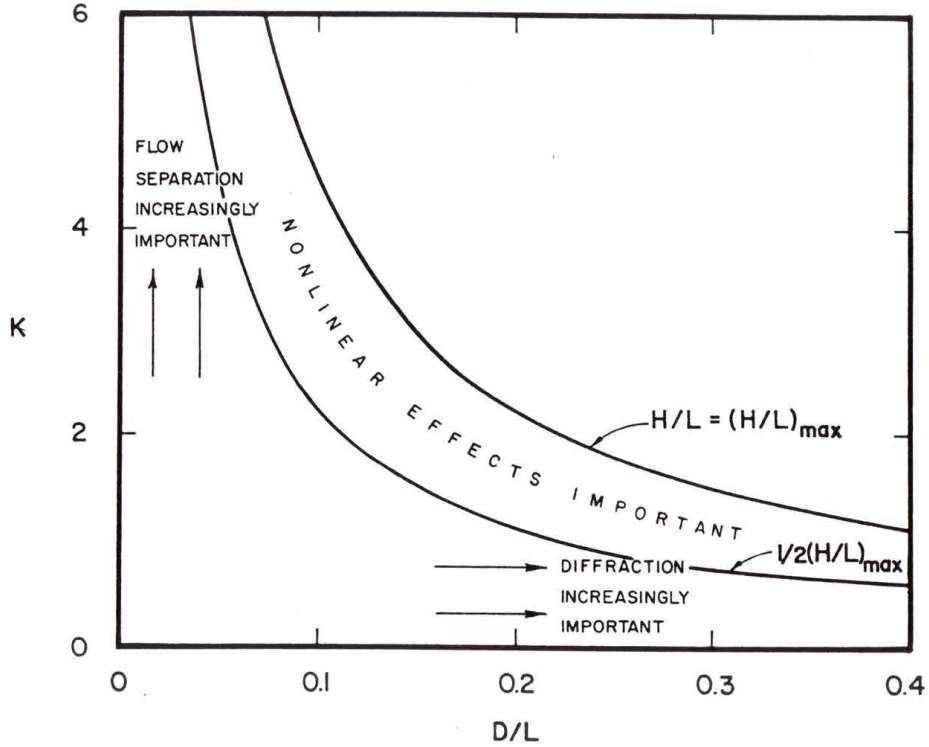
Figure 3.7: *Wave force regimes [62].*

$$F_H(t) = F_D(t) + F_{HI}(t) = \frac{1}{2}\rho D C_D u(t)|u(t)| + \frac{\pi}{4}D^2\rho C_{MH}a_H(t) \qquad (3.6)$$

where C_D is the drag coefficient and C_{MH} is the horizontal inertia coefficient, while u and a_H represent the undisturbed horizontal velocity and acceleration at the traversal axis of the cylinder, respectively.

3.5.2 The transverse equation

Along the lines of the Morison scheme, the transverse equation (e.g., [16]) allows for calculating the vertical force, F_V, as the sum of a lift component, F_L, generated by the increased velocity across the cylinder induced by the blocking of the flow, and an inertia component, F_{VI}, depending on the vertical acceleration of the external flow. The transverse force is then written as:

$$F_V(t) = F_L(t) + F_{VI}(t) = \frac{1}{2}\rho D C_L u^2(t) + \frac{\pi}{4}D^2\rho C_{MV}a_V(t) \qquad (3.7)$$

where C_L is the lift coefficient and C_{MV} is the vertical inertia coefficient, while a_V is the free stream vertical acceleration at the mentioned location.

The free stream kinematic field in the Morison and transverse formulas has been here calculated analytically by system 2.6 from the numerical and experimental values of the surface elevation, η, at the vertical section of the cylinder.

21

3.6 Alternative semi-empirical equations of hydrodynamic forces

3.6.1 The Gurnari and Filianoti equation

The analytical solution is derived by the original approach proposed by Filianoti and Piscopo [27] for a rectangular submerged barrier, and reformulated by Gurnari and Filianoti [33] for the case of a horizontal cylinder. The methodology for calculating the horizontal force exerted by solitary waves on submerged cylindrical obstacles is based on the speed drop factor, F_r. With reference to Figure 3.8, the time lag $\Delta t F_r$ spent by the pressure fluctuation to cover the distance from point 1' to point 2', both lying on the surface of a solid obstacle (i.e., a horizontal cylinder), is greater than the time Δt spent to cover the same distance between the points 1 and 2 in the absence of the obstacle. Let us indicate by F_r (> 1) the reduction factor in the propagation speed. The existence of F_r let us to explain why the horizontal force on the solid body is different from the Froude-Krylov force, even if amplitudes of pressure fluctuations are unchanged on points 1' and 1, and on 2' and 2. The same phenomenon occurs in the
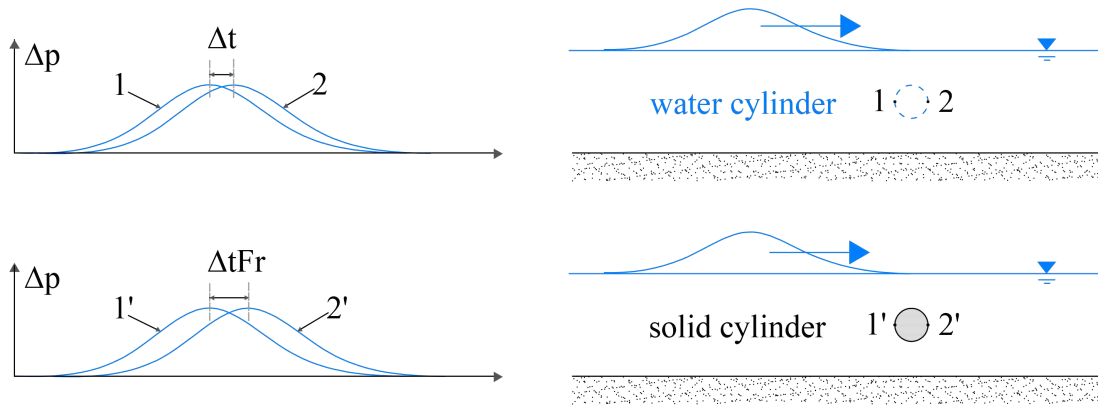
Figure 3.8: *Definition sketch for the speed drop factor F_r. Upper panel: pressure time series at points 1 and 2 on the equivalent wates mass. Lower panel: pressure time series at points 1' and 2' on the solid body represent by the cylinder.*

interaction between wind waves and cylinders with arbitrary position. The speed $\underline{c}_{\Delta p}$ of pressure head waves propagating across the cylinder can be calculated dividing the diameter D by the time spent by the wave crest to cover this distance. The value of $c_{\Delta p}$ in the undisturbed field is constant and it can be calculated measuring the time spent by the wave crest to cover the distance between points 1 and 2. The ratio $c_{\Delta p}/\underline{c}_{\Delta p}$ is equal to the speed drop factor F_r. The horizontal component of the unitary force acting on the water cylinder during the passage of the solitary wave can be calculated as:

$$F_H(t) = F_{HA}(t) - F_{HB}(t) \tag{3.8}$$

where F_{HA} and F_{HB} are the horizontal forces acting on semi-cylinder A and B, respectively:

$$F_{HA}(t) = \int_{-\pi/2}^{\pi/2} \Delta p(-\epsilon/2, t) r \cos\beta \, d\beta \tag{3.9}$$

22

$$F_{HB}(t) = \int_{-\pi/2}^{\pi/2} \Delta p(\epsilon/2, t) r cos\beta d\beta \tag{3.10}$$

where Δp is the wave pressure on the semi-cylinder, β is the angle defined in Figure 3.9, and ϵ is the phase angle for the water (3.11) and the solid (3.12) cylinder:
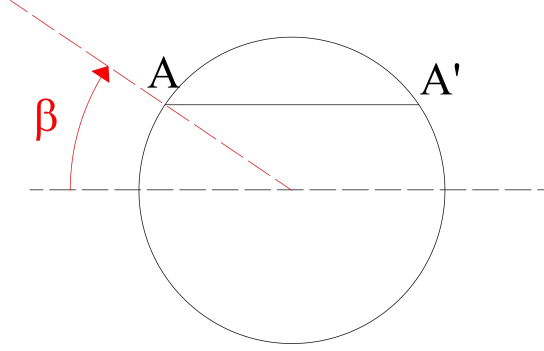
Figure 3.9: *Definition of angle β.*

$$\epsilon = D \left|cos\beta\right| \tag{3.11}$$

$$\epsilon = F_r D \left|cos\beta\right| \tag{3.12}$$

Considering the weighted average value of $cos\beta$ in the phase angle ϵ, we obtain:

$$\bar{\beta} = \frac{\int_{-\pi/2}^{\pi/2} cos^2\beta d\beta}{\int_{-\pi/2}^{\pi/2} cos\beta d\beta} = \pi/4 \tag{3.13}$$

which once substituted in Eqs. 3.11 and 3.12 permit us to integrate Eqs. 3.9 and 3.10, obtaining:

$$F_{HA}(t) = -\rho g A D tanh^2 \left[-k\left(F_r \frac{\pi}{2} D + ct\right)\right] \tag{3.14}$$

$$F_{HB}(t) = -\rho g A D tanh^2 \left[k\left(F_r \frac{\pi}{2} D - ct\right)\right] \tag{3.15}$$

The speed drop factor F_r depends on the relative amplitude A/d of the solitary wave, for a given diameter D of the cylinder and draft of its center.

3.6.2 The shifted transverse equation

The shifted transverse equation represents a proposed extension of the transverse formulation (see Eq. 3.7) for a cylinder near the bottom to well model the peaks and the phase shifts of the hydrodynamic forces. Historically, the transverse forces are more strongly affected than the horizontal ones by the formation and shedding of vortices close to a cylindrical structure [69]. In particular, the original form of the lift component did not model the forward phase shift in the observed experimental and numerical

time series of the vertical loads when a horizontal cylinder is placed near the bed. In this context, a new form of the lift force is proposed which takes the following form:

$$F_L(t) = \frac{1}{2}\rho D C_L [u(t + t_s)]^2 \tag{3.16}$$

where t_s is a time interval between the occurrence of the wave crest and that related to the peak of the observed vertical force. The proposed time shift is expressed as:

$$t_s = \frac{T\phi}{2\pi} \tag{3.17}$$

where the phase angle, ϕ, is assumed to be dependent on the wave amplitude and water depth. The values of the phase angle will be illustrated in Section 6.4.

CHAPTER *4*

Laboratory investigation

The laboratory investigation was performed in the wave channel of the GMI Laboratory at the Department of Civil Engineering of the University of Calabria.

4.1 Description of the wave flume

The wave flume is 41.0 m long, 1.2 m deep and 1.0 m wide. It is composed by a steel framework with glass walls, divided into 15 modules with a length of 2.7 m each and a flat glass bottom, appropriately jointed between the channel modules (Fig. 4.1).

It is equipped with a piston-type wavemaker moved by a servo-controller hydraulic actuator and a rubble mound breakwater made by concrete blocks and natural stones (slope of 1:4) to dissipate the incident waves in the final part.

4.2 Hardware/software instrumentation

This section provides an overview about the hardware/software instrumentation used in the experiments.

As for the hardware side, there are two main units: the paddle movement controller and the level sensor array. The first unit is represented by the block diagram showed in Figure 4.2 and it has the typical configuration of an analog feed-back control system [28]. The paddle movement is controlled indirectly by the rotation of a joint of the mechanical chain, that is connected to the paddle. The rotation angle is measured with a resistive encoder that provides a proportion analog voltage signal. This signal is processed, as well as the set-point signal, by a properly tuned Proportional Integral Derivative (PID) controller [56]. The PID acts in order to minimize the error, i.e. the difference between the set-point and the feedback signals. The output of the PID is

Figure 4.1: *Wave flume in the GMI Laboratory.*
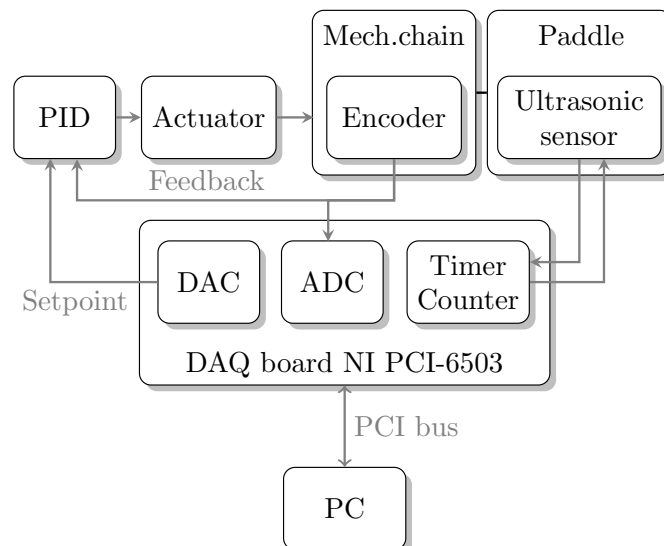
Figure 4.2: *Block diagram of paddle movement controller unit.*

connected to the kinematic chain through a hydro-pneumatic actuator. The set-point signal is generated by a Data AcQuision Board (DAQ), thanks to a Digital-to-Analog Converter (DAC). The DAQ board (NI PCI-6503) is physically installed into the PCI bus of a personal computer and it also provides other electronic peripherals, such us an Analog-to-Digital Converter (ADC) and several digital timer/counter units. The ADC is used to acquire the feedback signal, whereas the timer/counters are used to manage an ultrasonic sensor placed on the back side of the paddle. More specifically, one timer/counter is used to generate a train of pulse in order to trigger the ultrasonic wave emission and the second timer/counter is used to measure the pulse width of the echo signal. The ultrasonic sensor allows a more precise estimation of the paddle movement, because it has a well known calibration equation that relates the measured echo with the effective distance. The sensor array unit is represented by the block diagram showed in Figure 4.3.
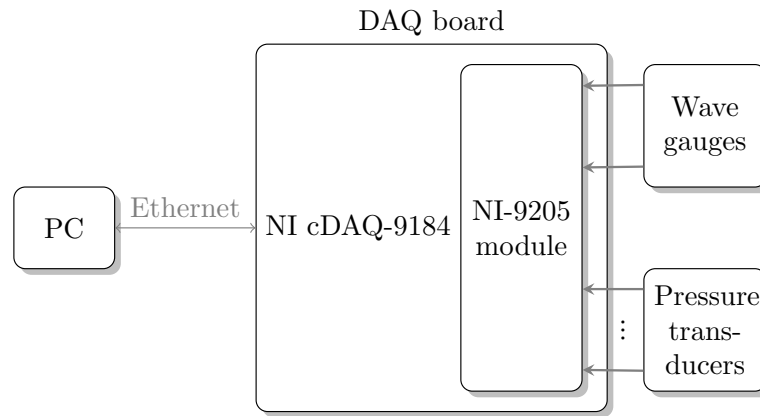
Figure 4.3: *Block diagram of sensor array unit.*

A second DAQ board (a NI cDAQ9184 chassis with a NI-9205 module) is connected to the same personal computer of the previous unit, by an ethernet cable, in order to guarantee a good synchronism and noise rejection. Two different kind of resistive sensors have been used: 12 Druck PDCR1830 pressure transducers, which are acquired in differential mode due the Wheatstone-bridge configuration and 4 Edif Instrument wave gauges, which are acquired in single-ended mode.

As for the software side, the wave flume operations are remotely controlled by a specifically designed LabVIEW application. Interacting with its simple Graphical-User-Interface (GUI), it is possible to set-up the wavemaker input signal and assign particular wave shapes, start/stop the experiment, and monitor all sensors data in real-time mode. This application is a high-level interface to the hardware modules described previously.

The twelve pressure transducer and the four wave gauges were calibrated before their installation in the wave channel. The relationship between the values in Volts and the values in meters is perfectly linear for both the instruments.
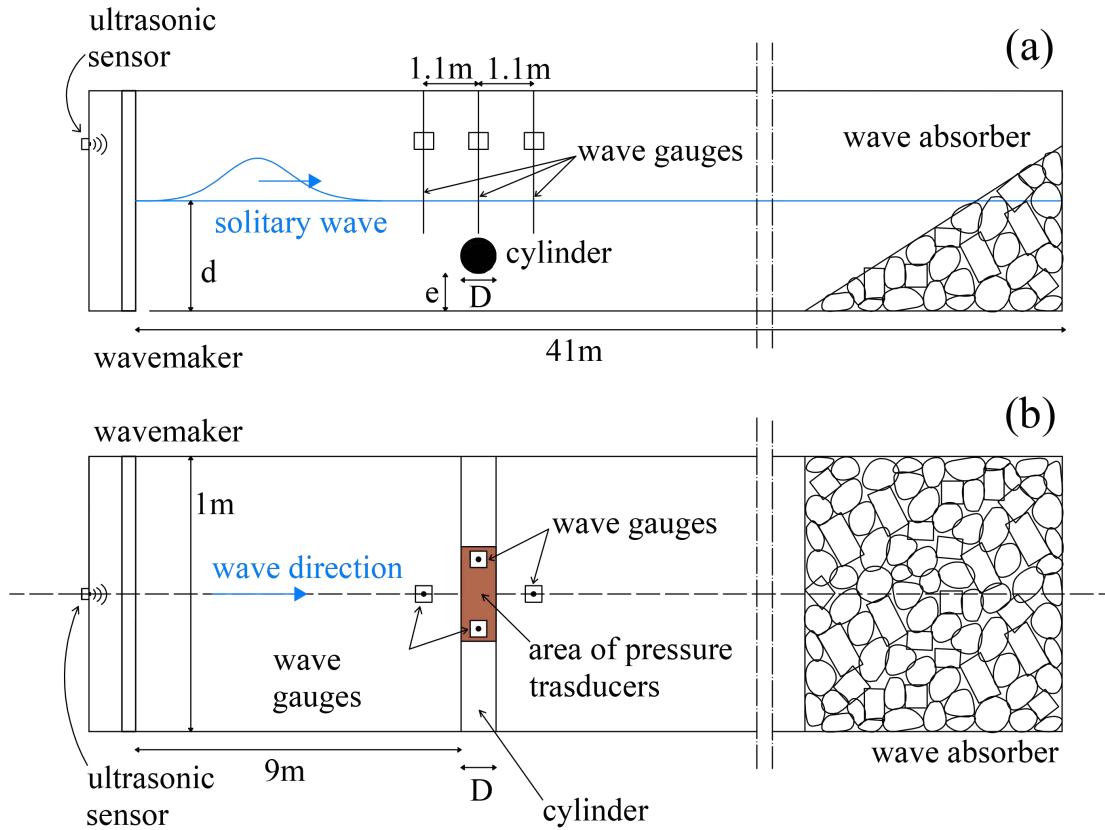
Figure 4.4: *Sketch of the experimental setup. (a) Longitudinal profile; (b) Plan view.*

4.3 Experimental set-up

The longitudinal profile and the general plan view of the experimental layout are respectively depicted in Figs. 4.4a and 4.4b .

At a distance of about 9 m from the paddle, a rigid circular cylinder having a diameter $D = 0.127$ m and longitudinal axis parallel to the cross flume axis was placed. It was mounted in the flume by a steel support equipped by a pulley system able to move it to a specific depth. In particular, five depths of the cylinder location were taken into account, ranging between 0.2 m and 0 (cylinder at the bottom). In the last case, a special glue was adopted to fix the cylinder at the bottom in order to inhibit the passage of water flows below it. To inhibit corrosion, an electrolytic zinc plating was used to coat the surface of the iron cylinder. Twelve pressure transducers were mounted along the external surface of the cylinder at 30° intervals. Following similar experimental investigations in the presence of cylinders ([70] [6] [7]), the adopted sensors (length of about 0.1 m) were slightly staggered along the longitudinal axis due to construction constraints and to avoid the use of a too large diameter. Specifically, they were placed in the central part of the cylinder for a total length of 0.33 m and a mutual distance of 0.03 m, as highlighted in the plan view of Fig. 4.5a where the while holes indicate the external position of the transducer heads and the grey ones indicate their internal position. This arrangement was possible because of the cylindrical fronts of the solitary waves propagating along the channel, leading to the study of the present 2D process.

Details of the cylinder placement and the assembling of the transducers inside it are respectively illustrated in Figs. 4.5b and 4.5c.
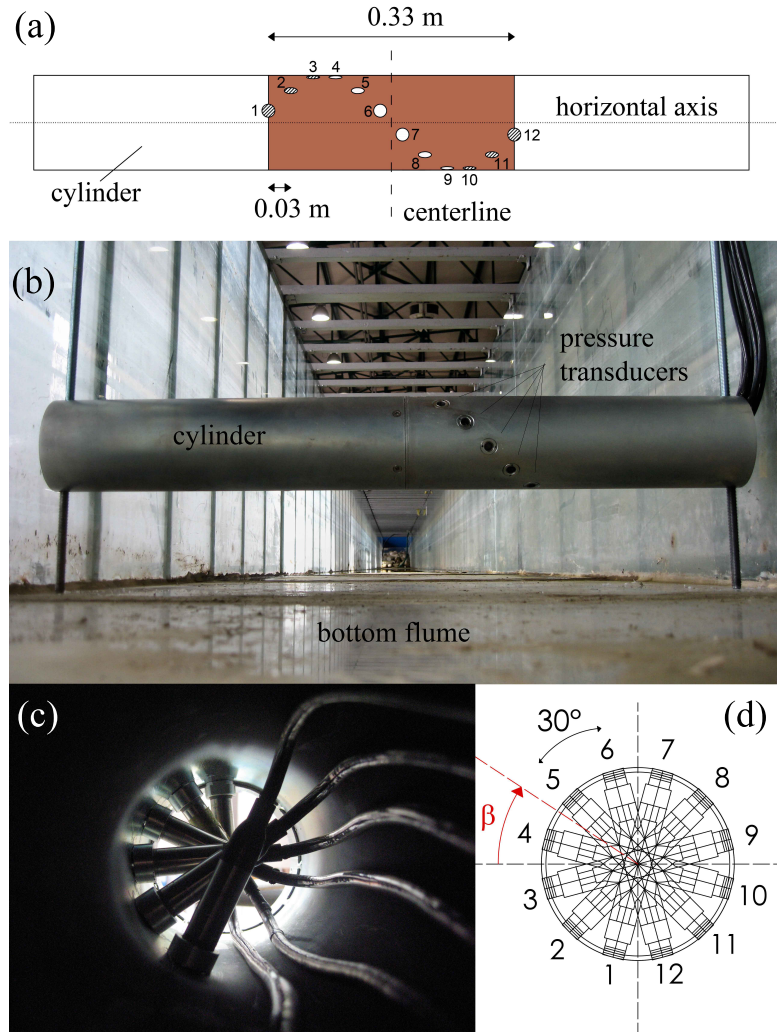
Figure 4.5: *(a) Plan view of the staggered arrangement of the transducers in the central part of the cylinder (case with e/D = 1); (b) Front view from the wavemaker of the cylinder placement in the wave flume; (c) Detail of the installation of the transducers inside the cylinder; (d) Representative cross section of the transducers around the cylinder.*

The dynamic pressures, Δp, deduced from the pressure records were calculated as a function of the position of the transducers. Each value of dynamic pressure was assumed constant over the influence area for the evaluation of the experimental force components. Consequently, the horizontal, F_H, and vertical, F_V, hydrodynamic forces were calculated as:

$$
\begin{cases}
F_H = a_1 \left(\Delta p_1 + \Delta p_6 - \Delta p_7 - \Delta p_{12} \right) + \\
\quad + a_2 \left(\Delta p_2 + \Delta p_5 - \Delta p_8 - \Delta p_{11} \right) + \\
\quad + a_3 \left(\Delta p_3 + \Delta p_4 - \Delta p_9 - \Delta p_{10} \right) \\
\\
F_V = a_1 \left(\Delta p_3 + \Delta p_{10} - \Delta p_4 - \Delta p_9 \right) + \\
\quad + a_2 \left(\Delta p_2 + \Delta p_{11} - \Delta p_5 - \Delta p_8 \right) + \\
\quad + a_3 \left(\Delta p_1 + \Delta p_{12} - \Delta p_6 - \Delta p_7 \right)
\end{cases}
\tag{4.1}
$$

where the influence areas a_1, a_2 and a_3 are respectively equal to:

$$
a_1 = \int_{\pi/3}^{\pi/2} \frac{D}{2} cos\beta d\beta, \quad a_2 = \int_{\pi/6}^{\pi/3} \frac{D}{2} cos\beta d\beta, \quad a_3 = \int_{0}^{\pi/6} \frac{D}{2} cos\beta d\beta \tag{4.2}
$$

The angle, β, was taken from the left side of the cylinder in a clockwise direction. The enumeration of transducers followed the reference system and is shown in Fig. 4.5d.

Two wave gauges were located in correspondence of the vertical axis of the cylinder to measure the surface elevation and other two 1.1 m before and after this section. The sampling frequency, f_s, of transducers and gauges was set at 1000 Hz. To check the correct generation of the desired solitary wave by applying Eq. 2.10, the horizontal displacement of the piston, X, was measured by an ultrasonic sensor located 0.55 m behind the position at rest of the paddle using f_s = 50 Hz.
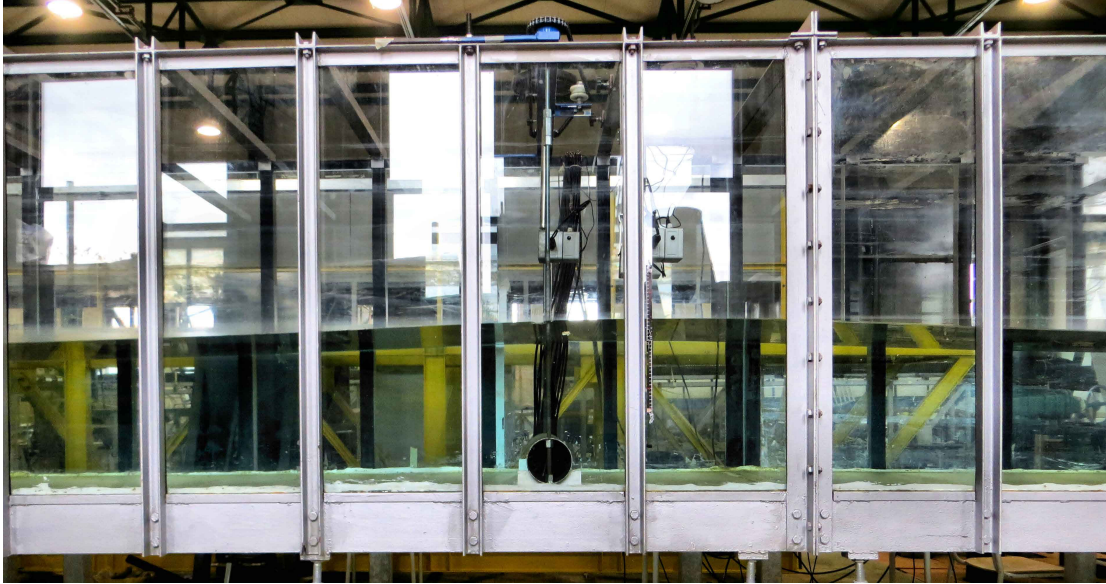
Figure 4.6: *Solitary wave in the laboratory channel (e/D = 0.1).*

4.4 Characteristics of laboratory tests

A set of 134 experimental tests with different solitary waves in terms of wave amplitude acting on the horizontal cylinder and five different vertical position of the cylinder was performed. The still water depth d of the experimental tests was fixed at 0.4 m. The tests were performed with five depths, so that the gap-to-diameter ratio assumed the values of $e/D = 1$, $e/D = 0.5$, $e/D = 0.25$, $e/D = 0.1$ and $e/D = 0$ (Fig.4.6). As previously mentioned, the value of e represents the distance between the bottom of the cylinder and the bed (Fig. 4.4). In the possible range of the experimental stroke S of the piston-type wavemaker and for the adopted five values of e/D, Tables 4.1, 4.2, 4.3, 4.4, 4.5 show the experimental values of A, T, A/d, $KC = u_{max}T/D$, $Re = u_{max}D/\nu$ and d/L (relative depth), where u_{max} is the maximum horizontal velocity at the transversal axis of the cylinder and ν is the kinematic viscosity. With respect to the theoretical wave period which increases when A decreases, the experimental values of T, in some cases, show a small deviation for this tendency because of the large spreading of η near SWL due to the occurrence of trailing waves [32]. It can also be noticed that the range of d/L refers to intermediate water depths quite close to shallow ones allowing for the use of Eq. 2.6 to represent the free stream velocity field at the cylinder. As performed by several authors who have studied the interaction between solitary waves and marine structures (e.g., [26] [65] [72]), the non-dimensional wave amplitude, A/d, will be considered as simple representative parameter to evaluate the features of the wave forces and coefficients with respect to Re and KC in the considered experimental and numerical dataset. A particular note can be referred to the magnitude of KC number, a largely adopted parameter to describe the flow field near the cylinder and the features of the hydrodynamic forces and coefficients in the presence of oscillatory flows (e.g., [69]). Indeed, owing to the dependence of the arbitrary finite wave period to model the solitary wave, also an apparent Keulegan-Carpenter number should be defined. To better analyze the occurrence of the force components due to the wave-cylinder interaction, the obtained results will be illustrated also considering the obtained values of KC.

The range of the involved physical quantities refers to small-scale experiments with approximate Froude scale of 1:100. This leads to real conditions characterized by leading waves of tsunamis with amplitudes up to 8 m and periods up to 44 s propagating on a water depth of 40 m and acting a circular cylinder having a diameter of 12.7 m whose size is comparable with an underwater floating tunnel.

Test Number	A (m)	T (s)	A/d	KC	Re	d/L
1A	0.031	4.10	0.079	4.82	1.81×10^4	0.047
2A	0.032	4.34	0.081	5.22	1.85×10^4	0.045
3A	0.038	4.38	0.096	6.15	2.15×10^4	0.044
4A	0.039	4.12	0.097	5.89	2.19×10^4	0.047
5A	0.046	3.86	0.116	6.48	2.57×10^4	0.049
6A	0.047	4.04	0.117	6.78	2.58×10^4	0.047
7A	0.051	3.79	0.127	6.89	2.80×10^4	0.050
8A	0.052	3.35	0.128	6.11	2.80×10^4	0.057
9A	0.053	4.02	0.133	7.62	2.91×10^4	0.047
10A	0.054	3.32	0.135	6.39	2.95×10^4	0.057
11A	0.057	3.88	0.143	7.87	3.11×10^4	0.049
12A	0.059	3.64	0.146	7.52	3.17×10^4	0.052
13A	0.062	3.26	0.156	7.11	3.35×10^4	0.058
14A	0.071	3.21	0.177	7.81	3.74×10^4	0.058
15A	0.078	2.98	0.196	7.86	4.06×10^4	0.062
16A	0.079	3.15	0.197	8.37	4.09×10^4	0.059

Table 4.1: *Characteristics of laboratory tests with e/D = 1.*

Test Number	A (m)	T (s)	A/d	KC	Re	d/L
1B	0.033	3.87	0.083	4.65	1.85×10^4	0.050
2B	0.033	4.02	0.083	4.89	1.87×10^4	0.048
3B	0.035	3.82	0.088	4.86	1.95×10^4	0.051
4B	0.035	3.75	0.088	4.82	1.98×10^4	0.052
5B	0.037	3.76	0.093	4.99	2.04×10^4	0.051
6B	0.040	3.80	0.100	5.43	2.20×10^4	0.051
7B	0.040	3.78	0.100	5.42	2.20×10^4	0.051
8B	0.041	3.74	0.103	5.48	2.25×10^4	0.052
9B	0.043	3.60	0.108	5.53	2.36×10^4	0.053
10B	0.043	3.85	0.108	5.94	2.37×10^4	0.050
11B	0.044	3.89	0.110	6.11	2.41×10^4	0.049
12B	0.045	3.62	0.113	5.84	2.48×10^4	0.053
13B	0.046	4.12	0.115	6.79	2.54×10^4	0.047
14B	0.047	3.98	0.118	6.62	2.56×10^4	0.048
15B	0.050	3.80	0.125	6.68	2.70×10^4	0.050
16B	0.050	3.56	0.125	6.28	2.71×10^4	0.054
17B	0.050	3.53	0.125	6.28	2.73×10^4	0.054
18B	0.053	3.44	0.133	6.40	2.85×10^4	0.055
19B	0.053	3.86	0.133	7.21	2.87×10^4	0.049
20B	0.054	3.79	0.135	7.17	2.91×10^4	0.050
21B	0.058	3.55	0.145	7.10	3.07×10^4	0.053
22B	0.058	3.31	0.145	6.63	3.07×10^4	0.057
23B	0.058	3.25	0.145	6.54	3.09×10^4	0.058
24B	0.062	3.08	0.155	6.58	3.28×10^4	0.061
25B	0.064	3.25	0.160	7.05	3.33×10^4	0.058
26B	0.064	3.33	0.160	7.24	3.35×10^4	0.056
27B	0.066	3.61	0.165	8.03	3.42×10^4	0.052
28B	0.068	3.22	0.170	7.43	3.54×10^4	0.058
29B	0.069	3.16	0.173	7.35	3.57×10^4	0.059
30B	0.069	3.05	0.173	7.11	3.59×10^4	0.061
31B	0.070	3.21	0.175	7.55	3.62×10^4	0.058

Table 4.2: *Characteristics of laboratory tests with e/D = 0.5.*

Test Number	A (m)	T (s)	A/d	KC	Re	d/L
1C	0.031	4.30	0.077	4.86	1.74×10^4	0.045
2C	0.031	3.81	0.077	4.35	1.75×10^4	0.051
3C	0.032	3.76	0.080	4.37	1.79×10^4	0.052
4C	0.032	4.13	0.080	4.82	1.79×10^4	0.047
5C	0.034	4.09	0.085	5.10	1.92×10^4	0.047
6C	0.035	3.85	0.088	4.94	1.97×10^4	0.050
7C	0.039	4.34	0.098	6.11	2.16×10^4	0.044
8C	0.040	3.92	0.100	5.57	2.18×10^4	0.049
9C	0.043	3.44	0.108	5.26	2.35×10^4	0.056
10C	0.043	3.53	0.108	5.42	2.36×10^4	0.054
11C	0.046	4.03	0.115	6.58	2.50×10^4	0.047
12C	0.047	3.75	0.118	6.18	2.53×10^4	0.051
13C	0.047	3.76	0.118	6.27	2.56×10^4	0.051
14C	0.050	3.52	0.125	6.13	2.68×10^4	0.054
15C	0.051	3.78	0.128	6.69	2.72×10^4	0.050
16C	0.051	3.68	0.128	6.54	2.73×10^4	0.052
17C	0.054	3.39	0.135	6.33	2.87×10^4	0.056
18C	0.054	3.58	0.135	6.76	2.90×10^4	0.053
19C	0.055	3.77	0.138	7.16	2.92×10^4	0.050
20C	0.058	3.49	0.145	6.98	3.07×10^4	0.054
21C	0.059	3.74	0.148	7.56	3.11×10^4	0.051
22C	0.060	3.81	0.150	7.86	3.17×10^4	0.049
23C	0.064	3.09	0.160	6.73	3.35×10^4	0.061
24C	0.065	3.39	0.163	7.49	3.39×10^4	0.055
25C	0.066	3.38	0.165	7.49	3.40×10^4	0.055
26C	0.070	3.20	0.175	7.46	3.58×10^4	0.058
27C	0.070	3.41	0.175	7.95	3.58×10^4	0.055
28C	0.070	3.11	0.175	7.26	3.59×10^4	0.060

Table 4.3: *Characteristics of laboratory tests with e/D = 0.25.*

Test Number	A (m)	T (s)	A/d	KC	Re	d/L
1D	0.032	3.74	0.080	4.39	1.80×10^4	0.052
2D	0.033	3.84	0.083	4.56	1.82×10^4	0.051
3D	0.034	3.85	0.085	4.74	1.89×10^4	0.050
4D	0.035	3.89	0.088	4.94	1.95×10^4	0.050
5D	0.035	4.02	0.088	5.17	1.98×10^4	0.048
6D	0.036	4.05	0.090	5.27	2.00×10^4	0.048
7D	0.038	3.55	0.095	4.89	2.12×10^4	0.054
8D	0.038	3.73	0.095	5.17	2.13×10^4	0.052
9D	0.043	3.52	0.108	5.35	2.33×10^4	0.055
10D	0.043	3.50	0.108	5.35	2.35×10^4	0.055
11D	0.044	3.54	0.110	5.57	2.40×10^4	0.054
12D	0.047	3.95	0.118	6.50	2.53×10^4	0.048
13D	0.047	3.60	0.118	5.99	2.56×10^4	0.053
14D	0.050	3.47	0.125	6.04	2.67×10^4	0.055
15D	0.050	3.67	0.125	6.43	2.69×10^4	0.052
16D	0.051	3.60	0.128	6.37	2.71×10^4	0.053
17D	0.053	3.40	0.133	6.29	2.84×10^4	0.056
18D	0.054	3.43	0.135	6.40	2.86×10^4	0.055
19D	0.055	3.54	0.138	6.72	2.92×10^4	0.054
20D	0.059	3.37	0.148	6.76	3.08×10^4	0.056
21D	0.060	3.40	0.150	6.93	3.13×10^4	0.055
22D	0.060	3.39	0.150	6.94	3.14×10^4	0.056
23D	0.060	3.15	0.150	6.46	3.15×10^4	0.060
24D	0.062	3.31	0.155	6.93	3.22×10^4	0.057
25D	0.062	3.31	0.155	6.98	3.24×10^4	0.057
26D	0.063	3.34	0.158	7.11	3.27×10^4	0.056
27D	0.068	3.02	0.170	6.86	3.49×10^4	0.062
28D	0.071	3.04	0.178	7.14	3.60×10^4	0.061
29D	0.072	3.17	0.180	7.51	3.64×10^4	0.059

Table 4.4: *Characteristics of laboratory tests with e/D = 0.1.*

Test Number	A (m)	T (s)	A/d	KC	Re	d/L
1E	0.033	3.73	0.083	4.43	1.83×10^4	0.052
2E	0.034	3.84	0.085	4.69	1.87×10^4	0.051
3E	0.034	3.82	0.085	4.74	1.91×10^4	0.051
4E	0.035	3.83	0.088	4.86	1.95×10^4	0.051
5E	0.037	3.91	0.093	5.17	2.03×10^4	0.050
6E	0.041	3.99	0.103	5.86	2.26×10^4	0.048
7E	0.041	3.78	0.103	5.60	2.27×10^4	0.051
8E	0.042	3.87	0.105	5.76	2.29×10^4	0.050
9E	0.042	4.06	0.105	6.06	2.29×10^4	0.047
10E	0.043	3.37	0.108	5.10	2.33×10^4	0.057
11E	0.044	3.73	0.110	5.77	2.38×10^4	0.051
12E	0.044	3.64	0.110	5.70	2.41×10^4	0.053
13E	0.045	3.90	0.113	6.19	2.44×10^4	0.049
14E	0.046	3.79	0.115	6.17	2.50×10^4	0.050
15E	0.046	3.47	0.115	5.67	2.51×10^4	0.055
16E	0.048	4.05	0.120	6.87	2.61×10^4	0.047
17E	0.049	3.88	0.123	6.66	2.64×10^4	0.049
18E	0.052	3.86	0.130	7.00	2.78×10^4	0.049
19E	0.054	3.56	0.135	6.62	2.86×10^4	0.053
20E	0.055	3.59	0.138	6.84	2.92×10^4	0.053
21E	0.055	3.69	0.138	7.03	2.93×10^4	0.051
22E	0.058	3.26	0.145	6.45	3.04×10^4	0.058
23E	0.058	3.58	0.145	7.14	3.06×10^4	0.053
24E	0.058	3.36	0.145	6.71	3.07×10^4	0.056
25E	0.064	3.22	0.160	6.99	3.33×10^4	0.058
26E	0.065	3.26	0.163	7.11	3.35×10^4	0.058
27E	0.065	3.28	0.163	7.18	3.36×10^4	0.057
28E	0.066	3.09	0.165	6.87	3.42×10^4	0.061
29E	0.071	3.01	0.178	7.07	3.61×10^4	0.062
30E	0.071	2.86	0.178	6.74	3.62×10^4	0.065

Table 4.5: *Characteristics of the experimental tests with e/D = 0.*

CHAPTER 5

Numerical modeling

5.1 Introduction

Another approach to analyze fluid dynamic problems is furnished by numerical model-ing. In this section 5, two different numerical approaches will be described to support and extend the experimental investigation as well as to discover physical insights of the near flow field not modeled by the laboratory investigation.

The first numerical model adopted to reproduce the interaction between the cylinder and the solitary waves is the Smoothed Particle Hydrodynamics (SPH). In SPH the flow evolution is described following the motion of a set of fluid particles, resulting in a Lagrangian representation of the fluid. The SPH particles represent a finite mass of the discretised continuum and carry the information about all physical variables which are evaluated at their positions. This numerical model is based on a meshless grid, which represents an advantage when dealing with cases where the structures have a complex geometry and large fluid deformations occur. The other numerical model, used in this thesis, is the OlaFlow model. This Eulerian model is based on a rigid mesh grid. In this case, the correct solution of the problem depends on the mesh generation. Nowadays, grid-based numerical methods are widely applied to different fields of computational fluid mechanics and represent the dominant approach to solve fluid dynamic problems. In addition, the use of OlaFlow model, which is free and open source, enables a less time consuming compared to SPH. In particular, the mean CPU time cost needed to run OlaFlow is about 1/10 of the time iteration cost using SPH. For this reason, just the first test case with e/D about equal to 1 was inspected through SPH.

5.2 Smoothed Particle Hydrodynamics

Owing to the capabilities in simulating complex physical phenomena and the interaction with structures, a diffusive weakly-compressible Smoothed Particle Hydrodynamics (SPH) scheme was adopted to study the present hydrodynamic process and give insights about physical phenomena not analyzed by laboratory tests. SPH currently represents one of the most popular meshless Lagrangian particle model (e.g., [75]) and, over the course of recent decades, has been applied to a broad range of flow processes and fluid-structure interaction problems (e.g., [4], [50]). Due to the presence of a circular shape at the fluid-solid interface, the spatial arrangement of fluid particles in the present SPH model was assessed by a packing algorithm [18]. This procedure has been applied with the aim of reducing the occurrence of unphysical currents altering the near flow field during the flow evolution. To well assess the hydrodynamic forces acting on the cylinder, the acoustic component occurring in the pressure field due to the weakly-compressibility assumption was filtered here through the use of Wavelet Transform (WT) following the recent approach proposed by Meringolo et al. [51].

5.2.1 Weakly-compressible Navier-Stokes equations

Considering a weakly-compressible fluid, the evolution of the flow field is described by means of Navier-Stokes equations written in the following form (e.g., [52]):

$$
\begin{cases}
\frac{D\rho}{Dt} = -\rho \nabla \cdot \mathbf{u} \\[2mm]
\frac{D\mathbf{u}}{Dt} = -\frac{1}{\rho}\nabla p + \mathbf{g} + \frac{1}{\rho}\nabla \cdot \mathbb{V} \\[2mm]
p = c_0^2 \left(\rho - \rho_0 \right)
\end{cases}
\tag{5.1}
$$

where $\mathbf{u}$ represents the fluid velocity, p the pressure, ρ the flow density, $\mathbf{g}$ the mass force, ρ_0 the initial density at the free surface, c_0 the initial sound speed and $\mathbb{V}$ the viscous stress tensor.

In System 5.1, a linear state equation, obtained as a truncation to the first order of the Taylor expansion of the so-called Tait equation, links the pressure field to the density one [3]. Under the weakly-compressible assumption (i.e. density variations lower than $1\%\rho_0$ [53]), the differences between the linearized state equation and the Tait one are in practice negligible. Regarding the artificial speed of sound adopted for the simulations, the following constraint has be to satisfied in order to guarantee the weakly-compressible regime (e.g., [53] [19]):

$$
c_0 = \max \ \{10 \max(|\mathbf{u}|), \quad 10\sqrt{gd}\}
\tag{5.2}
$$

For the involved hydrodynamic problem, the characteristic velocity $\mathbf{u}$ of Eq. (5.2) is represented by the wave celerity c [50].

5.2.2 Discretization of weakly-compressible Navier-Stokes equations

The weakly-compressible Navier-Stokes equations given by system 5.1 are here discretized by the δ-SPH model [3] which represents a widely adopted SPH scheme in

different hydrodynamic contexts (e.g., [4] [73] [50] [10]). This formulation presents a diffusive term added to the continuity equation that acts to smooth out a relevant amount of the high-frequency acoustic perturbations occurring in the pressure field. Moreover, it is able to preserve the hydrostatic component with respect to other diffusive schemes in SPH literature (e.g., [52]). As well as the standard SPH models (e.g., [53] [19]), the δ-SPH is able to preserve the mass and conserve both linear and angular momenta. The discrete equations of the δ-SPH model are:

$$
\begin{cases}
\frac{D\rho_i}{Dt} = -\rho_i \sum_j (\boldsymbol{u}_j - \boldsymbol{u}_i) \cdot \nabla_i W_{ij} V_j + D_i \\[2ex]
\frac{D\boldsymbol{u}_i}{Dt} = -\frac{1}{\rho_i} \sum_j (p_i + p_j) \nabla_i W_{ij} V_j + \boldsymbol{g}_i + \alpha c_0 h \frac{\rho_0}{\rho_i} \sum_j \pi_{ij} \nabla_i W_{ij} V_j \\[2ex]
\frac{D\mathbf{r}_i}{Dt} = \mathbf{u}_i + \epsilon_X \sum_j (\mathbf{u}_j - \mathbf{u}_i) W_{ij} V_j \\[2ex]
p_i = c_0^2 (\rho_i - \rho_0), \qquad V_i = \frac{m_i}{\rho_i}
\end{cases}
\tag{5.3}
$$

In system 5.3, the quantities ρ_i, $\mathbf{u}_i$, p_i and $\mathbf{r}_i$ are respectively the density, the velocity, the pressure and the position associated with the i-th particle. The gradient taken with respect to the coordinates of particle i is given by the symbol ∇_i. The particle volume V_i is a function of the density in which the mass m_i is taken constant during the flow evolution. The quantity W_{ij} represents the kernel function, chosen here as Gaussian (e.g., [52]) with a cut-off radius $r = 3h$, where h is the smoothing length. A ratio $h/\Delta x = 4/3$ is adopted, where Δx is the initial particle spacing. The artificial viscosity term π_{ij} in the momentum equation is added to stabilize the scheme being [3]:

$$
\pi_{ij} = \frac{(\boldsymbol{u}_j - \boldsymbol{u}_i) \cdot (\boldsymbol{r}_j - \boldsymbol{r}_i)}{|\boldsymbol{r}_j - \boldsymbol{r}_i|^2 + 0.01h^2}.
\tag{5.4}
$$

considering α an empirical coefficient that defines its magnitude.

The mentioned diffusive contribution in the δ-SPH model is given by the quantity D_i that reads as:

$$
\begin{cases}
D_i = 2\delta h c_0 \sum_j \psi_{ij} \frac{(\boldsymbol{r}_j - \boldsymbol{r}_i) \cdot \nabla_i W_j}{|\boldsymbol{r}_j - \boldsymbol{r}_i|^2} V_j, \\[2ex]
\psi_{ij} = (\rho_j - \rho_i) - \frac{1}{2} \left(\nabla \rho_j^L + \nabla \rho_i^L \right) \cdot (\boldsymbol{r}_j - \boldsymbol{r}_i),
\end{cases}
\tag{5.5}
$$

where the magnitude of the diffusive term is given by the parameter δ, while $\langle \nabla \rho \rangle_i^L$ and $\langle \nabla \rho \rangle_j^L$ are the renormalized density gradients [3].

The updating of particle position was corrected through the application of an XSPH numerical filter in which the parameter ϵ_X represents its magnitude in this correction on the velocity field [53]. System 5.3 was solved using a 4th-order Runge-Kutta integration scheme with a frozen diffusive approach [50]. The time step Δt was calculated on the basis of restrictive conditions linked to the time steps Δt_v, Δt_d and Δt_c due respectively to the presence of diffusive, advective and viscosity terms and was evaluated as follows:

$$\Delta t_v = \frac{\rho h^2}{8\mu}, \; \Delta t_d = 0.425\frac{h}{\delta c_0}, \; \Delta t_c = 2.2\min_i\left(\frac{h}{c_0 + |\mathbf{u}_i| + h\max_j \pi_{ij}}\right) \quad (5.6)$$

To simulate the solid boundaries (i.e., cylinder, bottom flume, wavemaker and final wall), the technique of the fixed ghost particles was implemented [47]. In particular, the left wall of the channel was modeled by moving fixed ghost particles and implemented with Eq. 2.10 to simulate the paddle for wave generation and mobile interpolation nodes follow this solid boundary condition [50]. It is worth noting that near solid bodies the support of the kernel function is cut by the body profile and the interpolation accuracy decreases due to the fact that the sum of kernel function is not equal to 1. For this reason, the adopted technique was applied to make up for the loss of mass and, at the same time, to impose correct boundary conditions. To calculate the physical quantities attributed to each fixed ghost particle at each time step, a Moving Least Square (MLS) interpolation over the fluid particles values centered on their interpolation nodes was carried out (e.g., [8]).

5.2.3 Hydrodynamic forces at body profile

The numerical horizontal and vertical hydrodynamic forces were evaluated on the basis of the dynamic pressures acting on the circular cylinder and measured by virtual gauges. For the m-th numerical pressure gauge located along the body profile, the following discrete formulation was adopted to evaluate Δp [50]:

$$\Delta p_m = \sum_{j\epsilon\Gamma} [p_j - (d - z_j)\rho_0 g]\,\tilde{W}(\boldsymbol{r}_m - \boldsymbol{r}'_j)V_j. \quad (5.7)$$

where Γ is the support area involving j-th fluid particles, $\boldsymbol{r}$ is the position of the numerical gauge and $\boldsymbol{r}'$ is the position of the considered fluid particle. As performed to model the solid boundaries through the fixed ghost particle approach, the dynamic pressures at body profile are obtained in Eq. 5.7 considering a weighting function, $\tilde{W}$, corrected with an MLS technique [8]. The interpolating function and the type of support area are the same as those adopted in the governing equations (see section 5.2.2). Along the lines of the experimental approach (see Eq. 4.1), the numerical forces, F_H and F_V, are then evaluated as:

$$
\begin{cases}
F_H = \displaystyle\sum_m^{n/4} a_m[\Delta p_m + \Delta p_{n/2-m+1} - \Delta p_{n/2+m} - \Delta p_{n-m+1}] \\[2em]
F_V = \displaystyle\sum_m^{n/4} a_m[\Delta p_{n/4-m+1} + \Delta p_{3n/4+m} - \Delta p_{n/4+m} - \Delta p_{3n/4-m+1}]
\end{cases}
\quad (5.8)
$$

where n is the total number of pressure gauges, while the influence areas, a_m, are evaluated as:
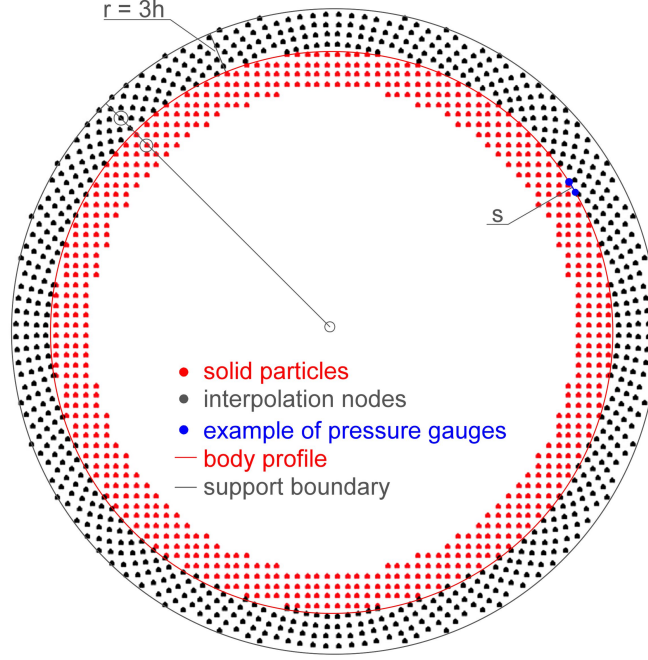
Figure 5.1: *Solid particles simulating the cylinder and associated interpolation nodes.*

$$a_m = \int_{\pi/2-m2\pi/n}^{\pi/2-(m-1)2\pi/n} \frac{D}{2} cos\beta d\beta \qquad \text{for } m = 1, n/4 \qquad (5.9)$$

where Eq. (4.1) adopted for laboratory tests is recovered for $n = 12$.

Fig. 5.1 shows the placement of the solid particles simulating the cylinder in a Cartesian grid with the associated interpolation nodes mirrored with respect to the circular shape of the body profile. To accurately calculate the hydrodynamic forces at the body profile, the mutual distance of pressure gauges belonging the body profile of the cylinder was assumed at an arc length, s, greater than Δx.

5.2.4 Particle Packing Algorithm

Using canonical tessellations in SPH to initialize the spatial placement of the fluid particles (Cartesian, triangular, hexagonal, etc.), the presence of a not-straight shape, i.e. the circular cylinder, coupled with the truncation of kernel support leads to the generation of a spurious and sometimes significant kinematic field close to the boundary. This drawback is induced by the inaccuracy in modeling the pressure gradient through SPH (e.g., [58]). In the present context, the resulting flow motion around the cylinder induced by the action of a solitary wave is then affected by the presence of a superimposed particle resettlement.

To have an initial equilibrium position of the particles, the Particle Packing Algorithm (PPA) developed by Colagrossi et al. [18] allows for recovery of the consistency of the SPH pressure operator. This procedure was applied before the use of system 5.3. The first operation is to close all the boundaries of the computational domain including the free surface, while the second one refers to the assumption of constant values of density ρ_0, pressure p_0 and volume V_0. The last quantity is given by the ratio between

the total fluid volume and the total fluid particles, while p_0 and ρ_0 can be arbitrarily set. Since the static solution must be reached, the above PPA is only governed by the following momentum equation written for 2D problems as:

$$
\begin{cases}
\rho_i \dfrac{D\mathbf{u}_i}{Dt} = -\beta \sum_j \nabla_i W(\mathbf{r}_{ij}) \, V_0 - \zeta \mathbf{u}_i \\[4mm]
\dfrac{D\mathbf{r}_i}{Dt} = \mathbf{u}_i
\end{cases}
\tag{5.10}
$$

in which $\beta = 2p_0/\rho_0$ and ζ represents a linear damping term given by:

$$
\zeta = \alpha_p \sqrt{\frac{\beta}{V_0}}
\tag{5.11}
$$

where the parameter α_p represents the magnitude of the damping term. Colagrossi et al. [18] heuristically found that a good choice for the coefficient dealing with the magnitude of the damping term, α_p, ranges between 10^{-3} and $5*10^{-3}$. We observed that values of α_p in this range give same results (i.e. convergence toward a stable particle configuration) and very small differences in the computation cost to run PPA were related to the time to reach the fixed velocity threshold which is dependent on the magnitude of the velocity field of the specific problem. Then, a mean value of $\alpha_p = 3*10^{-3}$ was here chosen. Note that the updating of particles position is not filtered through the XSPH correction (see system 5.3) since the application of PPA is not addressed to smooth out the velocity field. For 2D cases, the used time step is calculated as follows:

$$
\Delta t_p = CFL_p \sqrt{\frac{V_0}{\beta}}
\tag{5.12}
$$

where $CFL_p = 1$ [18].

With reference of the magnitude of the velocity field at the cylinder of the involved numerical and experimental tests (maximum velocity of order of 10^{-1} m/s), the packing procedure is stopped when the maximum velocity of the particles is lower than 10^{-4} m/s. Fig. 5.2a illustrates the time evolution of the resettlement process of fluid particles, initially placed in a Cartesian grid and subjected to PPA, in terms of maximum intensity of velocity, $\max_i |u_i|$, occurring in the fluid domain. The symbol t_p refers to the time evaluated through the specific Δt_p of PPA by Eq. 5.12. As expected, a progressive decreasing of the velocity can be observed until the set threshold velocity, highlighted with a horizontal dashed line, is reached. The final arrangement of the water particles in a stable position around the cylinder is highlighted in Fig. 5.2b. After the application of PPA, the solid boundary covering the free-surface is deleted and the hydrostatic pressure is assigned, allowing for the possibility to start the SPH simulation using the final configuration of the stabilized fluid particles of Fig. 5.2b. The differences between a simulation run with and without the initialization of the fluid particles through the packing algorithm are illustrated in Fig. 5.2c by inspecting the maximum intensity of velocity in a control area 0.2 m x 0.2 m surrounding the cylinder. The results refer to
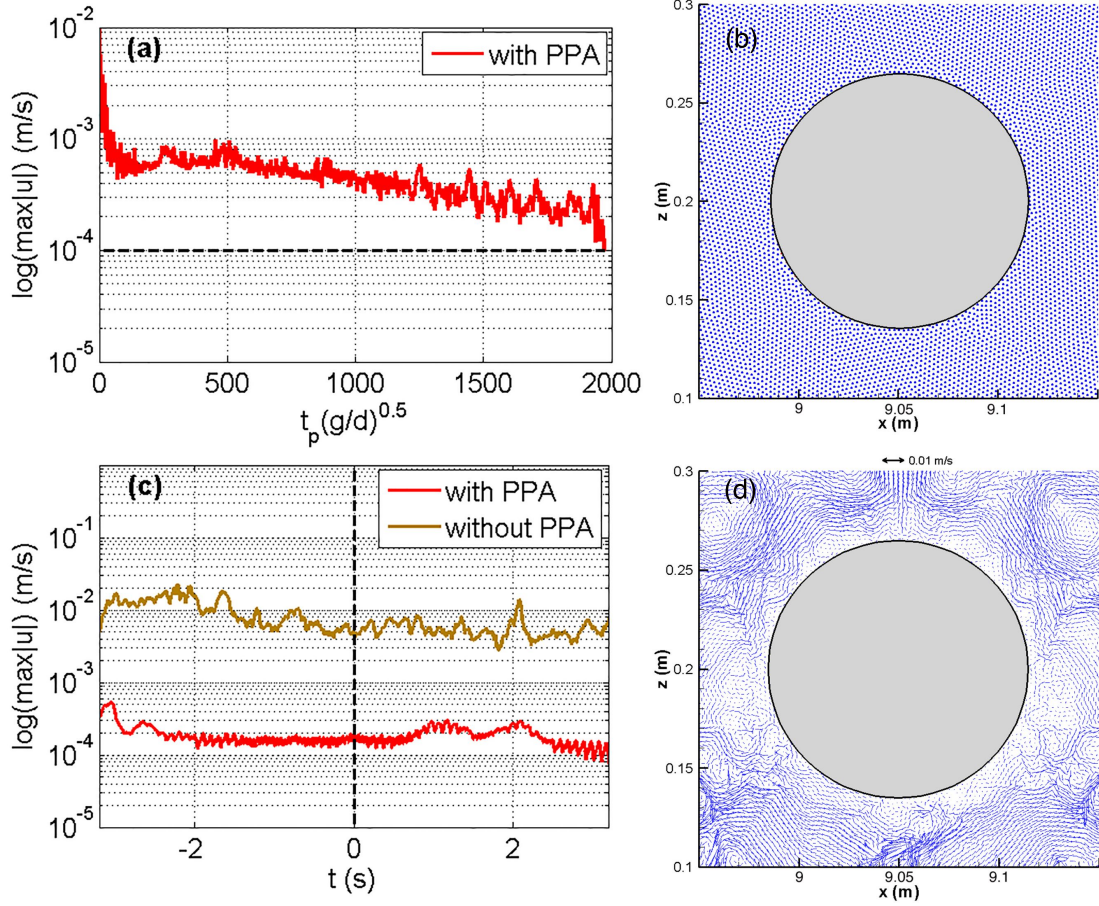
Figure 5.2: *(a) Time variation of maximum intensity of velocity of SPH fluid particles when subjected to PPA; (b) Arrangement of SPH fluid particles around the cylinder at the end of the application of PPA; (c) Time variation of maximum intensity of velocity of SPH fluid particles in hydrostatic conditions with and without PPA; (d) Velocity vectors of SPH fluid particles around the cylinder without PPA for t = 0.*

a hydrostatic test (no wave generation from the paddle) for a time window comparable with the studied wave-structure process. The reference time $t = 0$, highlighted with a vertical dashed line, corresponds to the time instant in which, in the case of a wave generation, the wave crest would have passed at the vertical axis of the cylinder. This assumption is in accordance with the successive definition of $t = 0$ in the analyses involving solitary waves. In the SPH simulation with PPA, the magnitude of velocity is just above the threshold adopted for PPA with values close to 10^{-4} m/s. Conversely, a random velocity field due to the particle resettlement of order of 10^{-2} m/s is noticed in the SPH simulation without PPA. For $t = 0$, the velocity field and the associated velocity vectors without the application of PPA is shown in Fig. 5.2d where spurious current fields occurring around the cylinder would influence the real flow due to the wave motion. In the case of the use of PPA, the particles configuration at $t = 0$ remains practically unchanged with respect that in Fig. 5.2b. It can be finally observed that the mean CPU time cost needed to run PPA is about 1/20 of the whole time iteration cost.

5.2.5   Filtering of pressure data

The assumption of an artificial compressibility is the basic hypothesis for most of the weakly-compressible SPH models where the artificial sound speed is chosen as much lower than the real one but much higher than the characteristic flow velocity to fulfill the weakly-compressible assumption [53]. As observed by Meringolo et al. [51], the pressure field can be expressed as the superimposition of an incompressible solution and an acoustic perturbation in the limit of Ma (Mach number) $\rightarrow 0$. As a result, the acoustic pressure perturbations in this Lagrangian variant are related with the fictitious value of c_0 resulting in a non-physical contribution. The pressure solution is then affected by these acoustic oscillations which should be correctly removed.

A suitable tool to provide the operation to split the hydrodynamic and the acoustic components can be represented by the Wavelet Transform (WT) [24]. In the presence of non-stationary pressure signals and possible spurious effects due to the trailing waves represented as irregular wave packets, the WT proves to be an efficient instrument to remove these unwanted fluctuations and also allows expression of the frequency contents in time. In this sense, the wavelet analysis offers also an advantage in directly controlling the cut-off frequency. The nature of hydrodynamic problems contains frequently unsteady and irregular characteristics that makes the classical Fourier analysis unfruitful for these purposes. Indeed, the Fourier Transform (FT) is suitable for analyzing periodic signals but is less useful when the signal becomes non-stationary. Moreover, when transforming to the frequency domain with the FT, time information is lost unless moving time-window algorithms are used. For example, moving average filters (MAF) are based on specific functions and a study should be done in order to find suitable functions for the MAF. Furthermore, an appropriate setting of parameters is also needed, the main one is the time window span where the averages are evaluated. Indeed, the choice of the time window span could be linked to known quantities such as the initial sound speed and the spatial resolution in order to give a practical method to well decompose the incompressible solution from the acoustic one. A first example of filtering procedure using MAF was carried out by Wei and Dalrymple [77] where SPH was successfully compared with an analytical solution in the case of a hydrostatic force acting on a vertical wall of a water tank.

Among the families of shape functions adopted in the wavelet framework for fluid dynamic problems, a Mexican hat wavelet is heuristically selected (e.g., [34]). This is motivated by two reasons: the curvature of the observed solitary wave forces better resembles that related to its basic function and the spurious "Gibbs-like" effect is avoided in the presence of fast changes of pressure (see, for more details, [51]). The mother wavelet, ψ, of the Mexican hat is represented by the negative Laplacian of a Gaussian function:

$$\psi = (1 - t^2)e^{\left(-t^2/2\right)} \tag{5.13}$$

The decomposition between the acoustic components and the exact incompressible solution proves to be difficult matter for cases involving strong wave impacts on structures since very short-time pressure impulses occur. Therefore, the inertial and acoustic components cannot be decoupled. Here, a pressure wave interacts with a submerged obstacle with resulting slower dynamics. In this case, the spurious acoustic waves can be easily filtered by setting the following cut-off frequency, f_{cut}:
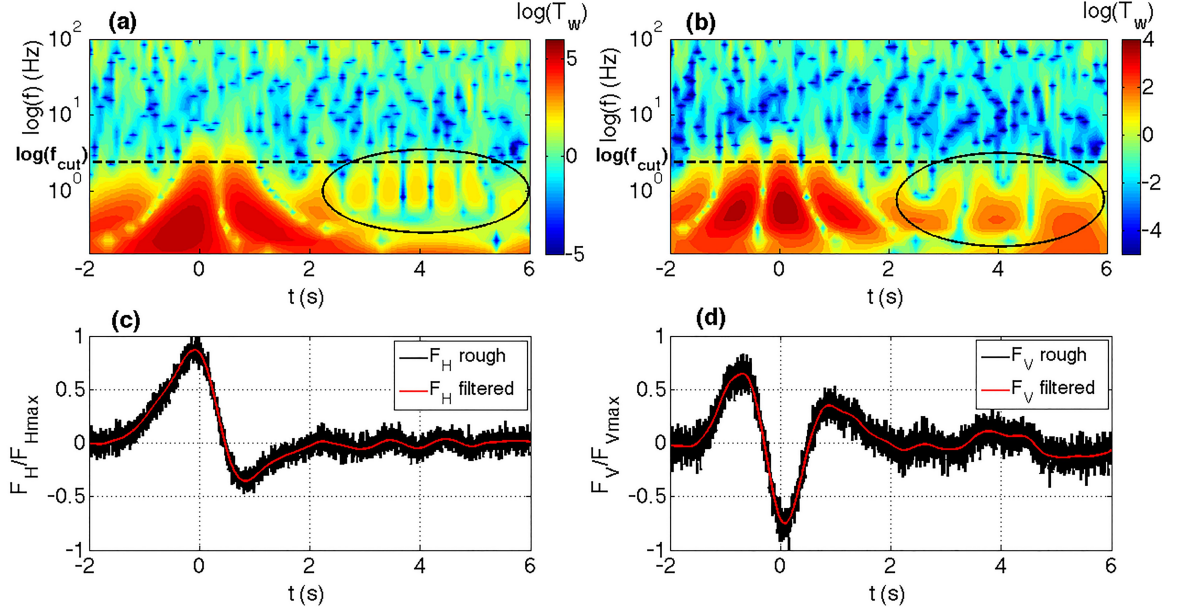
Figure 5.3: *(a) Wavelet coefficients of raw numerical horizontal force, F_H (test no. 13A), (b) Wavelet coefficients of raw numerical vertical force, F_V (test no. 13A), (c) Raw and filtered numerical signal of horizontal force, F_H (test no. 13A), (d) Raw and filtered numerical signal of vertical force, F_V (test no. 13A).*

$$f_{cut} = c_0/\lambda \tag{5.14}$$

that represents the lowest frequency in which the spurious acoustic oscillations arise in the pressure solution. In particular, f_{cut} is the frequency associated to the length of the fluid domain, $\lambda = 2L_c$, being L_c the length of the numerical channel.

In a weakly-compressible SPH model, the numerical oscillations linked to the acoustic components appears in the frequency band ranging from f_{cut} to $f_{max} = c_0/2\Delta x$, being the latter the highest frequency that is related to the interparticle distance [2]. The adopted spatial resolution and the choice of the artificial sound speed have ensured a well-defined splitting between the physical pressure solution and numerical noise. We also highlight that a Savitzky-Golay FIR smoothing filter is also adopted choosing a polynomial of order 3 with a span of about 300 points using $c_0 = 50$ m/s and a spatial resolution $d/\Delta x = 175$. This approach leads to similar results to those given by the use of a Mexican hat wavelet, even if depending on the adopted SPH variant (in this case, the δ-SPH model).

The filtering using the Mexican hat wavelet is therefore applied by cutting the energy contents linked with frequencies higher than f_{cut}. For the representative numerical test no. 13A ($e/D = 1$), Figs. 5.3a and 5.3b show respectively the wavelet coefficients, T_w, occurring in the time variation of the simulated horizontal and vertical forces acting on the horizontal cylinder for the passage of a solitary wave. The horizontal dashed line corresponds to f_{cut} given by Eq. 5.14. The time window related to the occurrence of the hydrodynamic loads given by the passage of the solitary wave on the cylinder is followed by low-energetic spurious wave forces, highlighted through a black ellipse in Figs. 5.3a and 5.3b. These unwanted contributions are induced by the trailing waves

at the free surface which are derived from the truncation in the time law of the mobile solid boundary simulating the paddle motion [32]. With reference to the log scale of the wavelet coefficients, the highest positive values of T_w appear in correspondence of the peaks of the horizontal and vertical hydrodynamic loads. High positive values of the wavelet coefficients mean either a positive or negative correlation between the numerical signal and the wavelet for a given frequency f (i.e. when signal and wavelet are in phase or anti-phase). The negative values of T_w are linked to the numerical noise. Figs. 5.3c and 5.3d illustrate respectively the rough and filtered SPH horizontal and vertical wave loads for the above reference test. The reconstruction of the filtered force signals is obtained by means of the Inverse Continuous Wavelet Transform (ICWT) [74]. It can be noticed that the numerical noise related to the vertical force is higher than the horizontal one since its magnitude is generally lower, as better illustrated in the chapter 6.

5.3 OlaFlow

OlaFlow is a free and open source numerical model which uses the latest advances in the simulation of wave dynamics to the OpenFOAM® and FOAM-extend communities. The model allows to generate and absorb water waves and simulate their interaction with coastal structures. OlaFlow is the development of the two previous versions, IHFOAM and OLAFOAM (see, e.g., [36]). This project is a continuation of the work by Higuera et al. [37] and has overcome limitations and errors in the original OpenFOAM® code. The authors, in this new version, added new functionalities increasing the performance of the solver like the generation of waves and currents simultaneously and the reproduction of multi-paddle piston or flap-type wave generators including the active wave absorption.

5.3.1 Navier-Stokes equations

The OlaFlow CFD suite solves the three-dimensional Reynolds Averaged Navier-Stokes equations (RANS). These equations are solved using a volume of fluid (VOF) technique, through a finite volume discretization. Under the assumption of incompressible fluid, the evolution of the flow field is described by the continuity and momentum conservation equations that are written in the following form [35]:

$$\nabla \cdot U = 0 \tag{5.15}$$

$$\frac{\partial U}{\partial t} + \nabla \cdot (\rho U U) - \nabla \cdot (\mu_{eff} \nabla U) = -\nabla p^* - g \cdot X \nabla \rho + \nabla U \cdot \nabla \mu_{eff} + \sigma \kappa \nabla \alpha \tag{5.16}$$

where U is the velocity vector, ρ is the density, g is the gravity acceleration, X is the position vector, p^* is the pseudodynamic pressure and μ_{eff} is the efficient dynamic viscosity, which takes into account the molecular dynamic viscosity and the turbulence effects. The last term of the equation represents the effect of surface tension, where, σ is the surface tension coefficient, κ is the curvature of the interface and α is the indicator function defined as the quantity of water per unit of volume at each cell. The

last parameter, α, is considered equal to 1 in this work since one-phase flow, i.e. water, is involved to study the present physical process.

The Eqs. 5.15 and 5.16 are solved with a two-step method (predictor-corrector scheme). The turbulence effects are accounted in the equations as an additional eddy viscosity. OlaFlow permits to use different turbulence models. In this thesis the simulations were performed using a k - ϵ model which is one of the most widely used in CFD (e.g., [36], [81]).

Experimental and numerical results

6.1 Introduction

The experimental and numerical forces induced by the interaction between solitary waves and submerged circular cylinders will be first compared and then analyzed. Successively, the validated SPH and OlaFlow results will be adopted to calibrate the hydrodynamic coefficients in Morison and transverse semi-empirical relationships.

On the basis of the comparison between experimental and numerical results, the parameters involved in the SPH equations are calibrated as: $\alpha = 0.01$, $\epsilon_X = 0.25$ and $\delta = 0.1$. The diffusive term, the artificial viscosity and the XSPH correction go to zero as the spatial resolution increases (i.e. when h goes to zero), recovering the consistency with the weakly-compressible Navier-Stokes equations (e.g., [48] [51]). For this reason, different spatial resolutions were tested to heuristically check the numerical convergence of the present Lagrangian variant. In particular, spatial resolutions using $d/\Delta x = 100$, 140, 160 and 175 were adopted to verify the performances of the numerical model and then to reach a solution sufficiently close to the convergent limit. We noticed that the SPH results of surface elevations and pressures at the cylinder adopting $d/\Delta x = 160$ and 175 were practically superimposed and this guarantees that the influence of the above empirical parameters is negligible. The adopted spatial resolution $d/\Delta x = 175$ leads to a resulting number of pressure gauges along the body profile of the cylinder equal to 144. The initial sound speed $c_0 = 50$ m/s is here chosen under the constraint expressed by Eq. 5.2 and considered as a reliable value to perform a good filtering of pressure data from the numerical noise. Free-slip conditions are implemented along all solid boundaries of the computational domain. All SPH simulations reproducing about 10 s of the involved wave-structure interaction process take a CPU time of about 6 days through a single 3.4 GHz Intel(R) i7-3770 core with 8GB RAM. The computation domain is smaller than the experimental one (see section 4.3) to overcome disadvan-

tages in terms of CPU time. On the basis of the wave celerity of the solitary wave, the length of the numerical flume is taken equal to 12 m so that the reflected waves reach the cylinder section after the time window of the investigated phenomenon. It can be also observed that a parallelized version of the numerical code could be adopted using MPI-OpenMP programming models (e.g., [48]) or GPUs (e.g., [1] [20]) to reduce the overall computation cost.

As regards the OlaFlow model, the length of the numerical flume is taken equal to 12 m as in the SPH model. The longitudinal spatial resolution changes as a function of the distance respect to the cylinder position. At the ends of the mesh grid, Δx is equal to 2 cm, while near the cylinder it is 2 mm. Regarding the vertical spatial resolution, the value of Δz is always 2 mm. The refinement of the mesh grid was necessary to obtain an accurate solution of the incident flow field and the hydrodynamic forces. The changes of the spatial resolution is step-by-step in the transition zones. Also in this case, the numerical convergence was checked by changing the spatial resolution. A sketch of mesh grid using OlaFlow with all the distances and the spatial resolutions is shown in Fig. 6.1. For a total time of 10 s, the OlaFlow simulations take a CPU time of about 6 hours through a 3.7 GHz Intel(R) Xeon(R) E5-1620 core v2 with 8GB RAM.

Except the analysis of the wavemaker displacement, the reference time $t = 0$ corresponds to the passage of the solitary wave crest at the vertical section of the cylinder.
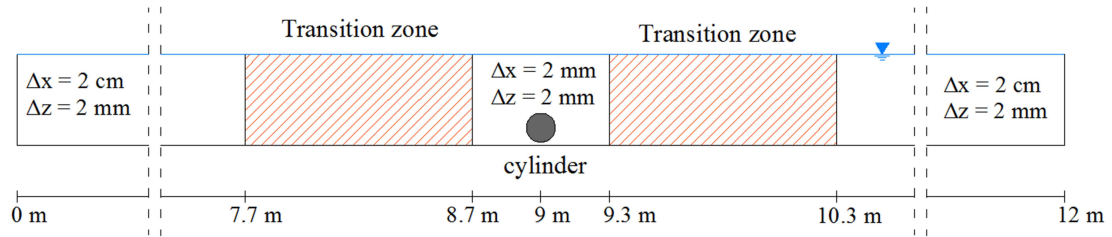

Figure 6.1: *Sketch of mesh grid using OlaFlow.*

6.2 Incident flow field

The assessment of the hydrodynamic forces acting on the horizontal cylinder proves to be dependent on the correct generation and propagation of the incident solitary wave. The suitability of the incident flow field is here checked in terms of generation of the solitary waves by the piston-type wavemaker and of the values of surface elevation and kinematic field in correspondence with the vertical axis of the cylinder.

With reference to the representative experimental test no. 14A (see Tab. 4.1, $e/D = 1$), the experimental horizontal displacement of the paddle deduced from the ultrasonic sensor located behind it is compared with the reference analytical solution given by Eq. 2.10. Note that the time $t_X = 0$ corresponds to a wavemaker displacement, $X = S/2$. An overall good agreement between experimental and analytical displacement can be observed in Fig. 6.2. The time law of the piston is forced in the SPH and in OlaFlow by discretizing the analytical solution with the numerical time step.
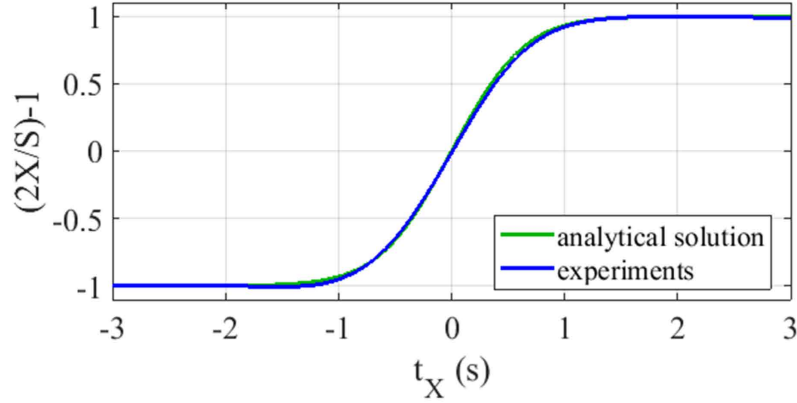
Figure 6.2: *Time law of horizontal displacement of wavemaker, X: comparison between analytical solution and experiments (test no. 14A)*

Fig. 6.3 shows the comparison between the analytical solution given by Eq. 2.2, the experimental and SPH numerical values of the surface elevation at the vertical axis of the cylinder (test no. 14A).
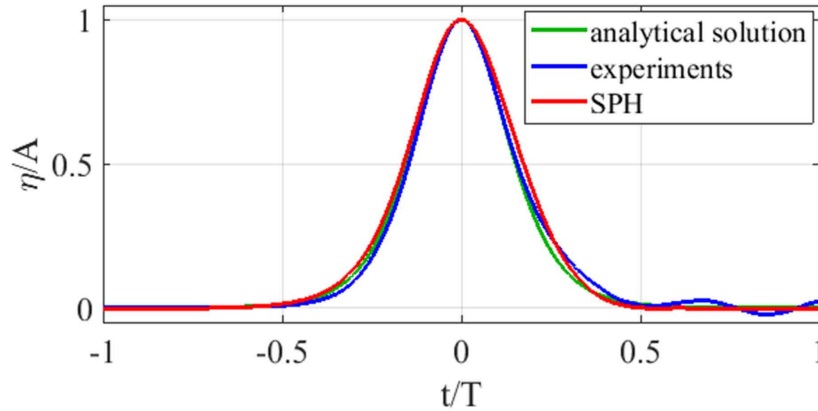

Figure 6.3: *Time variation of surface elevation, η, in correspondence with the vertical axis of the cylinder: comparison between analytical solution, experiments and SPH (test no. 14A)*

A comparison between the surface elevation given by the OlaFlow model, the analytical solution and the experimental values are shown in Fig. 6.4 (test no. 30E).

A general agreement between the approaches in terms of shape and magnitude of the incident solitary wave can be noticed. For both experimental and numerical data, the occurrence of spurious trailing waves, due to the instantaneous truncation in the time law of the paddle motion, were minimized at values within 3% of the incident wave amplitude for both crests and troughs and in any case lower than the critical threshold of 5% suggested by Guizien and Barthélemy [32]. For the mentioned test no. 14A, Fig. 6.5 shows the comparison between analytical solution, experiments and SPH regarding the time history of the undisturbed kinematic field in correspondence with the transversal axis of the cylinder.

Starting from surface elevations displayed in the previous Fig. 6.3, the three solutions are deduced from the application of the Eqs. 2.6 in which a_H and a_V are
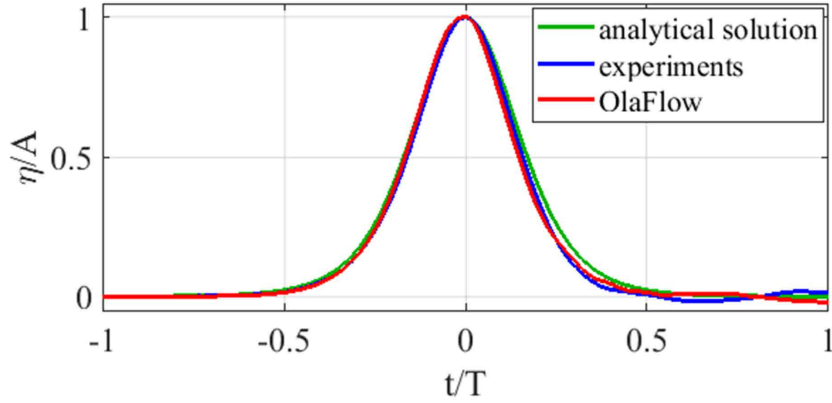
50

Figure 6.4: *Time variation of surface elevation, η, in correspondence with the vertical axis of the cylinder: comparison between analytical solution, experiments and OlaFlow (test no. 30E)*
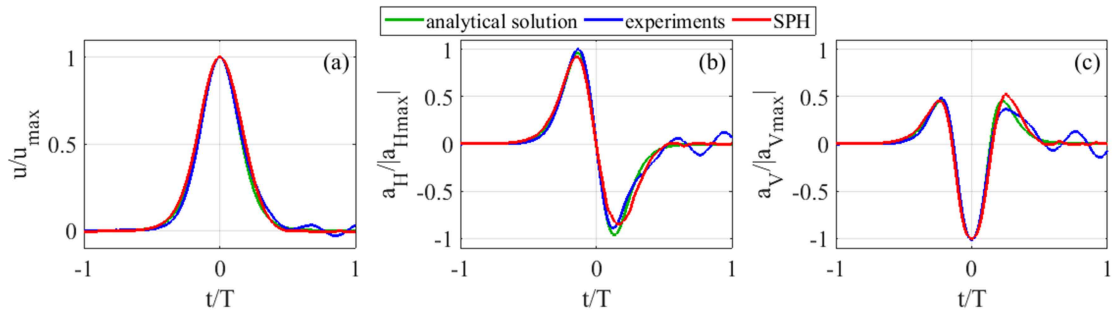

Figure 6.5: *Time variation of free stream kinematic field at the transversal axis of the cylinder: comparison between analytical solution, experiments and SPH (test no. 14A). (a) Horizontal velocity, u; (b) horizontal acceleration, a_H; (c) vertical acceleration, a_V.*

respectively derived from u and v. The specific depth ($z = D/2$) is chosen since the semi-analytical Morison and transverse approaches depend on the kinematic field at this location (see Eqs. 3.6 and 3.7). The same approach is used for the OlaFlow model and for the other four values of e/D, and a comparison between the analytical solution, the experiments and OlaFlow is shown in Fig. 6.6 for a representative test case (test no. 30E). The horizontal velocity u is highlighted in Figs. 6.5a and 6.6a where its shape follows η. The horizontal acceleration, a_H, presents equal positive and negative peaks (Figs. 6.5b 6.6b), while the vertical acceleration, a_V, presents a double positive peak and a greater negative one (Figs. 6.5c 6.6c). The main aim of this analysis is to highlight the shape of u, a_H and a_V and how they influence the consequent feature of the experimental and numerical solitary wave loads in both direction as a function of the considered range of A/d. The importance of the kinematic field will also be highlighted in the application of semi-empirical force models in which the different horizontal and vertical force components prove to be directly proportional to the shapes of u, a_H and a_V. The general accordance observed in Figs. 6.3 and 6.4 for η can be also observed for the kinematics at the cylinder apart a small deviation of the experimental and numerical free stream kinematics with respect to the analytical solutions during the decay phase. This allows for the possibility to adopt the free stream kinematic field to calibrate the hydrodynamic coefficients in the Morison and transverse schemes as well as to apply
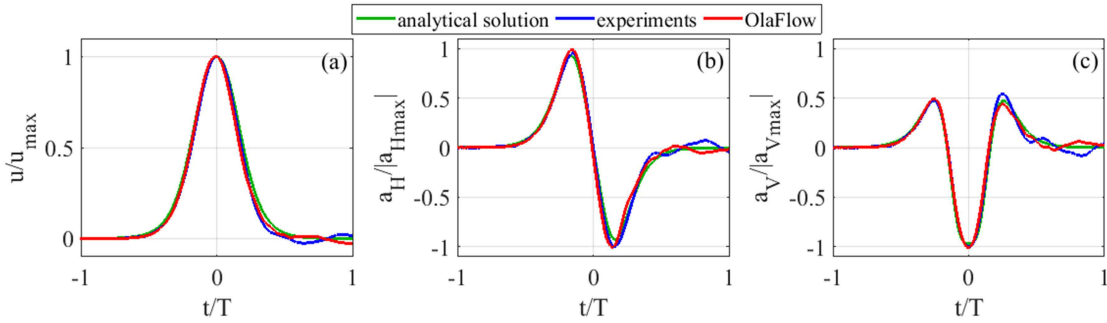
Figure 6.6: *Time variation of free stream kinematic field at the transversal axis of the cylinder: comparison between analytical solution, experiments and OlaFlow (test no. 30E). (a) Horizontal velocity, u; (b) horizontal acceleration, a_H; (c) vertical acceleration, a_V.*

it to reproduce the performed experimental and numerical tests in a simplified way. It can be noticed that the suitability of Eq. 2.6 is also checked at the transversal axis of the cylinder by using SPH and OlaFlow without the presence of the involved structure.

6.3 Hydrodynamic forces

In this section the experimental and numerical forces will be compared and analyzed. In particular, in the first subparagraph, the comparison between SPH and experiments in the case of $e/D = 1$ will be presented. Then, for the other four depths ($e/D = 0.5$, $e/D = 0.25$, $e/D = 0.1$ and $e/D = 0$) the comparison between the OlaFlow model and the experimental values will be showed.

6.3.1 Experimental and SPH forces - e/D = 1

The time variation of the solitary wave-induced forces acting on the horizontal cylinder from the analyzed laboratory tests and SPH simulations in the case where $e/D = 1$ is here illustrated. As presented in Fig. 6.7, two experimental and numerical test cases are taken into account. The first one refers to a smaller wave attack (test no. 1A, $A = 0.032$ m and $T = 4.10$ s), while the second one is characterized by a greater wave attack (test no. 14A, $A = 0.071$ m and $T = 3.21$ s). The agreement between experiments and SPH is quite satisfactory on the magnitude and the related phase shift of the maximum loads in both cases, particularly for the higher wave attack. It can be noticed that the maximum peak of the horizontal force is greater than the vertical one, revealing that the cylinder is substantially subjected to the action of the forward motion of the solitary wave for $e/D = 1$. With reference to the wave crest at the cylinder section highlighted as vertical dashed lines in Fig. 6.7, the positive peak of the horizontal force is back shifted, while the negative one is forward shifted. The maximum peaks of F_H and F_V tend to the maximum values of a_H and a_V, respectively. In particular, the lower wave attack shows these peaks much close to a_H and a_V. Thus, the inertia component dominates the characteristics of the horizontal and vertical wave forces in the present range of A/d. Indeed, the shapes of the total wave loads tend to follow those related to the undisturbed accelerations at the cylinder (see Fig. 6.5), with smaller contributions given by the drag and the lift forces. In particular, the drag component tends to reduce the negative peak of the horizontal force, while the lift one leads to a slight decrease of

the maximum negative peak. These findings are strictly linked to what appears when regular or irregular waves interact with horizontal cylinders in a similar range of the parameter KC in which the inertia components strongly influence the characteristics of the total forces (e.g., [69] [6] [7]). The weight of the different force components will be better analyzed through the successive application of the semi-empirical equations allowing to reconstruct the components acting on both directions.
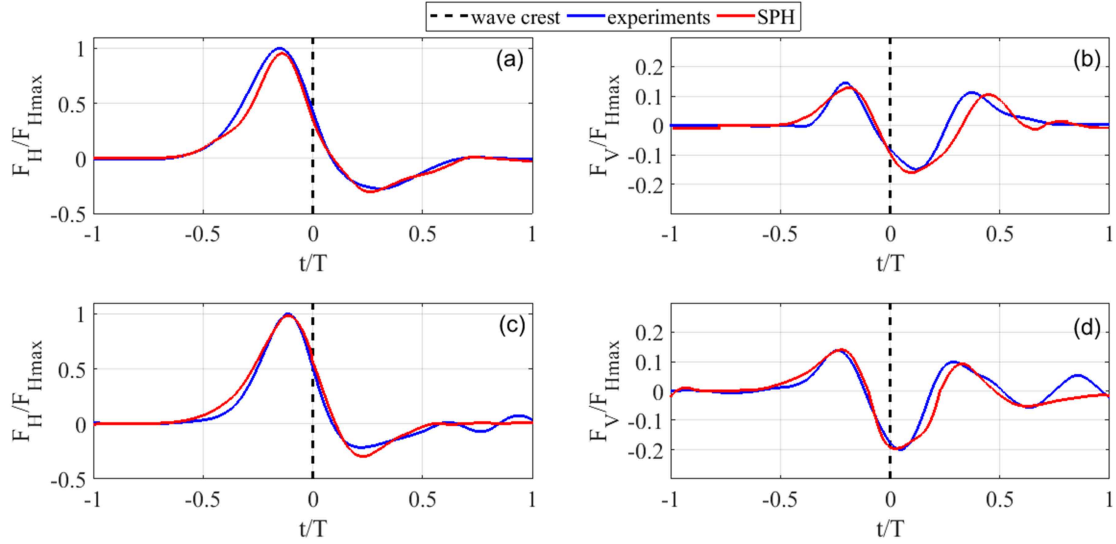

Figure 6.7: *Time variation of experimental and numerical hydrodynamic forces, F_H and F_V ($e/D = 1$). (a) Horizontal force (test no. 1A); (b) vertical force (test no. 1A); (c) horizontal force (test no. 14A); (d) vertical force (test no. 14A).*

Considering the whole experimental and numerical dataset (Tab. 4.1, $e/D = 1$), the positive and negative maximum horizontal, $F_{Hmax,p}$ and $F_{Hmax,n}$, and vertical, $F_{Vmax,p}$ and $F_{Vmax,n}$, forces as a function of A/d are respectively plotted in Figs. 6.8a and 6.8b. The force peaks are respectively normalized with respect to the maximum (positive) peak of the horizontal force, $F_{Hmax}*$, and the maximum (negative) peak of the vertical force, $F_{Vmax}*$. In the overall good agreement between the laboratory tests and SPH, it is possible to observe higher experimental values of $F_{Hmax,p}$ if compared to the corresponding numerical ones and higher numerical values of $F_{Hmax,n}$ compared to the corresponding experimental ones. It has been observed that the first positive peaks of the vertical force are slightly greater than the second ones and therefore considered in the present analysis. The positive and negative peaks in both directions increase proportionally to A/d with a greater variation for higher wave amplitudes. In the analyzed range of A/d, $F_{Hmax,p}$ shows a general increase of 72% and $F_{Hmax,n}$ of 24%, while $F_{Vmax,p}$ and $F_{Vmax,n}$ also growth of about 50% and 92%, respectively. The successive Fig. 6.8c illustrates the weight of the maximum vertical force with respect to the horizontal one as a function of A/d. With reference to $F_{Hmax,p}$, the contribution of $F_{Vmax,n}$ ranges from 14% for smaller A/d to 27% for larger A/d. A better-defined trend can be noticed by the SPH results.

An additional analysis to check the observed features of the total wave loads was carried out in terms of horizontal and vertical forces acting on each half part of the cylinder. Laboratory tests were considered to analyze the features of the wave forces in
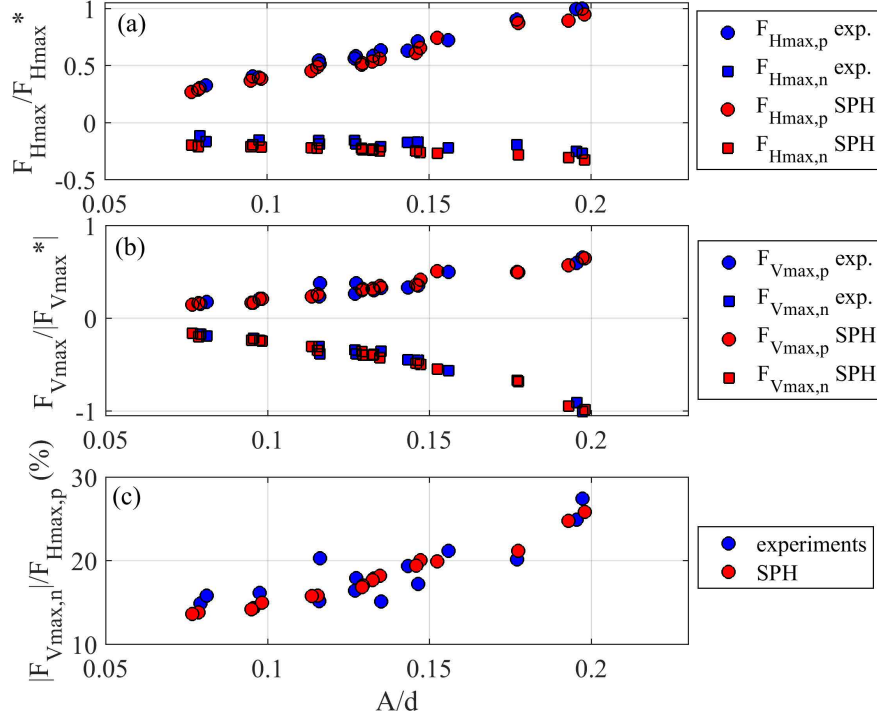
53

Figure 6.8: *Maximum positive and negative peaks of experimental and numerical hydrodynamic forces vs. A/d (e/D = 1). (a) horizontal force; (b) vertical force; (c) weight of vertical force with respect to horizontal one.*

this condition. As shown in Fig. 6.9a, the horizontal force, F_H, acting on the cylinder can be given by the difference between the horizontal component acting on the wave beaten half-cylinder A, F_{HA}, and that related to the sheltered half-cylinder B, F_{HB}. The pressure transducers are numbered from 1 to 6 on the wave beaten half-cylinder A and from 7 to 12 on the sheltered half-cylinder B. On the basis of the experimental pressure sensors belonging to each half-cylinder, the values of F_{HA} and F_{HB} are calculated as:

$$\begin{cases} F_{HA} = a_1 \left(\Delta p_1 + \Delta p_6 \right) + a_2 \left(\Delta p_2 + \Delta p_5 \right) + a_3 \left(\Delta p_3 + \Delta p_4 \right) \\ \\ F_{HB} = a_1 \left(\Delta p_7 + \Delta p_{12} \right) + a_2 \left(\Delta p_8 + \Delta p_{11} \right) + a_3 \left(\Delta p_9 + \Delta p_{10} \right) \end{cases} \tag{6.1}$$

Fig. 6.9b highlights the time variation of the experimental horizontal forces on the half-cylinders, F_{HA} and F_{HB}, for the tests no. 1A and 14A. The forces are plotted with the respect to the maximum force, F_{max}, given by test no. 14A. With respect to the occurrence of the wave crest centered at $t = 0$, the magnitude of the peaks is back shifted for the half-cylinder A and forward shifted for the half-cylinder B. In the expected time shift, a small reduction of the maximum value of the horizontal force component appears. This effect is given by the resistance offered by the cylindrical body to the incoming wave pressure field (i.e. the appearing of a drag force component and possible additional effects induced by the wave reflection for the presence of the solid obstacle and the occurrence of trailing waves at the free surface). The resulting wave loads deviate therefore from a fully inertia regime, where only a phase shift should be

noticed between F_{HA} and F_{HB}. Indeed, the inertia load is dependent on the horizontal acceleration whose shape is anti-symmetrical compared to $t = 0$ (i.e. equal positive and negative peaks). The vertical force, F_V, can be conversely represented by the difference between the vertical component acting on the lower half-cylinder A, F_{VA}, and that related to the upper half-cylinder B, F_{HB}. Following the image of Fig. 6.9c where the pressure transducers are numbered from 10 to 3 on the lower half-cylinder A and from 4 to 9 on the upper half-cylinder B, F_{VA} and F_{VB} are given by:

$$\begin{cases} F_{VA} = a_1 \left(\Delta p_3 + \Delta p_{10} \right) + a_2 \left(\Delta p_2 + \Delta p_{11} \right) + a_3 \left(\Delta p_1 + \Delta p_{12} \right) \\ \\ F_{VB} = a_1 \left(\Delta p_4 + \Delta p_9 \right) + a_2 \left(\Delta p_5 + \Delta p_8 \right) + a_3 \left(\Delta p_6 + \Delta p_7 \right) \end{cases} \tag{6.2}$$

The time history of F_{VA} and F_{VB} at the semi-cylinders is shown in Fig. 6.9d for the tests no. 1A and 14A deduced by laboratory experiments. In this case, the deviation from a pure inertia load appearing along the depth is lower than that noticed for F_H. The observed small increase and forward shift of the peak force when passing from F_{VA} to F_{VB} can be related to the contribution of the lift force acting towards the free surface.
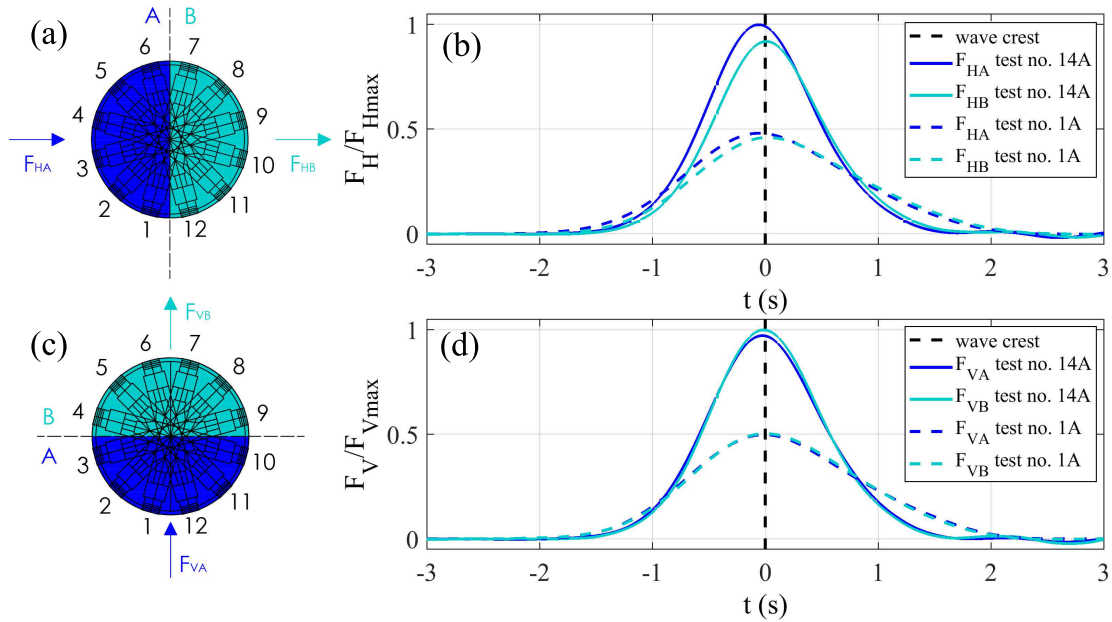

Figure 6.9: *(a) Sketch of the half-cylinders A (blue) and B (cyan) for calculating the horizontal forces. (b) Time variation of the experimental horizontal forces on the half-cylinders, F_{HA} and F_{HB}, for the experimental tests no. 1A and 14A. (c) Sketch of the half-cylinders A (blue) and B (cyan) for calculating the vertical forces. (d) Time variation of the experimental vertical forces on the half-cylinders, F_{VA} and F_{VB}, for the experimental tests no. 1A and 14A.*

The occurrence of drag and lift forces is linked to the formation of vortex patterns behind the cylinder and the consequent deviation from a pure inertial field instead characterized by a potential flow. An insight on the features of the flow field generated by a solitary wave at the horizontal cylinder is given through four significant time instants of the SPH simulations for numerical tests no. 1A and 14A. As highlighted in Fig.

6.10, the selected instants for the involved two cases refer to the passage of the solitary wave crest at the vertical section of the cylinder ($t = 0$), to the central part ($t = 0.7$ s) and to the final part ($t = 1.5$ s) of the descending phase of η. The last instant $t = 2.8$ s is representative of the complete passage of the solitary wave across the cylinder. The values of η are represented with the respect the maximum wave amplitude, A_{max}, given by test no. 14A.
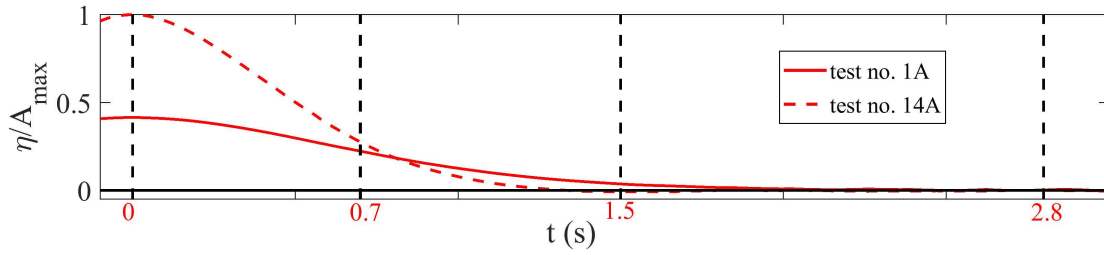

Figure 6.10: *Detail of the surface elevation, η, for numerical tests no. 1A and 14A (significant time instants adopted for SPH simulations are highlighted by vertical dashed lines).*

Figure 6.11: *SPH simulations of vorticity field, ω, and associate streamlines near the cylinder for numerical test no. 1A at t = 0 (a), 0.7 s (b), 1.5 s (c) and 2.8 s (d).*

With reference to the selected time instants, Figs. 6.11 and 6.12 describe the SPH simulations of the vorticity field, ω, and the streamlines around the cylinder for test no. 1A with $KC = 4.82$ and $Re = 1.81*10^4$ and no. 14A with $KC = 7.81$ and $Re = 3.74*10^4$, respectively. Note that in Figs. 6.11 and 6.12 and in the successive Fig. 6.13 the values of ω are converted to unity by D/c.

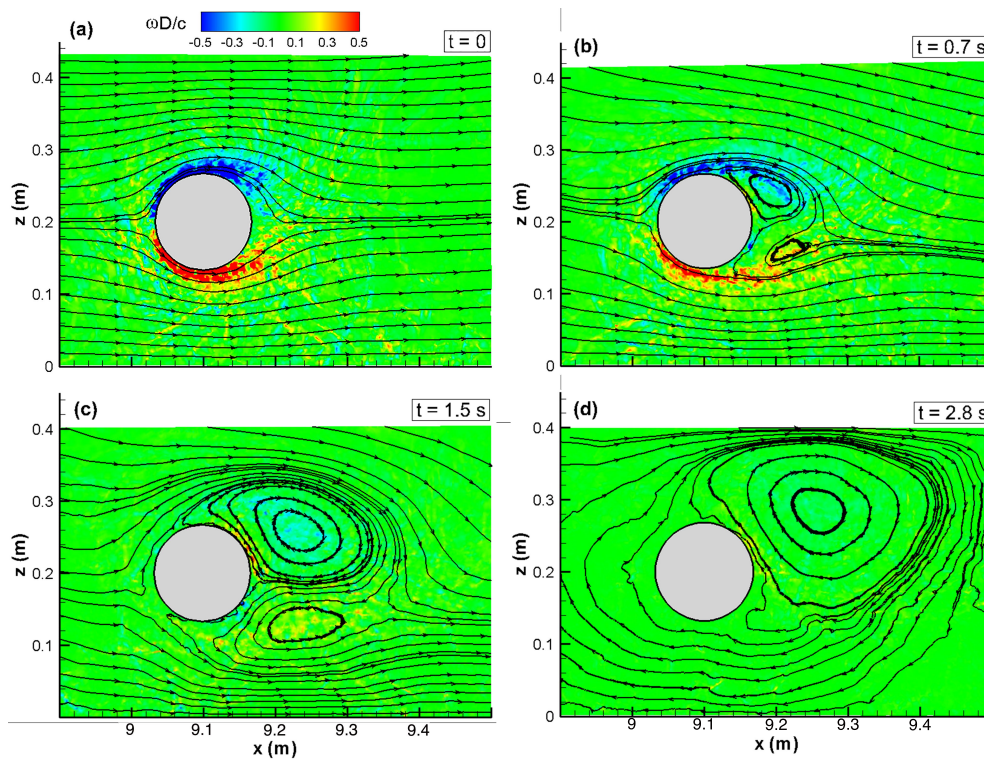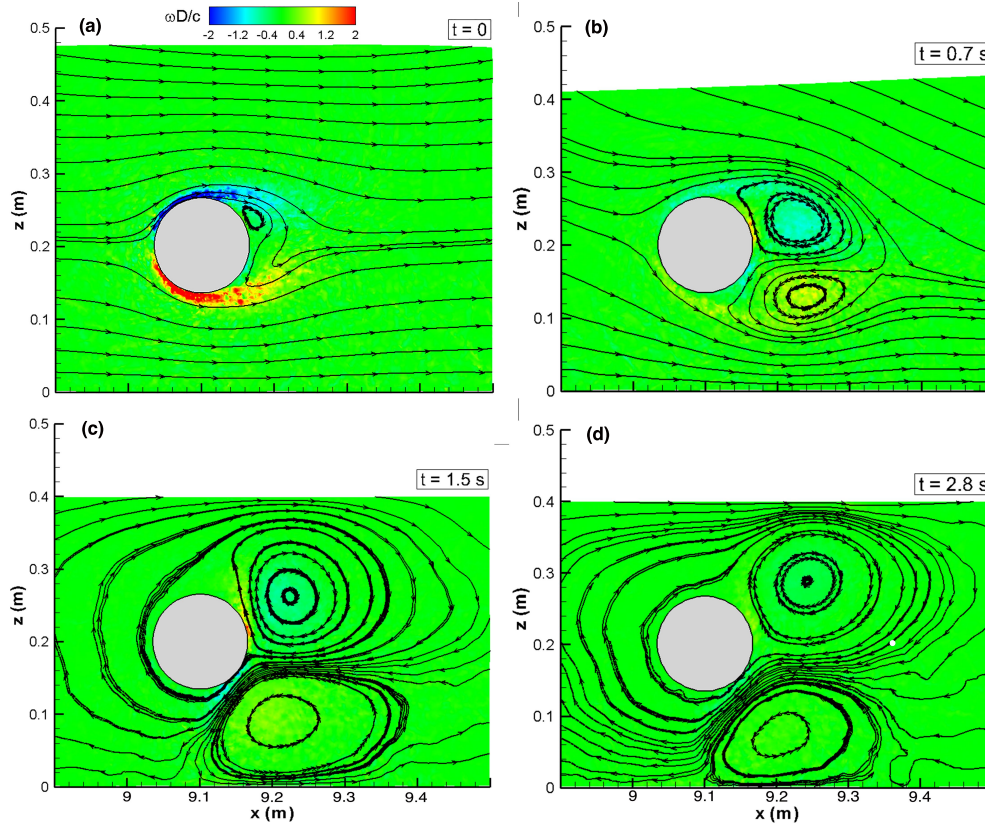This specific location of the cylinder at a half water depth (resulting e/D equal

Figure 6.12: *SPH simulations of vorticity field, ω, and associate streamlines near the cylinder for numerical test no. 14A at t = 0 (a), 0.7 s (b), 1.5 s (c) and 2.8 s (d).*

to 1) has not been investigated in literature unless that of the numerical simulations performed by Lin and Liao [43]. However, in this study, the cylinder was set close to the bottom and therefore the flow evolution was strongly affected by its presence, with a resulting different near field and magnitude of horizontal and vertical forces. For test no. 1A characterized by a lower A, a deviation from the irrotational flow due to the shear layer at the upper and the lower side of the cylinder was noticed at the passage of the crest of the solitary wave for $t = 0$ (Fig. 6.11a). The shear layer at both sides is characterized by a strong clockwise (negative) and anti-clockwise (positive) vorticity. At $t = 0.7$ s, the mentioned shear layer has rolled up inducing a primary lee-wake vortex behind the structure and, for the interaction with the incident flow at the lower side, a secondary vortex (Fig. 6.11b). Owing to the shape of the solitary wave, the vortex in clockwise direction grows larger than the other in anti-clockwise direction. These vortices are then progressively convected far from the cylinder. At $t = 1.5$ s, a growth of the two vortices appears in a wider region behind the cylinder (Fig. 6.11c). At $t = 2.8$ s, the secondary vortex disappears while the primary one grows towards the free surface and generally in the traverse direction (Fig. 6.11d). With reference to the test no. 14A defined by a higher A, a just-formed primary vortex occurs behind the upper side of the cylinder at the passage of the wave crest at its vertical section (Fig. 6.12a). At $t = 0.7$ s, the higher incident flow field yields the growth of the primary vortex and the arising of a secondary vortex close to the lower part of the cylinder (Fig. 6.12b), the

amplitudes of which are higher than that observed for the test no. 1A (see Fig. 6.11b). The resulting flow motion is directed towards the bottom because of the higher incident motion. The subsequent time instant $t = 1.5$ s leads to a progressive increasing of the size of the couple of counter-rotating cells covering the water depth behind the structure where the lower one tends to interact with the bottom channel (Fig. 6.12c). The final frame representing $t = 2.8$ s shows a similar feature of the previous time instant except for a more significant interaction of the vortices with the bottom and the free surface (Fig. 6.12d). With respect to the test no. 1A, the vortices are generally convected in a downstream direction. The pair of asymmetric vortices with a successive shedding regime highlighted for the two tests shows similarities with the case of regular waves for a similar KC range (e.g., [70]). In the investigated range of Re of order of 10^4, the generated wake proves to be completely turbulent and a laminar boundary layer separation occurs in subcritical flow conditions (e.g., [69]).
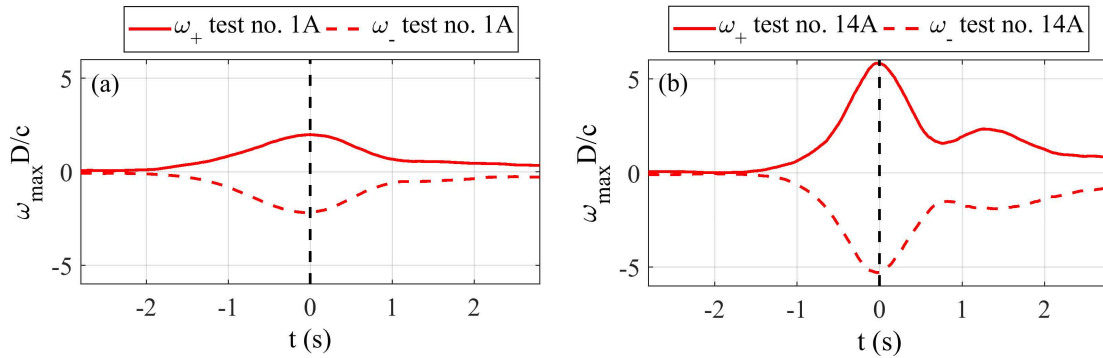

Figure 6.13: *Time evolution of maximum positive, ω_+, and negative, ω_-, vorticity around the circular cylinder for numerical tests no. 1A and 14A.*

However, the passage of a unique wave at the cylinder does not give the occurrence of another vortices in an alternative manner as conversely appears in the presence of a continuous flow, i.e. steady currents and regular or irregular wave trains. The current couple of vortices tends progressively to decrease after the passage of the solitary wave over the cylinder with a dissipation mechanism depending on the magnitude of incident wave motion. This feature is highlighted in Figs. 6.13a and 6.13b in which the time variation of maximum positive, ω_+, and negative, ω_-, vorticity is displayed for the analyzed tests no. 1A and 14A, respectively. A rectangular control section starting from the free side of the cylinder until 0.3 m behind it was considered, i.e. the expected zone where a significant amount of vorticity given the wave-cylinder interaction tends to grow and successively decay. Positive and negative peaks of maximum vorticity occurring respectively at the lower and upper side of the cylinder are very close to the passage of the wave crest, represented by vertical dashed line at $t = 0$, and then related to the greatest horizontal velocity. This means that the force components (i.e. drag and lift) due to the resistance offered by the cylindrical body are also maximum. Moreover, it is noticed that the peak of ω_- is slightly higher than the corresponding value of ω_+. For test no. 14A characterized by higher wave amplitude, the secondary peak of maximum ω_+ and ω_- is related to the occurrence of relevant vorticity just behind the cylinder when the two lee-wake vortex patterns tend to move far from it, as illustrated

in Fig. 6.12c.

6.3.2 Experimental and OlaFlow forces - e/D = 0.5

The time history of solitary wave loads acting on the horizontal cylinder, in the case where the gap-to-diameter ratio is equal to 0.5, is analyzed in this subsection. In particular, Fig. 6.14 highlights the experimental and OlaFlow values of the horizontal and vertical hydrodynamic forces for the selected tests no. 6B and 31B (see Tab. 4.2), respectively.
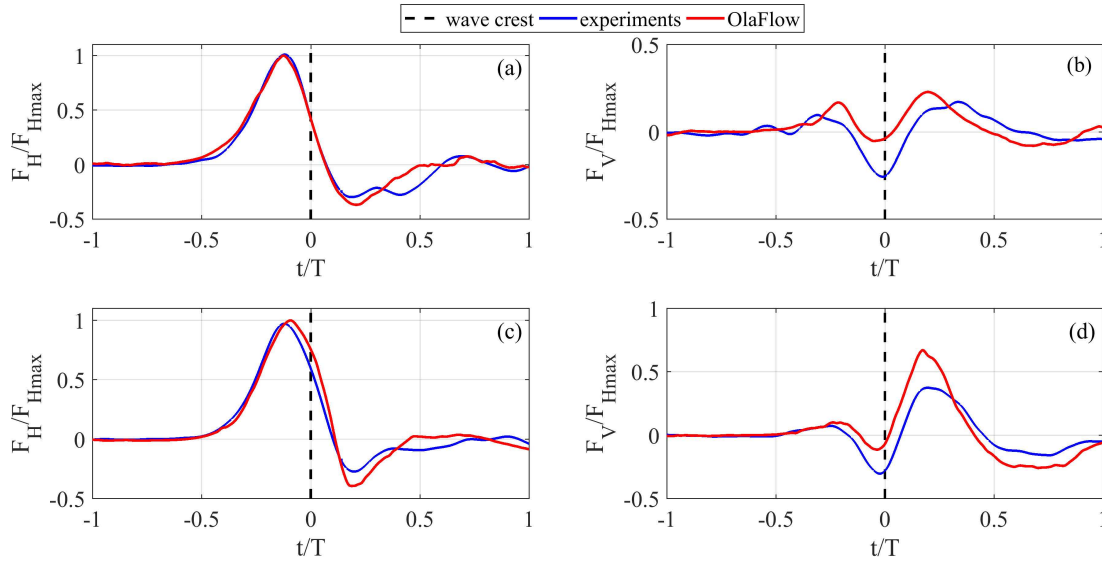

Figure 6.14: *Time variation of experimental and numerical hydrodynamic forces, F_H and F_V (e/D = 0.5). (a) Horizontal force (test no. 6B); (b) vertical force (test no. 6B); (c) horizontal force (test no. 31B); (d) vertical force (test no. 31B).*

The time variation of the horizontal force is comparable with the previous case analyzed (e/D = 1), while the time variation of the vertical force is slightly different and presents a second positive peak greater than the first one. The agreement between the experiments and the numerical simulations of the horizontal hydrodynamic force is good for both examined tests (Fig. 6.14a, Fig. 6.14c). Some differences can be noticed in the vertical force in terms of peaks and associate phase shifts, particularly for the lower wave attack (Fig. 6.14b). Similarity to the case of e/D = 1, the maximum peak of the horizontal force is greater than the vertical one and is back shifted with respect to the wave crest. On the contrary, the maximum peak of the vertical force is forward shifted with respect to the solitary wave crest. Considering the whole experimental and OlaFlow dataset (Tab. 4.2, e/D = 0.5), the positive and negative maximum horizontal, $F_{Hmax,p}$ and $F_{Hmax,n}$, and vertical, $F_{Vmax,p}$ and $F_{Vmax,n}$, forces as a function of A/d are respectively plotted in Figs. 6.15a and 6.15b. The force peaks are respectively normalized with respect to the maximum peak of the horizontal force, $F_{Hmax}*$, and the maximum peak of the vertical force, $F_{Vmax}*$. The Figure 6.15a shows a good agreement between the laboratory and numerical tests for $F_{Hmax,p}$. With reference to Fig. 6.15b, it is possible observe a little difference between the experimental and numerical positive peak of the vertical force, especially for the highest wave attacks. Also in this

case ($e/D = 0.5$), the positive and negative peaks of the forces increase proportionally to A/d. As highlighted in Fig. 6.15c, the weight of the maximum vertical force with respect to the horizontal one ranges from 5% for smaller A/d to 67% for the larger A/d. The experimental weight of the maximum vertical force is slightly lower respect the numerical one and Fig. 6.15c illustrates this little discrepancy.
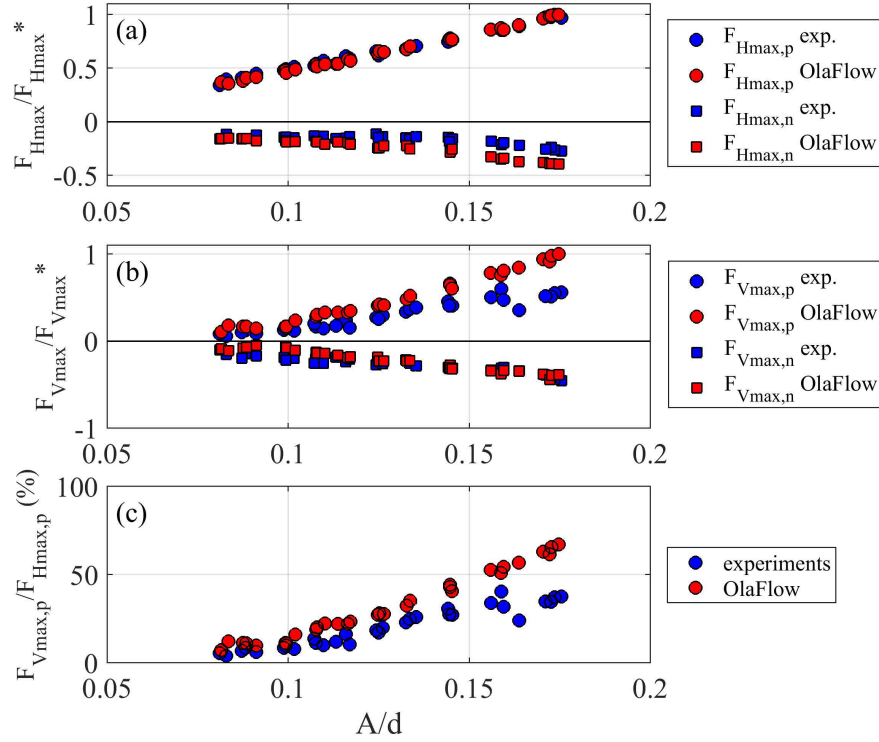

Figure 6.15: *Maximum positive and negative peaks of experimental and OlaFlow hydrodynamic forces vs. A/d (e/D = 0.5). (a) horizontal force; (b) vertical force; (c) weight of vertical force with respect to horizontal one.*

6.3.3 Experimental and OlaFlow forces - e/D = 0.25

In this subsection the time variation of the solitary wave-induced forces acting on the horizontal cylinder from the analyzed laboratory tests and OlaFlow simulations in the case where $e/D = 0.25$ is illustrated. Along the lines of the previous depth, a comparison between the experimental and Olaflow forces is shown in Fig. 6.16 for two representative test cases (see Tab. 4.3, test no. 7C and 28C). The difference between experiments and OlaFlow is really small on the magnitude and the related phase shift of the maximum forces in both cases. Some differences appear for the lower negative peaks. The maximum peak of the horizontal force is greater than the vertical one although in the greater wave attack this difference is less evident (Fig. 6.16d). Like in the other different depths, the maximum peak of the horizontal force is back shifted respect the wave crest. The maximum peak of the vertical force is forward shifted similarly to the case where $e/D= 0.5$.
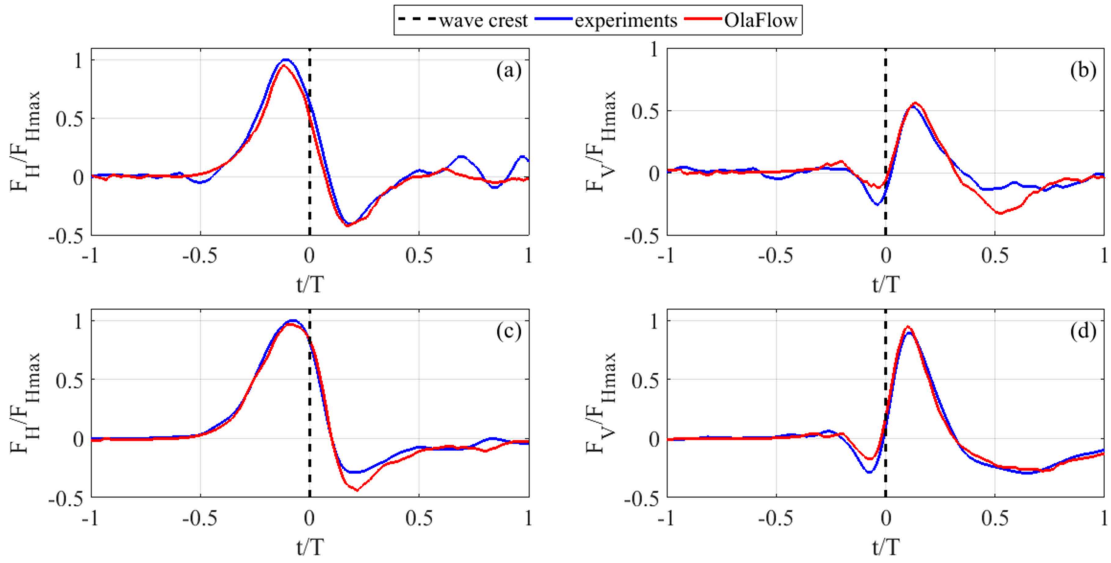
Figure 6.16: *Time variation of experimental and numerical hydrodynamic forces, F_H and F_V ($e/D = 0.25$). (a) Horizontal force (test no. 7C); (b) vertical force (test no. 7C); (c) horizontal force (test no. 28C); (d) vertical force (test no. 28C).*

The comparison for the whole dataset of $e/D = 0.25$ in terms of positive and negative maximum horizontal force, $F_{Hmax,p}$ and $F_{Hmax,n}$, and vertical ones, $F_{Vmax,p}$ and $F_{Vmax,n}$, as a function of A/d are respectively shown in Fig. 6.17. The force peaks are normalized with respect to the maximum peak of the horizontal force, $F_{Hmax}*$ (Fig. 6.17a) and the maximum peak of the vertical force, $F_{Vmax}*$ (Fig. 6.17b). In the overall good agreement between the laboratory tests and OlaFlow, it is possible to observe slightly higher experimental values of $F_{Hmax,p}$ if compared to the corresponding numerical ones and higher numerical values of $F_{Hmax,n}$ compared to the corresponding experimental ones. Concerning the vertical peaks, the differences between experiments and simulations are less evident if compared to the horizontal ones. The positive and negative peaks in both directions increase proportionally to A/d with a greater variation for higher wave amplitudes. The value of $F_{Hmax,p}$ shows a general increase of 63% and $F_{Hmax,n}$ of 62%, while $F_{Vmax,p}$ and $F_{Vmax,n}$ also growth of about 77% and 73%. The weight of the $F_{Vmax,p}$ with respect to $F_{Hmax,p}$, like showed in Fig. 6.17c, ranges between 40% and 100%, i.e. $F_{Hmax,p}$ about equal to $F_{Vmax,p}$ for the greater wave attacks.
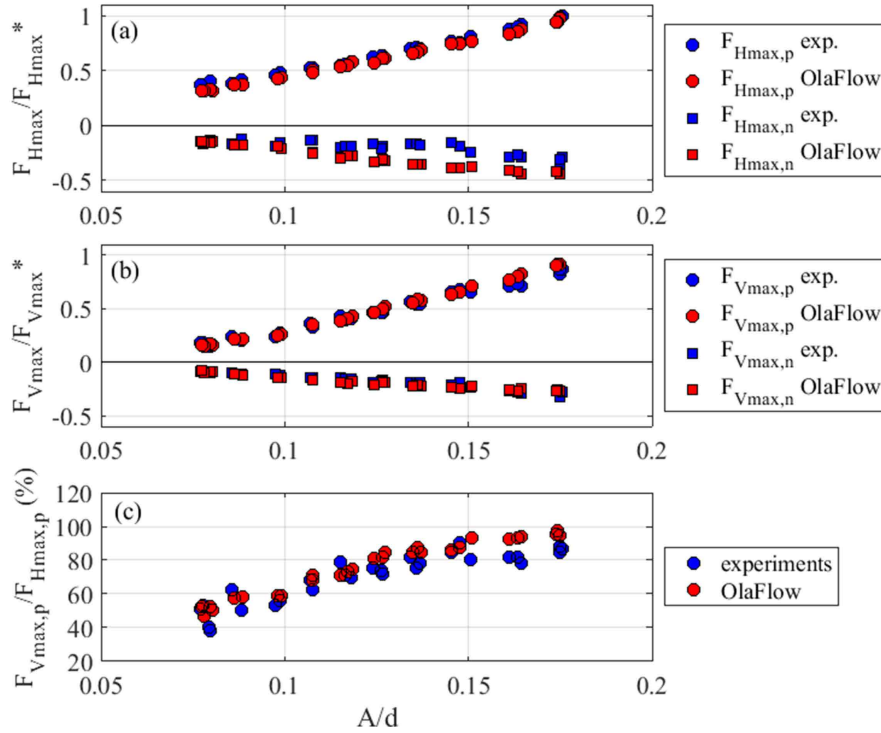
Figure 6.17: *Maximum positive and negative peaks of experimental and OlaFlow hydrodynamic forces vs. A/d (e/D = 0.25). (a) horizontal force; (b) vertical force; (c) weight of vertical force with respect to horizontal one.*

6.3.4 Experimental and OlaFlow forces - e/D = 0.1

The comparisons between the time variation of the hydrodynamic forces acting on the horizontal cylinder from the analyzed laboratory tests and OlaFlow simulations in the case where $e/D = 0.1$ are plotted in Fig. 6.18 for tests 6D and 29D.

The horizontal force changes its magnitude in a similar way to the previous cases and also in this situation the largest positive peak is back shifted with respect to the wave crest. The maximum peak of the vertical force is slightly forward shifted with respect to the solitary wave crest. The agreement between the experimental and numerical values is satisfactory. The positive and negative peaks of the horizontal and vertical forces in the present case are shown respectively in Figs. 6.19a and b. The force peaks are normalized with respect to the maximum peak of the horizontal force, F_{Hmax}*, and the maximum peak of the vertical force, F_{Vmax}*. Also for this gap-to-diameter ratio, the force peaks increase with the increasing of the wave amplitude. In the present range of A/d, the value of $F_{Hmax,p}$ shows an increase of 61% and $F_{Hmax,n}$ of 51%, while $F_{Vmax,p}$ and $F_{Vmax,n}$ also growth of about 71% and 57%, respectively. Fig. 6.17c highlights the weight of the horizontal force in relation to the vertical one. For this specific depth, it is possible to observe that the peaks of the vertical force are greater with respect to the horizontal ones for the higher wave amplitudes ($A/d > 0.125$) while are lower for $A/d < 0.125$.
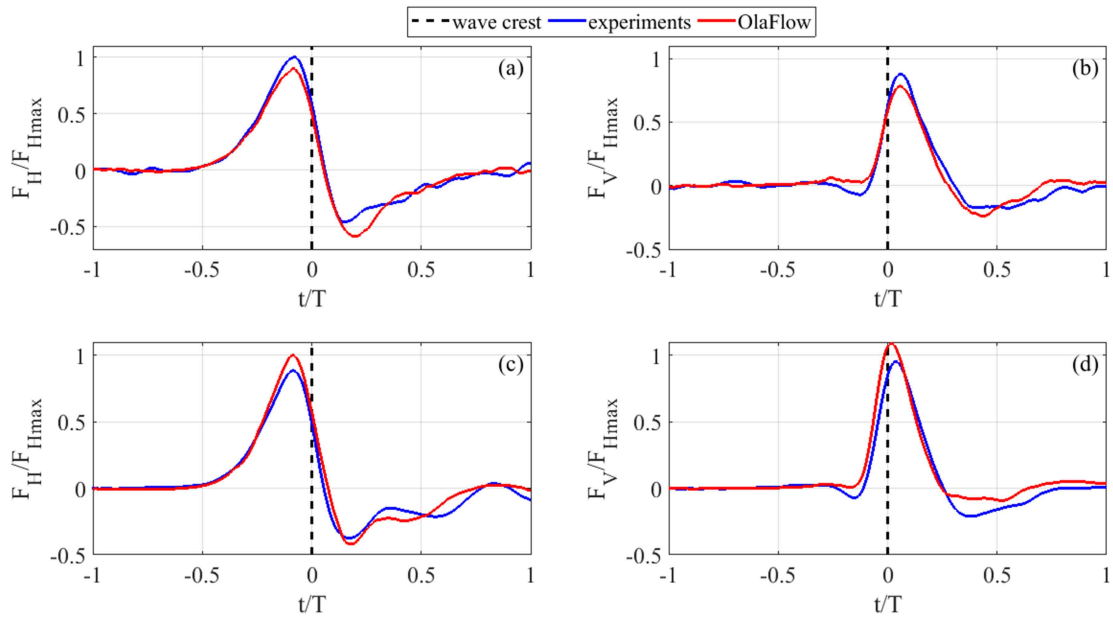
Figure 6.18: *Time variation of experimental and numerical hydrodynamic forces, F_H and F_V (e/D = 0.1). (a) Horizontal force (test no. 6D); (b) vertical force (test no. 6D); (c) horizontal force (test no. 29D); (d) vertical force (test no. 29D).*
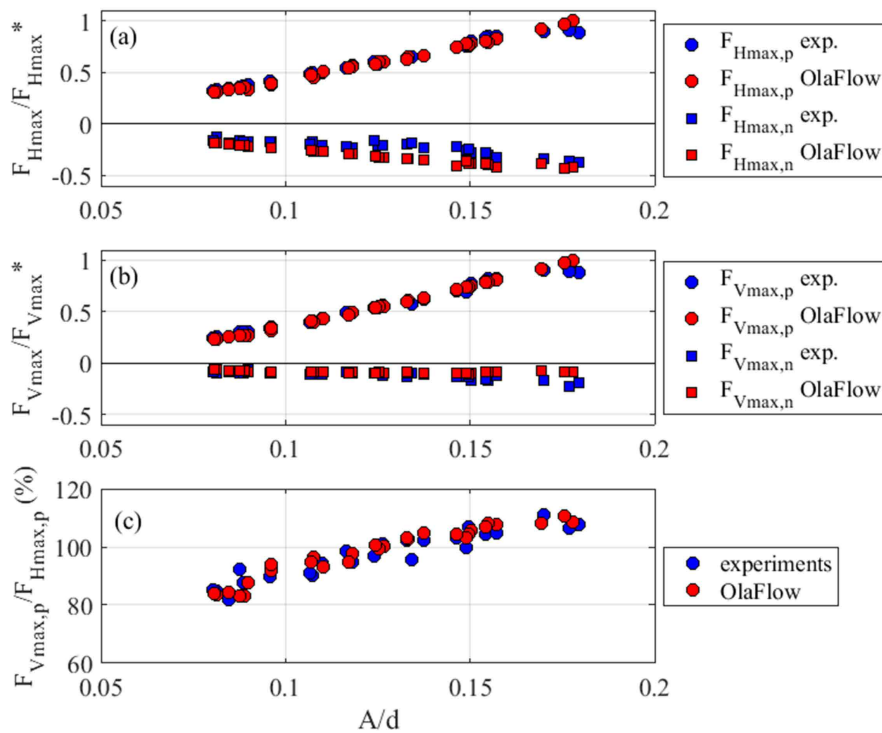

Figure 6.19: *Maximum positive and negative peaks of experimental and OlaFlow hydrodynamic forces vs. A/d (e/D = 0.1). (a) horizontal force; (b) vertical force; (c) weight of vertical force with respect to horizontal one.*

6.3.5 Experimental and OlaFlow forces - e/D = 0

In this section, the time history of the solitary wave loads acting on the bottom-mounted cylinder deduced from the experimental and numerical tests is analyzed. As previously seen for the other depths, two reference test cases characterized by a different wave amplitude and period are considered. Figure 6.20 highlights the experimental and numerical values of the horizontal and vertical hydrodynamic forces induced by solitary waves for tests 5E and 30E, respectively.
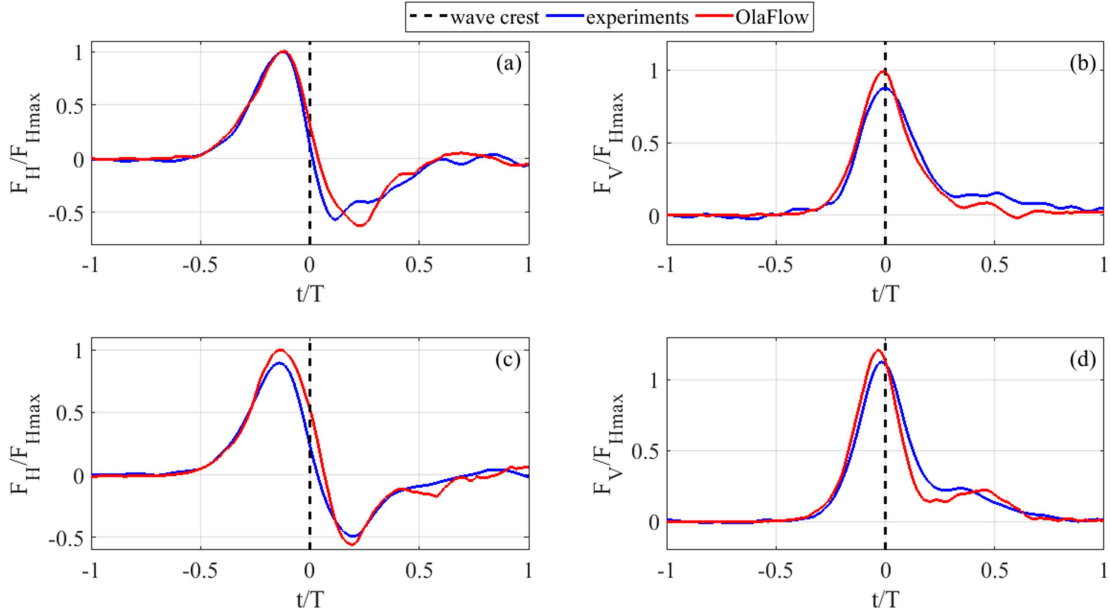

Figure 6.20: *Time variation of experimental and numerical hydrodynamic forces, F_H and F_V ($e/D = 0$). (a) Horizontal force (test no. 5E); (b) vertical force (test no. 5E); (c) horizontal force (test no. 30E); (d) vertical force (test no. 30E).*

It is interesting to observe that, in terms of maximum peaks, F_H is slightly greater than F_V for test number 5E (lower solitary wave), while $F_V > F_H$ for test number 30E (higher solitary wave). Moreover, a prevalence of positive values of the forces can be noticed, revealing that the cylinder is substantially subjected to the coupled action of a forward motion in the direction of solitary wave propagation and a lift one towards the free surface. The above findings are substantially in agreement with experimental observations related to the interaction between regular or random waves and cylinders placed on the bed when the parameter KC is considered (e.g., [49, 55]). It can be observed that the shapes of F_H generally follow those related to a_H, with a less relevant contribution of the drag force related to the decreasing of the negative peak of F_H and the forward shift of the positive peak of F_H. Apart a small contribution of the vertical inertia component for low values of F_V, the shape of the vertical load, for the reference tests no. 5E and 30E, follows that related to the horizontal velocity where the peak appears very close to the solitary wave crest. This situation arises when an external flow interacts with a bottom-mounted cylinder in which the lift component dominates the features of F_V (e.g., [7, 14]). The occurrence of drag and lift forces will be better highlighted when Morison and transverse semi-empirical schemes are applied.

However, it is important to notice that these contribution are linked to the formation of vortex patterns around the cylinder and the consequent deviation from a pure inertial field instead characterized by a potential flow (e.g., [25, 43]).

Taking into account all experimental tests, the positive and negative maximum horizontal forces ($F_{Hmax,p}$ and $F_{Hmax,n}$) and the positive maximum vertical forces (F_{Vmax}) as a function of A/d are respectively shown in Fig. 6.21. Note that these peaks are respectively normalized with respect to the maximum peak of the horizontal force, $F_{Hmax}*$, and the maximum peak of the vertical force, $F_{Vmax}*$. In general, the positive peaks increase almost linearly with A/d, while the negative ones highlight a higher variation for $A/d > 0.15$. The values of $F_{Hmax,n}$ are lower than the positive ones and those referring to F_{Vmax}. It is interesting to note that, for $A/d < 0.105$, $F_{Hmax,p}$ values are slightly greater than F_{Vmax}, while F_{Vmax} values are greater than $F_{Hmax,p}$ values for $A/d > 0.105$ and, particularly, for high A/d (Fig. 6.21c).
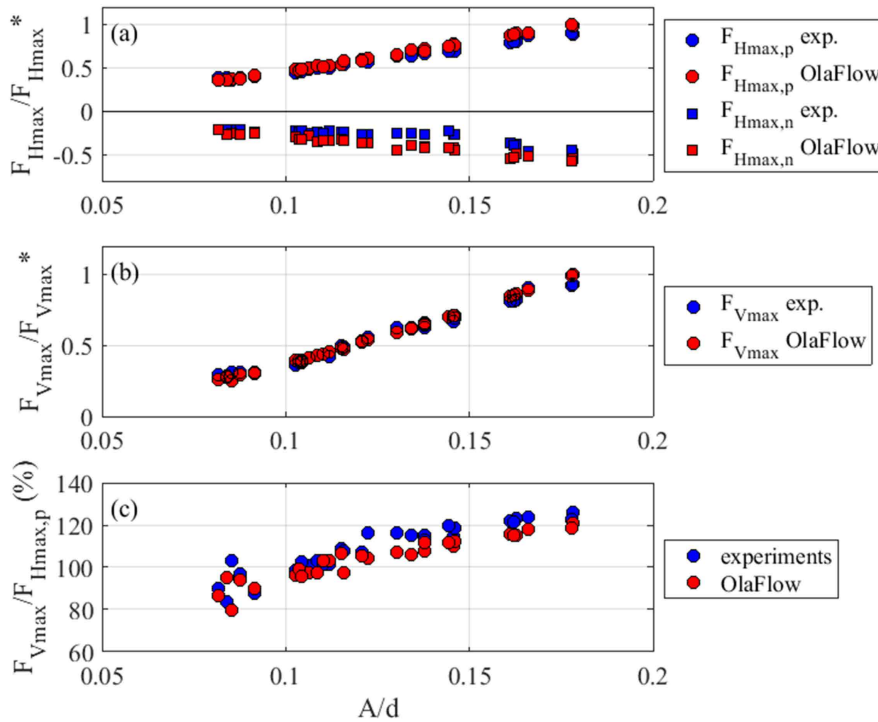

Figure 6.21: *Maximum positive and negative peaks of experimental and OlaFlow hydrodynamic forces vs. A/d (e/D = 0). (a) horizontal force; (b) vertical force; (c) weight of vertical force with respect to horizontal one.*

6.4 Morison and transverse hydrodynamic coefficients

For practical applications, the calibration of semi-empirical formulas to evaluate wave forces consists in the assessment of the hydrodynamic coefficients which represent time-constant parameters representative of the flow field around the cylinder. In order to minimize the differences between experimental and numerical forces and those calculated by Morison and transverse schemes within the adopted wave period, various methods for evaluating the hydrodynamic coefficients have been analyzed. On the basis of the undisturbed kinematics (horizontal velocity, and horizontal and vertical ac-

celeration) at the cylinder center and the hydrodynamic loads at the cylinder deduced by laboratory tests and numerical simulations, in-line C_D and C_{MH}, and transverse, C_L and C_{MV}, hydrodynamic coefficients have been calculated using the ordinary and weighted least square method (e.g., [79]). In the weighted least square method, the difference between the measured/simulated and the semi-empirical force is multiplied by F_H^k, with k a positive index. The resulting hydrodynamic coefficients C_D and C_{MH} are calculated as:

$$
\begin{cases}
C_D = \dfrac{\sum_{i=1}^{M} F_H^{2k+1} u|u| \sum_{i=1}^{M} F_H^{2k} a_H^2 - \sum_{i=1}^{M} F_H^{2k+1} a_H \sum_{i=1}^{M} F_H^{2k} u|u| a_H}{K_D \left[\sum_{i=1}^{M} F_H^{2k} u^4 \sum_{i=1}^{M} F_H^{2k} a_H - \left(\sum_{i=1}^{M} F_H^{2k} u|u| a_H \right)^2 \right]} \\[4mm]
C_{MH} = \dfrac{\sum_{i=1}^{M} F_H^{2k+1} a_H \sum_{i=1}^{M} F_H^{2k} u^4 - \sum_{i=1}^{M} F_H^{2k+1} u|u| \sum_{i=1}^{M} F_H^{2k} u|u| a_H}{K_{MH} \left[\sum_{i=1}^{M} F_H^{2k} a_H^2 \sum_{i=1}^{M} F_H^{2k} u^4 - \left(\sum_{i=1}^{M} F_H^{2k} u|u| a_H \right)^2 \right]}
\end{cases}
\tag{6.3}
$$

where $K_D = \frac{1}{2}\rho D$ and $K_M = \frac{1}{4}\pi D^2 \rho$.

Similarly, the expressions to determine the hydrodynamic coefficients C_L and C_{MV} for the transverse formula read as:

$$
\begin{cases}
C_L = \dfrac{\sum_{i=1}^{M} F_V^{2k+1} u^2 \sum_{i=1}^{M} F_V^{2k} a_V^2 - \sum_{i=1}^{M} F_V^{2k+1} a_V \sum_{i=1}^{M} F_V^{2k} u^2 a_V}{K_L \left[\sum_{i=1}^{M} F_V^{2k} u^4 \sum_{i=1}^{M} F_V^{2k} a_V - \left(\sum_{i=1}^{M} F_V^{2k} u^2 a_V \right)^2 \right]} \\[4mm]
C_{MV} = \dfrac{\sum_{i=1}^{M} F_V^{2k+1} a_V \sum_{i=1}^{M} F_V^{2k} u^4 - \sum_{i=1}^{M} F_V^{2k+1} u^2 \sum_{i=1}^{M} F_V^{2k} u^2 a_V}{K_{MV} \left[\sum_{i=1}^{M} F_V^{2k} a_V^2 \sum_{i=1}^{M} F_V^{2k} u^4 - \left(\sum_{i=1}^{M} F_V^{2k} u^2 a_V \right)^2 \right]}
\end{cases}
\tag{6.4}
$$

where $K_L = K_D$ and $K_{MV} = K_{MH}$. Equations 6.3 and 6.4 recover the ordinary least square approach by setting $k = 0$.

The performances of the time domain methods for calculating in-line and transverse coefficients are checked by the Mean Square Error Percent (MSEP) obtained from the comparison between the semi-empirical Morison and transverse forces with the reference experimental and numerical ones as follows:

$$
MSEP = \frac{1}{N} \sum_{i=1}^{N} \left(\frac{F_i^r - F_i^s}{F_i^r} \right)^2
\tag{6.5}
$$

where F^s represents the generic semi-empirical force and F^r is the generic experimental or numerical force, while N is the number of force values within the wave period of the solitary wave. For engineering purposes, attention is paid to the maximum peak of the wave forces and the related phase shifts, $\phi = 2\pi t_{max}/T$, where t_{max} represents the occurrence time of the maximum peak. Figs. 6.22, 6.23, 6.24, 6.25 and 6.26 show, for any depth, the mean values of MSEP for all the experimental and numerical tests calculated by the ordinary least square (OLS) and the weighted least square using $k = 1$ (WLS1), $k = 2$ (WLS2), $k = 3$ (WLS3) and $k = 4$ (WLS4). In particular, the MSEP is calculated considering the positive and negative maximum peaks of the horizontal force and the negative (for $e/D = 1$) or positive (for the other cases) maximum peaks of the vertical force.
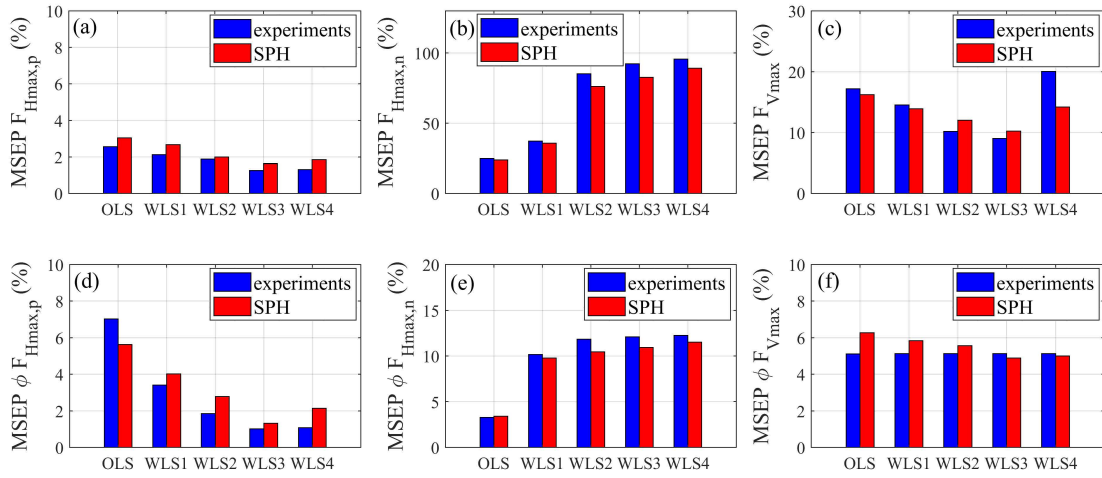
Figure 6.22: *Experimental and numerical Mean Square Error Percent (MSEP) through OLS, WLS1, WLS2, WLS3 and WLS4 methods (e/D = 1). (a) Maximum positive horizontal force, $F_{Hmax,p}$; (b) Maximum negative horizontal force, $F_{Hmax,n}$; (c) Maximum vertical force, F_{Vmax}; (d) Phase shift, ϕ, associated with $F_{Hmax,p}$; (e) Phase shift, ϕ, associated with $F_{Hmax,n}$; (f) Phase shift, ϕ, associated with F_{Vmax}. OLS: ordinary least square; WLS: weighted least square.*
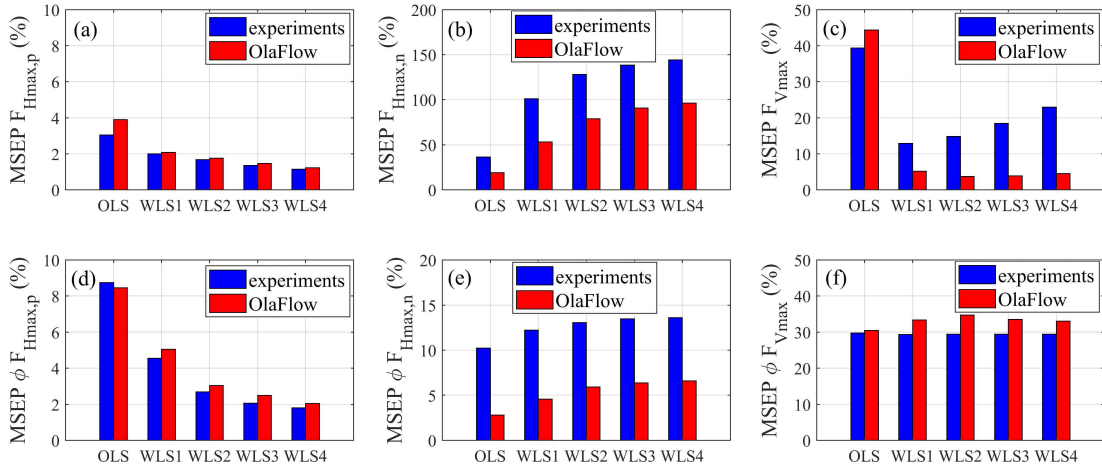

Figure 6.23: *Experimental and numerical Mean Square Error Percent (MSEP) through OLS, WLS1, WLS2, WLS3 and WLS4 methods (e/D = 0.5). (a) Maximum positive horizontal force, $F_{Hmax,p}$; (b) Maximum negative horizontal force, $F_{Hmax,n}$; (c) Maximum vertical force, F_{Vmax}; (d) Phase shift, ϕ, associated with $F_{Hmax,p}$; (e) Phase shift, ϕ, associated with $F_{Hmax,n}$; (f) Phase shift, ϕ, associated with F_{Vmax}. OLS: ordinary least square; WLS: weighted least square.*
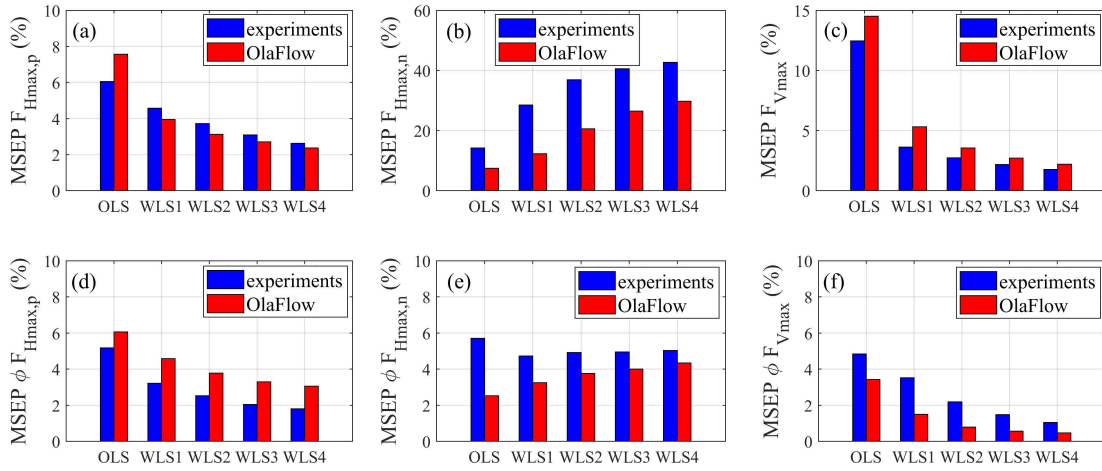
Figure 6.24: *Experimental and numerical Mean Square Error Percent (MSEP) through OLS, WLS1, WLS2, WLS3 and WLS4 methods (e/D = 0.25). (a) Maximum positive horizontal force, $F_{Hmax,p}$; (b) Maximum negative horizontal force, $F_{Hmax,n}$; (c) Maximum vertical force, F_{Vmax}; (d) Phase shift, ϕ, associated with $F_{Hmax,p}$; (e) Phase shift, ϕ, associated with $F_{Hmax,n}$; (f) Phase shift, ϕ, associated with F_{Vmax}. OLS: ordinary least square; WLS: weighted least square.*

Figure 6.25: *Experimental and numerical Mean Square Error Percent (MSEP) through OLS, WLS1, WLS2, WLS3 and WLS4 methods (e/D = 0.1). (a) Maximum positive horizontal force, $F_{Hmax,p}$; (b) Maximum negative horizontal force, $F_{Hmax,n}$; (c) Maximum vertical force, F_{Vmax}; (d) Phase shift, ϕ, associated with $F_{Hmax,p}$; (e) Phase shift, ϕ, associated with $F_{Hmax,n}$; (f) Phase shift, ϕ, associated with F_{Vmax}. OLS: ordinary least square; WLS: weighted least square.*
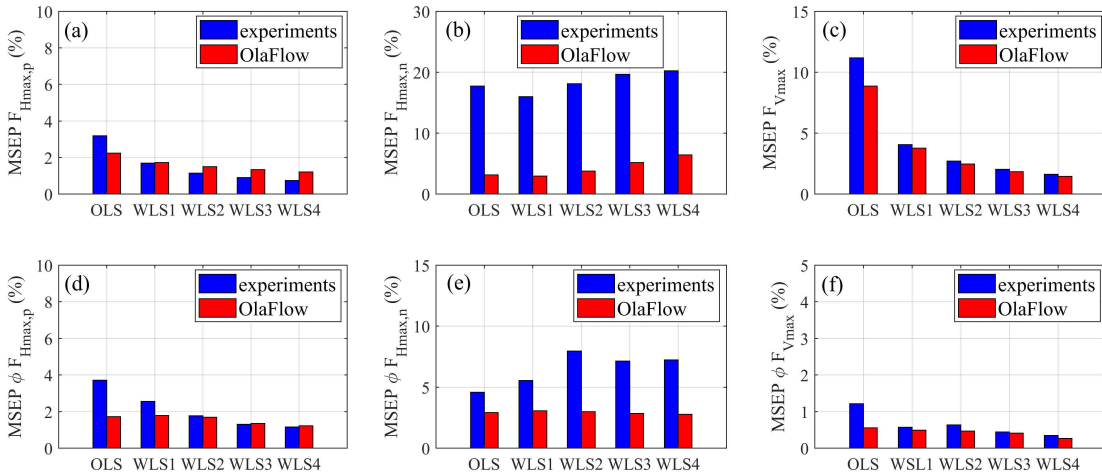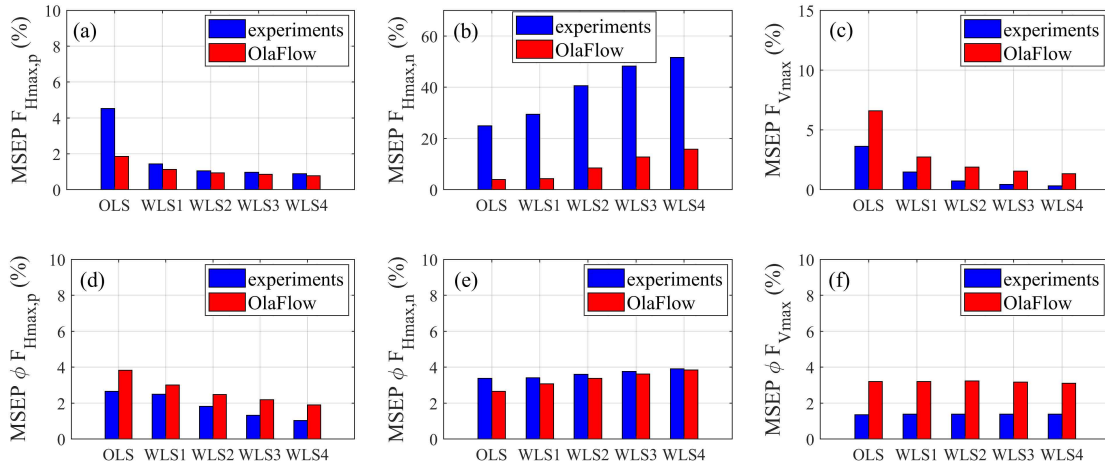
Figure 6.26: *Experimental and numerical Mean Square Error Percent (MSEP) through OLS, WLS1, WLS2, WLS3 and WLS4 methods (e/D = 0). (a) Maximum positive horizontal force, $F_{Hmax,p}$; (b) Maximum negative horizontal force, $F_{Hmax,n}$; (c) Maximum vertical force, F_{Vmax}; (d) Phase shift, ϕ, associated with $F_{Hmax,p}$; (e) Phase shift, ϕ, associated with $F_{Hmax,n}$; (f) Phase shift, ϕ, associated with F_{Vmax}. OLS: ordinary least square; WLS: weighted least square.*

Taking into account for all the methods calibrated both experimentally and numerically, in the case of $e/D = 1$, the mean MSEP of maximum horizontal peaks is of the order of 2% while that related to the maximum vertical peaks is less than approximately 15%. The mean MSEP linked to the time shifts of the horizontal and vertical loads are respectively lower than 4% and 7%. On the other hand, the mean MSEP of horizontal negative peaks and the related MSEP of the time shifts are greater, especially for the value of $k > 1$. Specifically, Fig. 6.22b shows that the MSEP of $F_{Hmax,n}$ can reach about 90% while the MSEP of the phase shift of $F_{Hmax,n}$ about 10% (Fig. 6.22e). Observing the histograms related to the case of $e/D = 0.5$ (Fig. 6.23), the mean MSEP of the vertical force results slightly higher with respect to the previous case. The mean MSEP of $F_{Hmax,p}$ and F_{Vmax} is respectively about 2% and 17% while that related to phase time shift are respectively 4% and 31%. The mean error of the maximum negative horizontal force is equal to 84% considering both experimental and numerical data. Fig. 6.24 represents the MSEP of the dataset related to case of $e/D = 0.25$. Here again, the mean MSEP of positive horizontal peak is low (4%) and the vertical peak is more than approximately 5%. The mean MSEP linked to the time shifts of the horizontal and vertical loads is lower than 5%. The MSEP of $F_{Hmax,n}$ ($e/D = 0.25$) results lower with respect to the previous cases, in particular in the ordinary least square method and the weighted least square method using $k = 1$, i.e. 11% and 20%, respectively. Similarly, Fig. 6.25 shows, for $e/D = 0.1$, a low value of the mean MSEP of horizontal negative peaks (about 5%) for the methods calibrated numerically with OlaFlow and less than approximately 20% for the experiments. The mean MSEP of $F_{Hmax,p}$ and F_{Vmax} is respectively about 2% and 4%, while the mean MSEP linked to the time shifts of the horizontal and vertical loads is respectively lower than 2% and 1%. In the last case (cylinder at the bottom, i.e. $e/D = 0$), the mean MSEP of $F_{Hmax,p}$ and F_{Vmax} is about 2%, while the mean MSEP linked to the time shifts of the horizontal and vertical loads is lower than 3%. The maximum MSEP, like in the other depths, is related to the $F_{Hmax,n}$ and reaches values of 40% in the methods calibrated experimentally and

about 10% for the numerical ones. Comparing the above methods for all the involved depths of the horizontal cylinder, WLS1 provides the lowest values of MSEP among all involved approaches and, therefore the related hydrodynamic coefficients are adopted in the Morison and transverse formulas. The mean MSEP of the maximum peak of the horizontal and vertical force is about 2%, while the mean MSEP calculated with the OLS method reaches higher values (10%). Conversely, the mean MSEP of the $F_{Hmax,n}$ tends to grow as k increases. The weighted least square method with $k = 1$ represents the best compromise and moreover allows a better estimate on the time variation of the vertical force, as shown in the next section 6.5.

As mentioned in chapter 3, for the case of $e/D = 0.25$ and $e/D = 0.1$ the lift component did not model the forward phase shift in the observed experimental and numerical time series of the vertical loads. This is due to the fact that the canonical lift force (see Eq. 3.7) is proportional to the horizontal velocity and then to the maximum surface elevation of the solitary wave at the vertical section of the cylinder. The Eqs. 3.16 and 3.17 show respectively the new lift force formulation and the time interval between the occurrence of the wave crest and that related to the peak of the observed lift force. The lift hydrodynamic coefficient, C_L, was then calculated considering this new formulation. The relationship between the time shift, t_s, and the different physical quantities of the experimental and numerical tests is shown in Figs. 6.27 and 6.28 for $e/D = 0.25$ and $e/D = 0.1$, respectively. The resulting fitting curve shows a good agreement between experimental and OlaFlow simulations and particularly for $e/D = 0.25$, leading that a very small time shift occurs for the adopted two approaches. For $e/D = 0.25$, the value of the phase angle, ϕ, is given by a power law as follows:

$$\phi = a_1 \left(\frac{d}{A}\right)^{b1} \tag{6.6}$$

where a_1 and b_1 are two empirical constant. Considering the numerical values, $a_1 = 0.166$ and $b_1 = 0.613$ with a correlation coefficient $R^2 = 0.976$.
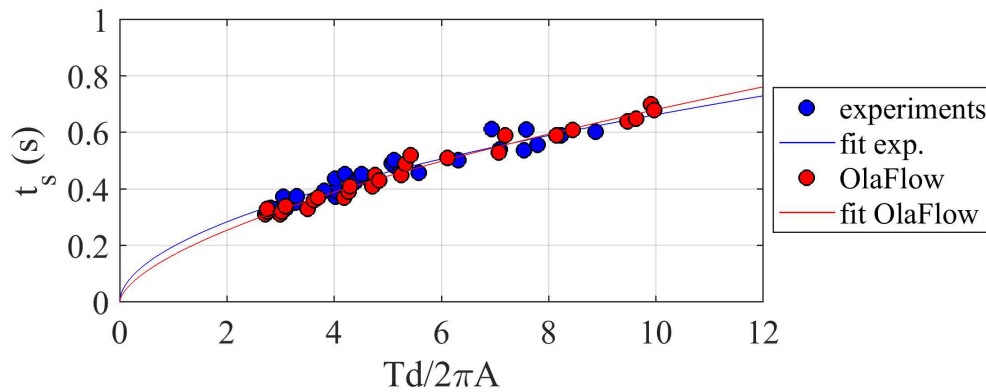

Figure 6.27: *Experimental and numerical values of the time shift t_s vs. $Td/2A\pi$ (e/D = 0.25).*

For $e/D = 0.1$, the phase angle varies linearly with respect to A and d as follows:

$$\phi = a_2 \frac{d}{A} \tag{6.7}$$

where a_2, the empirical constant, assumed the value of 0.025 for the OlaFlow dataset with a correlation coefficient $R^2 = 0.933$.
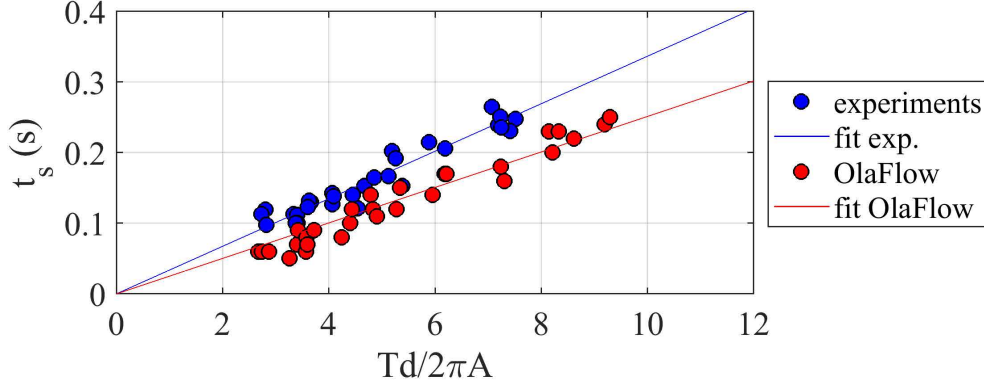

Figure 6.28: *Experimental and numerical values of the time shift t_s vs. $Td/2A\pi$ (e/D = 0.1).*

After the validation of the numerical hydrodynamic coefficients with the experimental ones, supplementary numerical simulations were performed to extend the range of A/d. In the first case ($e/D = 1$), the dataset was expanded through six numerical tests with higher A/d (0.2, 0.21, 0.22, 0.23, 0.24 and 0.25) and three with lower A/d (0.05, 0.06 and 0.07). Other two SPH tests were conducted to better cover the initial experimental range and corresponding to A/d = 0.085 and 0.165, for a total number of 27 numerical tests performed. In the additional simulations, it was noticed that the flow regime is still characterized by a couple of vortices behind the cylinder (as those in Figs. 6.11 and 6.12), with a lower vorticity associated to smaller values of A/d that suggests that drag and lift forces still persist. Similarly, also for the other four depths, additional numerical simulations were performed with OlaFlow to enlarge the calculation range of the hydrodynamic coefficients. The new simulations, in the case of $e/D =$ 0.5, present the follow values of A/d: 0.072, 0.077, 0.186, 0.199, 0.212, 0.223, 0.235 and 0.245. The third analyzed depth ($e/D = 0.25$) was enlarged through the following values of the A/d: 0.062, 0.072, 0.186, 0.199, 0.212, 0.223 and 0.245. The additional numerical tests, in the case of $e/D = 0.1$ present the following values of A/d: 0.056, 0.066, 0.077, 0.186, 0.198, 0.211, 0.223, 0.235 and 0.245. The last dataset, related to the case in which the cylinder is placed on the bottom ($e/D = 0$), was expanded through the following values of A/d: 0.061, 0.071, 0.205, 0.217, 0.227 and 0.248. Considering all the five depths, 176 numerical simulations were performed. The upper limit of the simulations is fixed at $A/d = 0.25$ because of the limitation of the relationship adopted to determine the free stream kinematic field at the transversal axis of the cylinder (see Eq. 2.6). For $A/d > 0.25$, the application of Eq. 2.6 leads to unphysical singularities in the shape of the velocities and accelerations which influence the correct assessment of the hydrodynamic forces using the Morison and transverse semi-empirical schemes and makes it impossible a comparison with the numerical data. Values of $A/d < 0.05$ were not considered since the solitary waves have low amplitudes and very long waves (i.e. L greater than 15 m) leading to the use of a very extended channel with a raising of the computational effort to run the numerical simulations. However, the actual range of A/d proves to be comparable with other literature investigations dealing with the interaction between solitary waves and marine structures (e.g., [45], [39], [26]).

On the basis of the results obtained by the numerical simulations and the experimental investigation, Figs. 6.29, 6.30, 6.31, 6.32 and 6.33 show respectively the experimental and numerical values of C_D, C_{MH}, C_L and C_{MV} in the Morison and transverse semi-empirical equations as a function of A/d ranging from approximately 0.05 to 0.25.
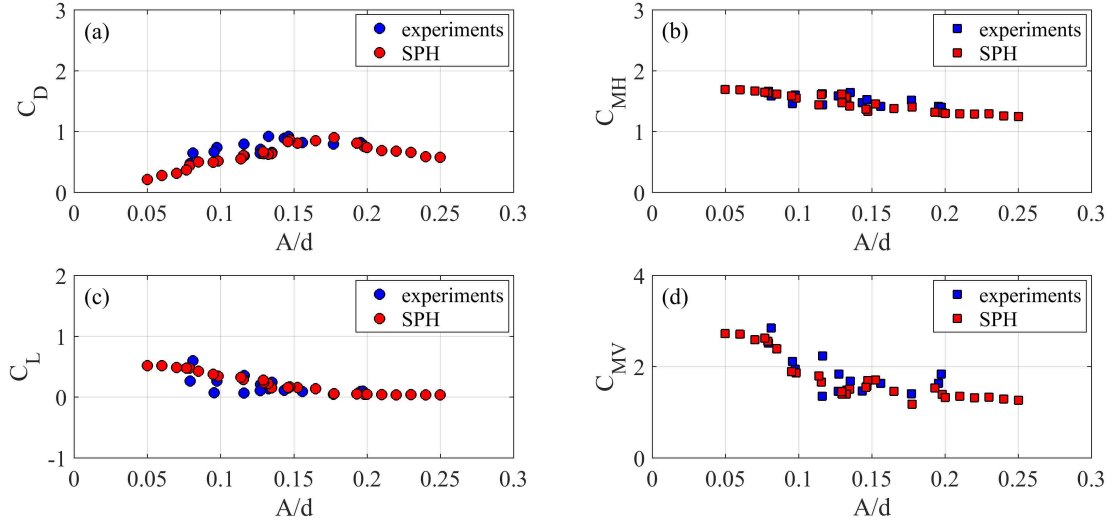

Figure 6.29: *Experimental and numerical hydrodynamic coefficients vs. A/d (e/D = 1). (a) C_D; (b) C_{MH}; (c) C_L; (d) C_{MV}.*

The horizontal and vertical inertia and the lift coefficients in the case of $e/D = 1$ (6.29) highlight a general decreasing trend when A/d increases, while the drag coefficient tends to increase up to approximately $A/d = 0.17$ with a corresponding $C_D = 0.9$, followed by a progressive reduction. The values of C_L range between about 0.01 and 0.6. As previously observed, the inertia components dominate the total forces in the horizontal and vertical direction for the present range of A/d. When A/d increases, the ratio between horizontal inertia and drag coefficients, C_{MH}/C_D oscillates from 2 to 6, while the ratio between vertical inertia and lift coefficients, C_{MV}/C_L, ranges between about 5 and 30, revealing that the lift force component is generally weak when the cylinder is placed quite far from the bottom as in the present case. Maximum C_{MH} and C_{MV} reach values respectively of up to 1.7 and 2.8 for low A/d and minimum C_{MH} and C_{MV} tend both to be approximately to 1.2 for high A/d. More stable values of C_{MH} and C_{MV} are observed for low A/d presuming that an asymptotic behavior of the inertia coefficients should be reached. When $A/d \rightarrow 0$, the resulting fully inertial field leads to a negligible contribution of drag and lift forces (e.g., [16] [69]). This feature of the hydrodynamic coefficients can also be viewed in terms of KC in which the trend of the coefficients is substantially the same of that represented using A/d apart a larger scattering due to dependency on the apparent wave period. The parameter KC ranges from 3.3 to 9.4 considering all numerical tests, confirming that the inertia components play the major role in assessing the total loads. This feature was widely noticed in various experimental activities in the case of horizontal cylinders subjected to regular or irregular waves where KC is taken as the representative parameter for wave-cylinder interaction problems (e.g., [62]). In particular, the increasing and

the successive decreasing of C_D was noticed for regular and irregular waves by Justesen [40] and Longoria et al. [44] with the maximum C_D occurring at about $KC = 10$ which is slightly higher that the current analysis ($KC = 8.5$). The change in the trend of C_D can be deduced from the SPH simulations represented in Figs. 6.11 and 6.12. In the former case ($KC = 4.82$) characteristic of the increasing trend of C_D, the greater vortex appearing behind the cylinder after the passage of the solitary wave crest tend progressively to move with a predominant transverse direction. In the latter case ($KC = 7.81$) representative of the initial decreasing trend of C_D, the vortices seem to show a resulting movement in the direction of the flow motion. Although the passage of a unique solitary wave at the cylinder is investigated here, the above results show some similarities with the experimental evidences for regular waves by Sumer and Fredsoe [69] regarding the occurrence of a transverse vortex street and a successive convection of the vortices away from the cylinder when KC increases. The lowest value of $KC = 3.3$ is very close to the critical threshold for regular waves fixed at 2.2 [62] and related to the transition from the potential flow regime to the vortex shedding one. The decreasing trend of C_{MH} and C_{MV} is comparable with that observed in the considered KC range by several authors in the case of oscillatory flows (e.g., [16]). In the case of a horizontal cylinder subjected to regular waves for $e/D = 1$ and comparable with the present $e/D = 1.075$, experimental asymptotic values occurring for a potential flow characterized by only inertia loads are $C_{MH} = 2.1$ [62] and $C_{MV} = 2.2$ [16]. The above values are then slightly different than the mentioned present values for $A/d = 0.05$. The trend and magnitude of C_L is similar of that experimentally observed by Sumer et al. [70] at $e/D = 1$.

Fig. 6.30 shows the comparison between the experimental and numerical values of the hydrodynamic coefficients for $e/D = 0.5$. The horizontal inertia coefficients highlight an overall decreasing trend when A/d increases, while the drag, lift and the vertical inertia coefficients generally tend to increase. Specifically, C_{MV}, for values of $A/d > 0.2$, undergoes a progressive reduction while C_D, for the lower values of A/d ($A/d < 0.1$) tends to reduce. Observing the values of C_L, the numerical coefficients show higher values if compared to the experimental ones.
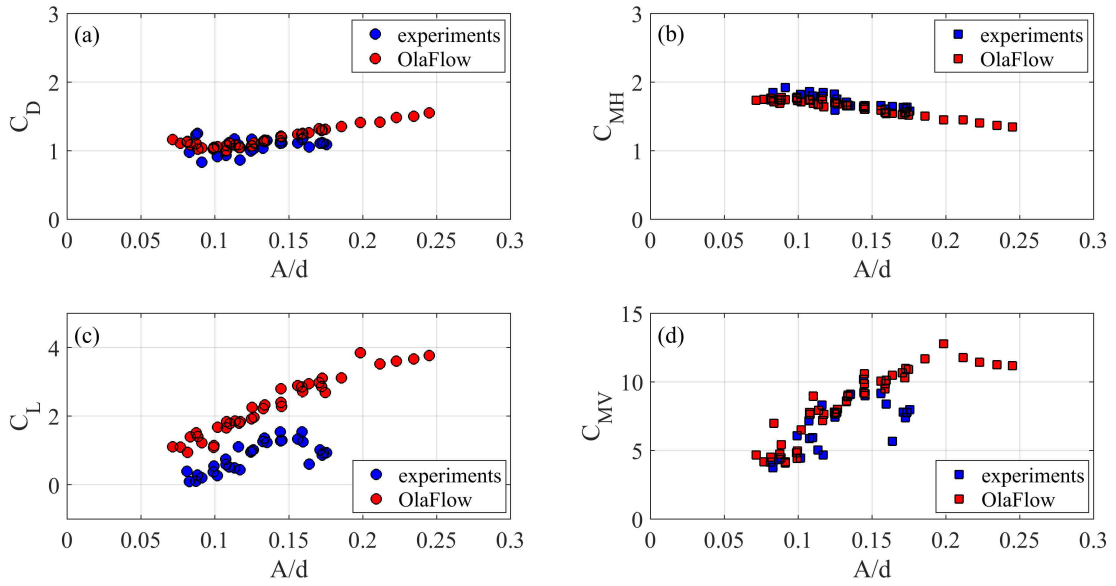
Figure 6.30: *Experimental and numerical hydrodynamic coefficients vs. A/d (e/D = 0.5). (a) C_D; (b) C_{MH}; (c) C_L; (d) C_{MV}.*

The hydrodynamic coefficients calculated for the gap-to-diameter ratio $e/D = 0.25$ are shown in Fig. 6.31. The horizontal inertia coefficients tend to reduce with the increasing of A/d. Although present some differences between experimental and numerical coefficients, the vertical inertia coefficients decrease with the increasing of the wave amplitude. The values of C_D increase with decreasing of A/d, while the lift coefficient tends to increase up to approximately $A/d = 0.16$ with a corresponding value of $C_L = 2$, followed by a progressive reduction.
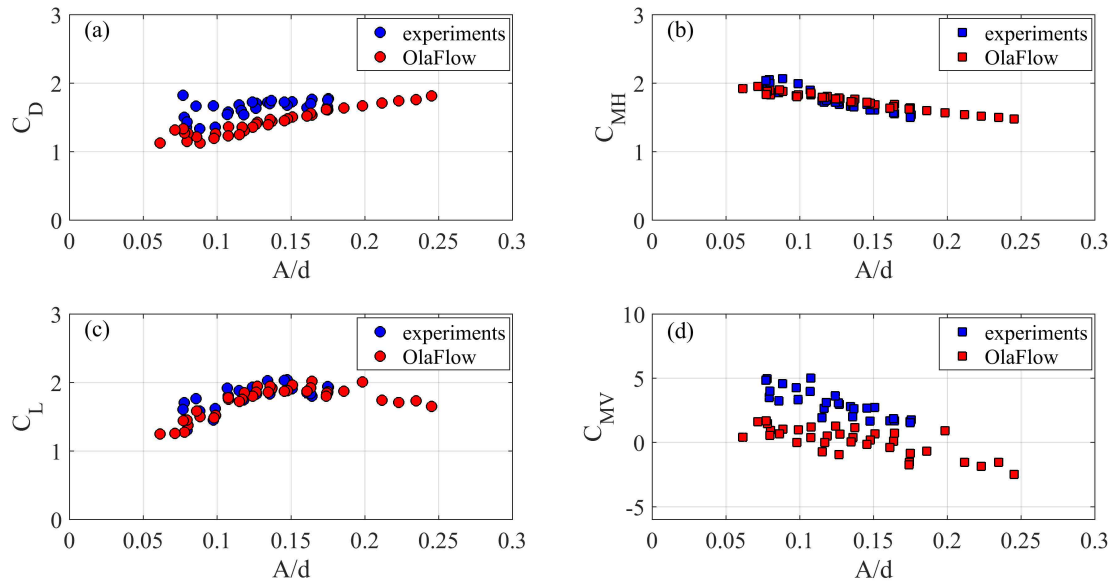

Figure 6.31: *Experimental and numerical hydrodynamic coefficients vs. A/d (e/D = 0.25). (a) C_D; (b) C_{MH}; (c) C_L; (d) C_{MV}.*

Fig. 6.32 illustrates the comparison between the experimental and numerical hydrodynamic coefficients when the gap-to-diameter ratio is equal to 0.1. In this case, it is possible to observe a little discrepancy between the experiments and OlaFlow for the drag coefficient. The numerical values of C_D tend to reduce with the increasing of A/d while the experimental ones seem to increase. However, the difference in term of magnitude is really low. The horizontal inertia coefficients, as well as for the other cases, decrease with the increasing of A/d. For the lower A/d, C_{MH} presents the maximum value, that in this case is equal to 2.5. Regarding the vertical hydrodynamic coefficients, Fig. 6.32c and Fig. 6.32d show an initial increasing of the value of the coefficients and, for $A/d > 0.12$, a subsequent decreasing.
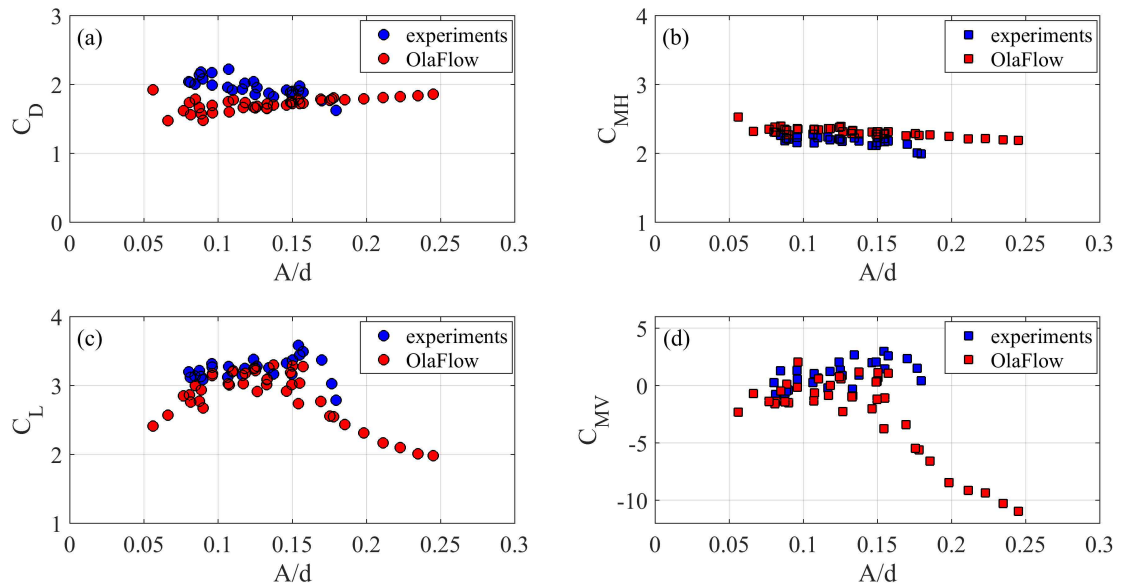

Figure 6.32: *Experimental and numerical hydrodynamic coefficients vs. A/d (e/D = 0.1). (a) C_D; (b) C_{MH}; (c) C_L; (d) C_{MV}.*

The experimental and numerical hydrodynamic coefficients for $e/D = 0$ are plotted in Fig. 6.33. The values of C_{MH} and C_L show a general decreasing trend when A/d increases. It can be observed that the stable trend of horizontal inertia coefficient is particularly evident for the analyzed all the gap-to-diameter ratios. In addition, the mean value of C_{MH} tends to grow with the decreasing of the depth of the cylinder. In this case, considering the numerical coefficients, C_{MH} ranges from 3.1 to 2.4 unlike the first case ($e/D = 1$) where C_{MH} ranges from 1.7 to 1.2. The drag coefficients present a different trend. Indeed, C_D tends to grow when A/d increases. Observing the variation of C_D in the other depths, is possible to note that, on average, the trends are always increasing. The vertical inertia coefficient presents a scattered trend which seems to decrease for low values of A/d, while a increasing trend for higher wave amplitudes can be noticed. However, C_{MV} is the more scattered coefficient with the highest uncertainty, even if the inertia force component has a small weight in calculating the vertical load as compared to the lift load, as successively highlighted in the application of semi-empirical force models (see section 6.5). Regarding C_L, this coefficient shows a general decreasing trend when A/d increases.
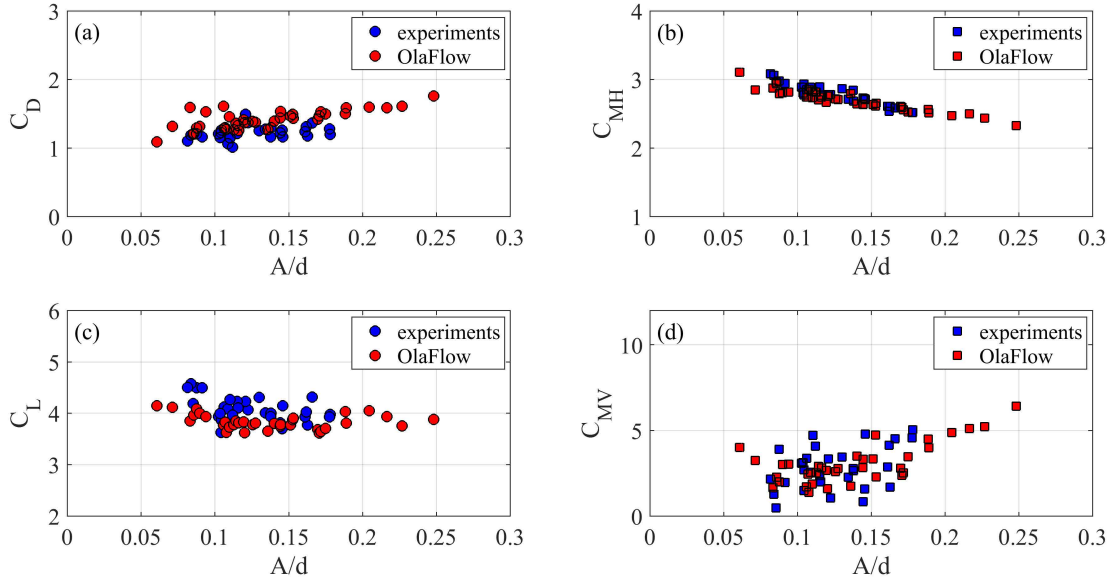
Figure 6.33: *Experimental and numerical hydrodynamic coefficients vs. A/d (e/D = 0). (a) C_D; (b) C_{MH}; (c) C_L; (d) C_{MV}.*

6.5 Application of Morison and transverse equations

The features of Morison and transverse equations calibrated by experimental and numerical hydrodynamic coefficients from the WLS1 method are here displayed in the time domain to show the contribution of the different force components. For the representative test case no. 14A ($e/D = 1$), Figs. 6.34a and 6.34b show respectively the comparisons between the time history of the experimental and numerical horizontal force, F_H, and that calculated by the calibrated Morison scheme from Eq. 3.6 through the corresponding inertia, F_{HI}, and drag, F_D, force components. Figs. 6.34c and 6.34d describe respectively the comparisons between the time history of the experimental vertical force, F_V, and that calculated by the transverse scheme from Eq. 3.7 with the related inertia, F_{VI}, and lift, F_L, force components. Note that in Fig. 6.34 and in the following Figs. 6.36, 6.38, 6.40 and 6.42 the Morison and transverse schemes are respectively represented by the symbols M and T.
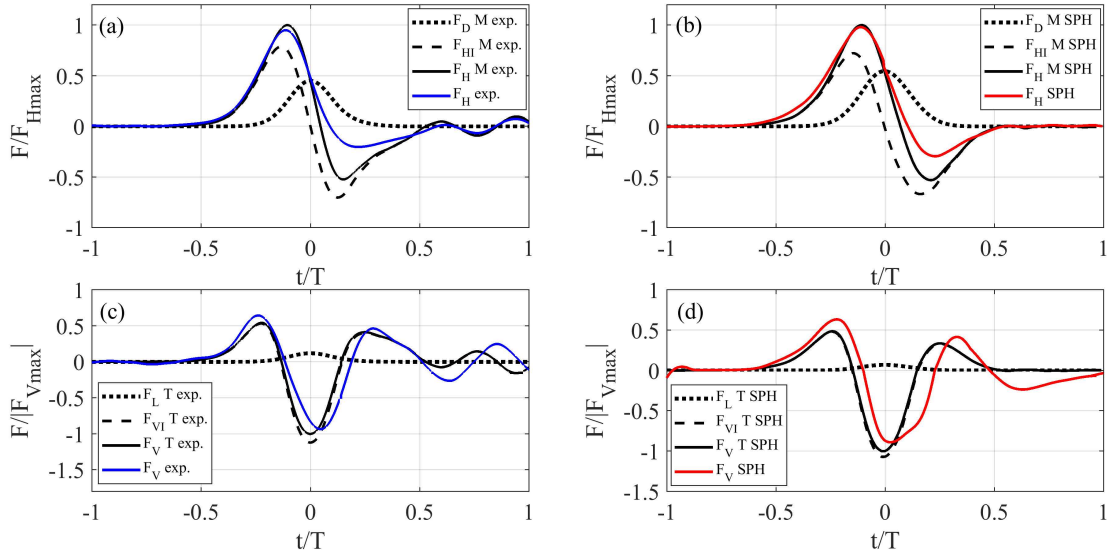
Figure 6.34: *Time variation of hydrodynamic forces calculated by semi-empirical equations, experiments and SPH ($e/D = 1$, test no. 14A). (a) Comparison between experimental F_H and Morison $F_D M$, $F_{HI} M$ and $F_H M$ calibrated by experiments; (b) Comparison between numerical F_H and Morison $F_D M$, $F_{HI} M$ and $F_H M$ calibrated by SPH; (c) Comparison between experimental F_V and transverse $F_L T$, $F_{VI} T$ and $F_V T$ calibrated by experiments; (d) Comparison between numerical F_V, and transverse $F_L T$, $F_{VI} T$ and $F_V T$ calibrated by SPH.*

A general good correspondence between semi-empirical equations vs. experiments and SPH simulations is observed particularly for the maximum peak of the horizontal force modeled by the Morison scheme. A less accurate modeling of the peaks and the phase shift of the vertical force can be seen in the application of the transverse equation. The occurrence of the maximum horizontal and vertical forces is given by the prevalence of the inertia forces depending on the horizontal and vertical acceleration with respect to the drag and lift ones related to the horizontal velocity. The horizontal force positive peak is greater than the negative one and its shape tends to follow the free stream horizontal acceleration at the cylinder. The vertical force shows an additional positive peak due to the shape of the vertical acceleration involved in the expression of the vertical inertia. Moreover, a higher negative peak of vertical force appears quite close to the maximum vertical inertia. As highlighted by the first analysis of MSEP (see Fig. 6.22), a discrepancy in the magnitude of negative peak is noticed by the semi-empirical models in reproducing the horizontal force as well as an overall back shift in the time series of the vertical one.

The values of F_D, F_{HI}, F_L and F_{VI} adopted to determine the total horizontal and vertical loads using the calibrated Morison and transverse formulas through SPH are also analyzed in terms of positive and negative peaks. In order to show the variation of the force components, the above considered 27 SPH simulations deduced from a more extended range of A/d and previously verified by laboratory tests are taken into account. In addition, a more stable trend of the numerical results compared with the laboratory ones has been observed. The considered four force components are weighted with respect to the corresponding maximum peak of the semi-empirical horizontal and vertical force in order to exhibit their specific contribution. This behavior is illustrated in Fig. 6.35 as a function of A/d. It is evident that the peaks of the horizontal and

vertical forces are principally influenced by those related to the inertia components. The greater weight is related to lower A/d which is close to a fully inertia regime generally encountered for low KC (e.g. [62]). Specifically, the weight of the positive peak of horizontal inertia force is always higher that 70% in the studied values of A/d. For low A/d, the mentioned weight proves to be higher than 90%. The progressive deviation from a fully inertia regime can be noticed by analyzing the drag contribution which represents 6% of the horizontal force for lower A/d until 50% of the horizontal force for higher A/d. It is worth noting that the ratio between the peaks of the vertical inertia component and the total vertical one is generally greater than 1 and reaches values of up to 2. This result is driven by the positive contribution of lift force which acts to reduce the maximum negative peak of vertical force compared to the inertia one. The contribution of the lift force conversely shows an overall decreasing when A/d increases, ranging from about 9% to 53% of the resulting vertical force. As shown in Fig. 6.29, the tendencies of the force peaks generally reflect the features of the hydrodynamic coefficients.
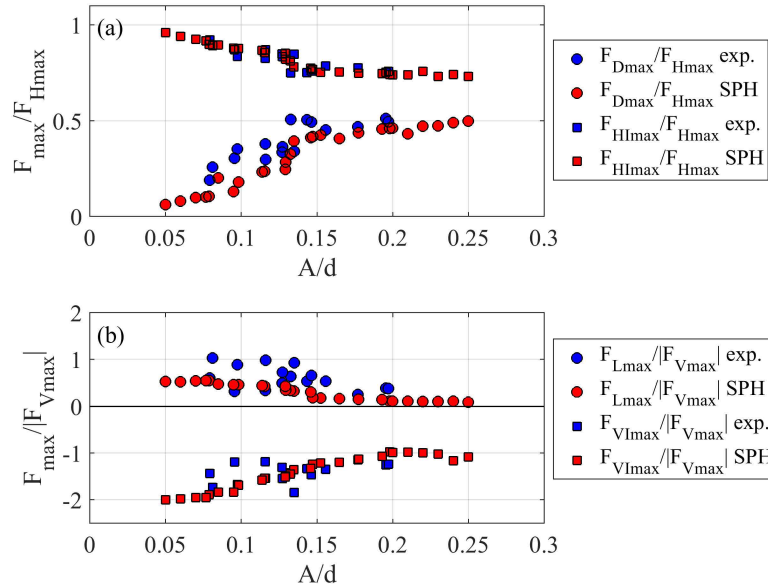

Figure 6.35: *(a) Peaks of Morison force components deduced from experiments and SPH vs. A/d (e/D = 1): drag F_{Dmax} and inertia F_{HImax}; (b) Peaks of transverse force components deduced from experiments and SPH vs. A/d (e/D = 1): lift F_{Lmax} and inertia F_{VImax}.*

For a representative test case (test no. 31B) related to the case of e/D = 0.5, the comparisons between the time history of the experimental and OlaFlow horizontal force and that calculated by the calibrated Morison scheme through the corresponding inertia and drag force components are shown in Figs. 6.36a and 6.36b. Figs. 6.36c and 6.36d describe respectively the comparisons between the time history of the experimental vertical force, and that calculated by the transverse scheme with the related inertia and lift force components. A general good correspondence between semi-empirical equations vs. experiments and OlaFlow simulations is observed particularly for the horizontal force modeled by the Morison scheme. The maximum peak of the horizontal force is well modeled for both cases. In addition, Fig. 6.36b indicates that there is a good correspondence also in the case of the negative maximum peak of the numerical

horizontal force. For this specific gap-to-diameter ratio (e/D = 0.5), the modeling of the vertical force is less accurate. Anyway, the transverse model reproduces well the peak of the vertical force which is the most important target for engineering aims. Fig. 6.36c and Fig. 6.36d indicate that the comparison between experimental F_V and $F_V T$ is satisfactory for the positive and negative peak of the vertical force, while the comparison between the numerical F_V and $F_V T$ is satisfactory only for the positive peak.
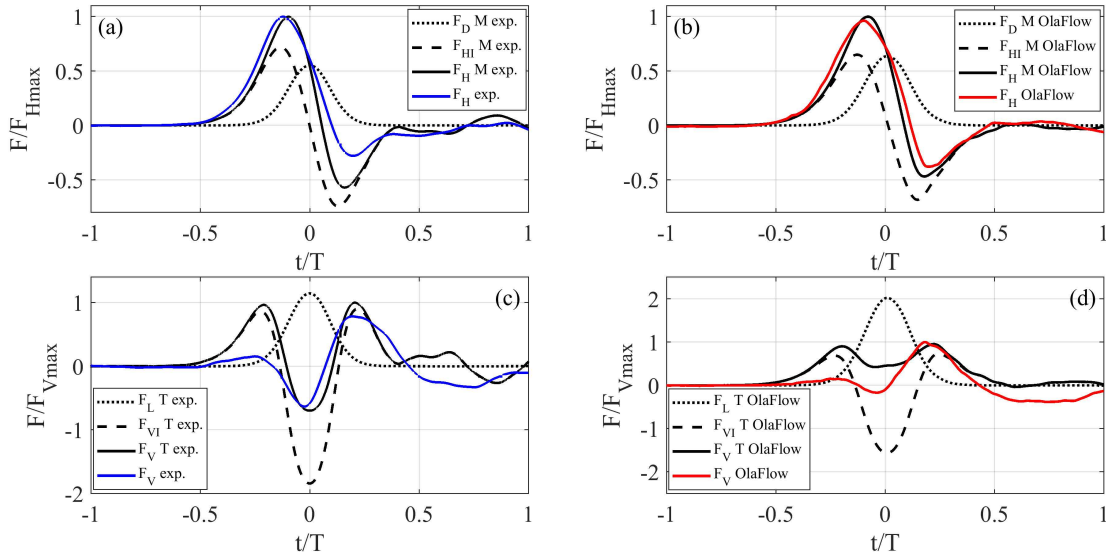

Figure 6.36: *Time variation of hydrodynamic forces calculated by semi-empirical equations, experiments and OlaFlow (e/D = 0.5, test no. 31B). (a) Comparison between experimental F_H and Morison $F_D M$, $F_{HI} M$ and $F_H M$ calibrated by experiments; (b) Comparison between numerical F_H and Morison $F_D M$, $F_{HI} M$ and $F_H M$ calibrated by OlaFlow; (c) Comparison between experimental F_V and transverse $F_L T$, $F_{VI} T$ and $F_V T$ calibrated by experiments; (d) Comparison between numerical F_V, and transverse $F_L T$, $F_{VI} T$ and $F_V T$ calibrated by OlaFlow.*

The 28 experimental tests (see Tab. 4.2) and the 39 OlaFlow simulations were analyzed in order to calculate the variation of the force components. As in the previous case, the four components are weighted with respect to the corresponding maximum peak of the semi-empirical horizontal and vertical force in order to exhibit their specific contribution. Fig. 6.37 illustrates the variation of the force components as a function of A/d. The weight of the peak of the horizontal inertia tends to decrease from about 85% to 52% with the increasing of A/d. Differently, the weight of the peak of the drag force tends to increase from 30% to 80% for the higher values of the wave amplitude. For a value of A/d about equal to 0.18, the two force components of the horizontal force are equal. It is worth noting that in Fig. 6.36a, related to a test case where A/d = 0.175, the weight of the peak of the inertia force is slightly higher with respect to the drag one. Indeed, for A/d > 0.18, the drag force overcomes the inertia one. As regards the vertical force components, Fig. 6.36b reveals that the higher weight is generally due to the lift component. To represent in a correct way the peak of the vertical force, the contribution of the vertical inertia is needed. So, the lift component reaches this highest value to balance the highest value of the vertical inertia at the passage of the solitary wave on the vertical section of the cylinder ($t = 0$). The little discrepancy

in the experimental and vertical C_L and the small difference between the time variation of the experimental and numerical F_V produces some dissimilarities between the experimental and numerical weight of F_{Lmax}.
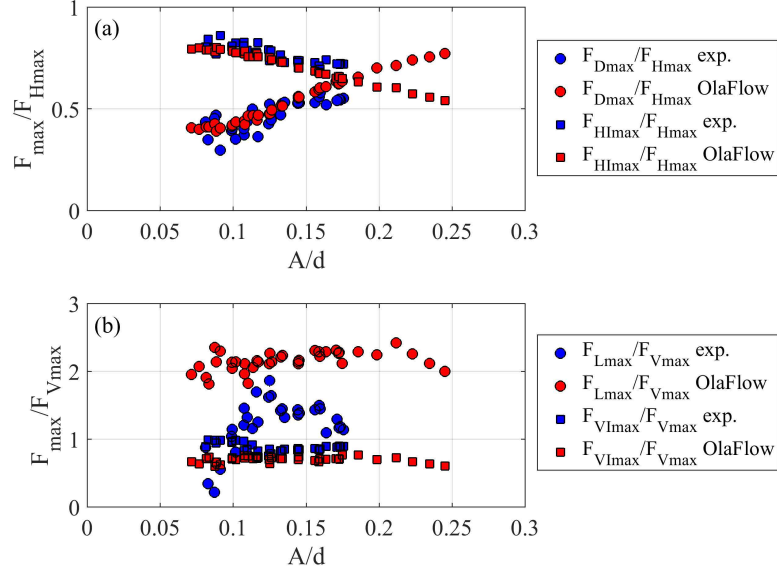

Figure 6.37: *(a) Peaks of Morison force components deduced from experiments and OlaFlow vs. A/d (e/D = 0.5): drag F_{Dmax} and inertia F_{HImax} ; (b) Peaks of transverse force components deduced from experiments and OlaFlow vs. A/d (e/D = 0.5): lift F_{Lmax} and inertia F_{VImax}.*

Similarly to the previous cases (e/D = 0.5 and 1), Figs. 6.38a and 6.38b illustrate the comparisons between the time history of the experimental and OlaFlow horizontal force and that calculated by the calibrated Morison scheme through the corresponding inertia and drag force components for the test no. 28C (e/D = 0.25). For the same test case, Figs. 6.38c and 6.38d show the comparisons between the time history of the experimental and OlaFlow vertical force, and that calculated by the transverse scheme with the related inertia and modified lift force components. As regards the horizontal force, like in the previous case (see Figs. 6.36a and 6.36b), the Morison model is able to well reproduce the time variation of F_H. Differently, the transverse model, considering the Eq. 3.7, does not correctly reproduce the time variation of the vertical force. For this reason, like previously mentioned, a new formulation of lift force was proposed (see Eq. 3.16). Indeed, observing the Figs. 6.38c and 6.36d a good correspondence between the new semi-empirical equation and the experimental and numerical variation of the vertical force can be noticed. Except for the negative peak of the vertical force, that however results very small, the comparison between the positive peaks of the vertical force is very satisfactory using the modified lift force calibrated both experimentally and numerically. The occurrence of the maximum vertical force is given by the prevalence of the lift force which is forward shifted with respect to the solitary wave crest.
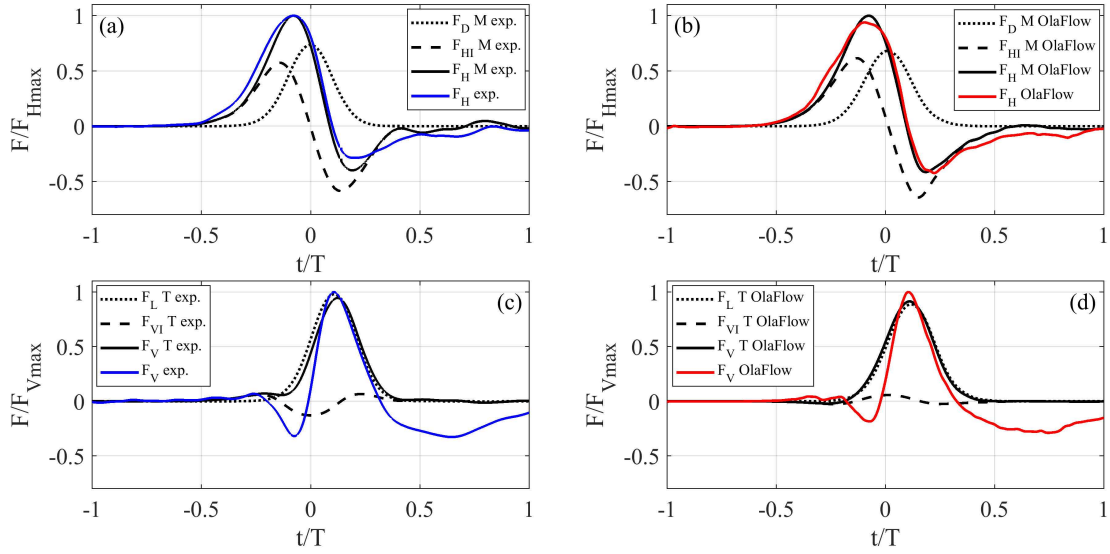
Figure 6.38: *Time variation of hydrodynamic forces calculated by semi-empirical equations, experiments and OlaFlow (e/D = 0.25, test no. 28C). (a) Comparison between experimental F_H and Morison $F_D M$, $F_{HI} M$ and $F_H M$ calibrated by experiments; (b) Comparison between numerical F_H and Morison $F_D M$, $F_{HI} M$ and $F_H M$ calibrated by OlaFlow; (c) Comparison between experimental F_V and transverse $F_L T$, $F_{VI} T$ and $F_V T$ calibrated by experiments; (d) Comparison between numerical F_V, and transverse $F_L T$, $F_{VI} T$ and $F_V T$ calibrated by OlaFlow.*

Considering all the 28 experimental tests (see Tab. 4.3) and the 36 numerical simulations performed by the OlaFlow model, a comparison between the weight of the different force components is shown in Fig. 6.39. The trends of the weight of the peak of the different components of the horizontal force present a similar behavior to the case of $e/D = 0.5$. The weight of F_{Dmax} with respect to F_{Hmax} tends to grow with the increasing of A/d (from 35% to 80%), while the weight of F_{HImax} with respect to F_{Hmax} tends to decrease (from 82% to 50%). The two force components reach the same magnitude for a value of A/d about equal to 0.16. As regards the peaks of the vertical loads (Fig. 6.39b), the major role is linked to the maximum lift force, F_{Lmax}. The lift component ranges from approximately 100% to 90% while the inertia component ranges from 0% to 20%. It can be observed that the numerical trend is more stable than the experimental one.
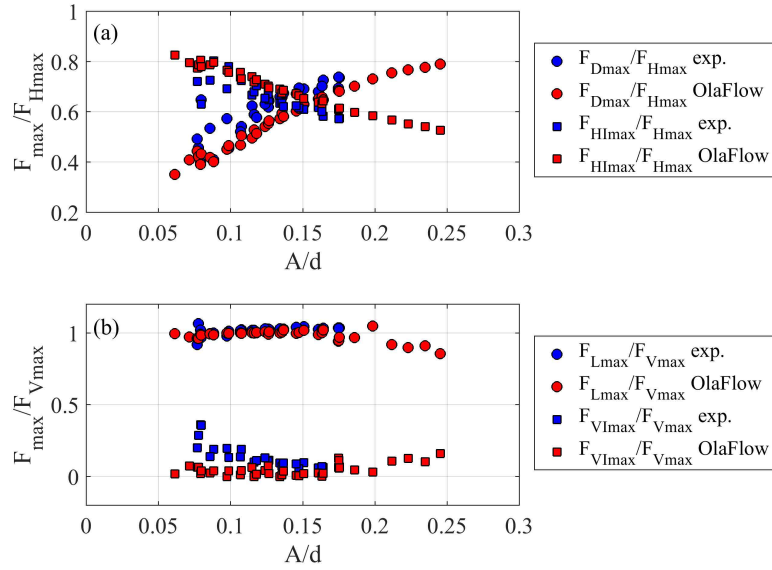
Figure 6.39: *(a) Peaks of Morison force components deduced from experiments and OlaFlow vs. A/d $(e/D = 0.25)$: drag F_{Dmax} and inertia F_{HImax}; (b) Peaks of transverse force components deduced from experiments and OlaFlow vs. A/d $(e/D = 0.25)$: lift F_{Lmax} and inertia F_{VImax}.*

For the case of $e/D = 0.1$, the Morison and transverse semi-empirical equations calibrated by experimental and numerical values of the hydrodynamic coefficients are displayed in the time domain to analyze the feature of the different force components. Fig. 6.40, shows, for the representative test case no. 29D, how to change the drag, the horizontal inertia, the lift and the vertical inertia at the passage of the solitary wave on the horizontal cylinder. A good agreement between the semi-empirical equations and the experimental and numerical simulations is noticed. With reference to the horizontal positive peak, the difference between the F_H and the $F_H M$ is negligible both experimentally and numerically. For this test, the positive peak of the horizontal inertia component results slightly higher with respect to the drag one. As concerns the vertical force, Figs. 6.40c and 6.40d illustrate the application of the transverse model with the new formulation of lift force. The vertical force mainly depends on the lift component and the vertical inertia gives a very low contribution to model this load. As with the other depths, the weight of the force components as a function of A/d is shown in Fig. 6.41. It is clear that the peaks of the horizontal inertia are higher compared to the drag ones for almost the whole range of A/d. In particular, the peaks of the inertia force tend to reduce (from 80% to 65%) with the increasing of the wave amplitude, while the peaks of the drag force tend to increase (from 40% to 70%). Only for the higher values of A/d, the drag component results slightly higher than the inertia one. The weight of the vertical force component is displayed in Fig. 6.41b. The peaks of the transverse force components deduced from experiments and the OlaFlow simulations show a higher weight of the lift force for all the range of A/d. Specifically, the weight of the lift peak ranges between about 100% to 60% while the weight of F_{VImax} ranges from 0% to 40%. However, a reduction of the peaks of lift component and a consequent rise of the maximum inertia force for $A/d > 0.15$ can be observed.
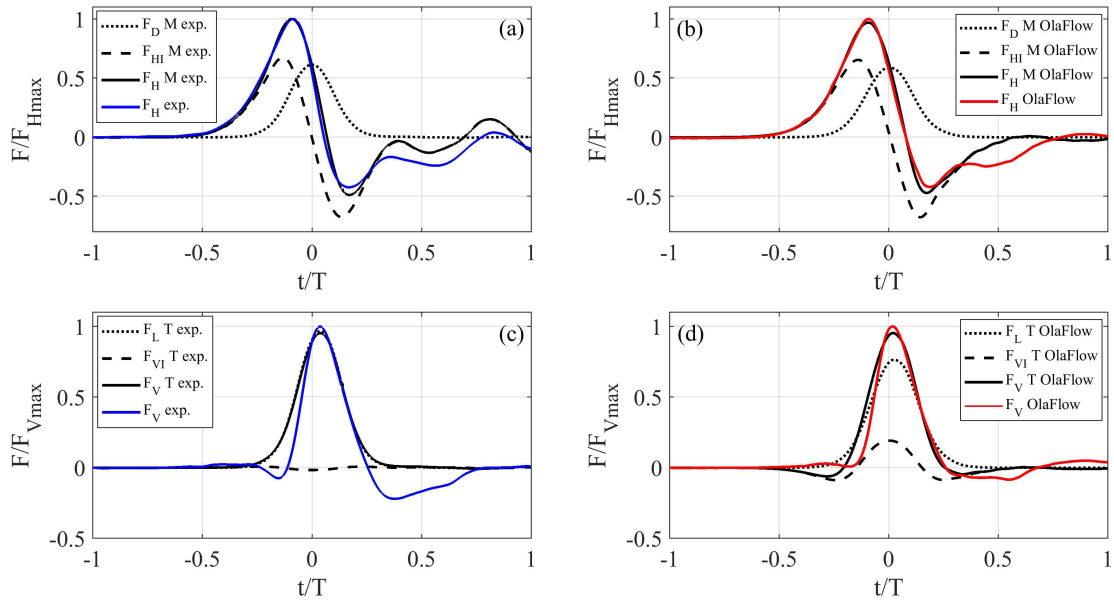
Figure 6.40: *Time variation of hydrodynamic forces calculated by semi-empirical equations, experiments and OlaFlow (e/D = 0.1, test no. 29D). (a) Comparison between experimental F_H and Morison $F_D M$, $F_{HI} M$ and $F_H M$ calibrated by experiments; (b) Comparison between numerical F_H and Morison $F_D M$, $F_{HI} M$ and $F_H M$ calibrated by OlaFlow; (c) Comparison between experimental F_V and transverse $F_L T$, $F_{VI} T$ and $F_V T$ calibrated by experiments; (d) Comparison between numerical F_V, and transverse $F_L T$, $F_{VI} T$ and $F_V T$ calibrated by OlaFlow.*

Figure 6.41: *(a) Peaks of Morison force components deduced from experiments and OlaFlow vs. A/d (e/D = 0.1): drag F_{Dmax} and inertia F_{HImax}; (b) Peaks of transverse force components deduced from experiments and OlaFlow vs. A/d (e/D = 0.1): lift F_{Lmax} and inertia F_{VImax}.*

On the basis of the previous investigations, also in the case where the cylinder is placed on the bottom, the Morison and transverse semi-empirical equations are applied to model the horizontal and vertical loads. The feature of the different force compo-

nents in both the directions are shown in Fig. 6.42 for test number 30E. An overall good agreement between semi-empirical methods, experiments and OlaFlow simulations is noticed. This is evident particularly for the maximum positive peak of the horizontal and vertical force modeled by the Morison and transverse scheme. It can be noted that the horizontal force is dominated by the inertia contribution depending on the undisturbed horizontal acceleration if compared to the drag, which is related to the free stream horizontal velocity. The vertical force field is conversely dominated by the lift force and the effect of the vertical inertia is linked to a lowering of the former contribution to give the modeling of the vertical load. In general, the shape of the vertical force follows that related to the ambient horizontal velocity in which the peak is substantially in phase with the surface elevation. Owing to the presence of spurious trailing waves, it is also possible to observe a low contribution of a positive vertical load in its final part that is not modeled by the transverse scheme.
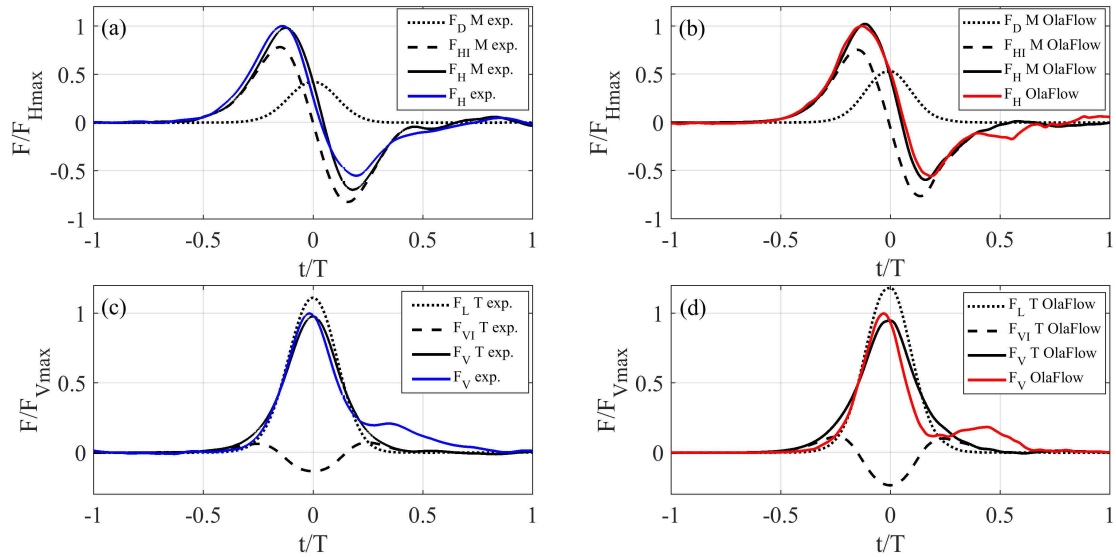
Figure 6.42: *Time variation of hydrodynamic forces calculated by semi-empirical equations, experiments and OlaFlow ($e/D = 0$, test no. 30E). (a) Comparison between experimental F_H and Morison $F_D M$, $F_{HI} M$ and $F_H M$ calibrated by experiments; (b) Comparison between numerical F_H and Morison $F_D M$, $F_{HI} M$ and $F_H M$ calibrated by OlaFlow; (c) Comparison between experimental F_V and transverse $F_L T$, $F_{VI} T$ and $F_V T$ calibrated by experiments; (d) Comparison between numerical F_V, and transverse $F_L T$, $F_{VI} T$ and $F_V T$ calibrated by OlaFlow.*

For $e/D = 0$, the four force components, i.e., F_D, F_{HI}, F_L, and F_{VI} are analysed in terms of positive and negative peaks like in the previous cases. As highlighted in Figure 6.43 as a function of A/d, the force components are weighted with respect to the corresponding maximum peak of the semi-empirical horizontal and vertical force. For the peaks of horizontal forces (see Fig. 6.43a), the inertia component ranges about from 90% for low A/d to 70% for high A/d, leading to a progressive reduction of an inertia-dominated regime and a growth of the weight of the drag up to 55%. Paying attention to the peaks of vertical loads (see Fig. 6.43b), a major role is linked to the maximum lift force, F_{Lmax}. It can be observed that the ratio between the peaks of the lift component and the total vertical one is generally greater than 1. The weight of F_{VImax} compared to the maximum vertical force is quite low. The contribution

exhibits a very small increase when A/d increases. Specifically, the values of F_{VImax} range about from 1% to 9%.
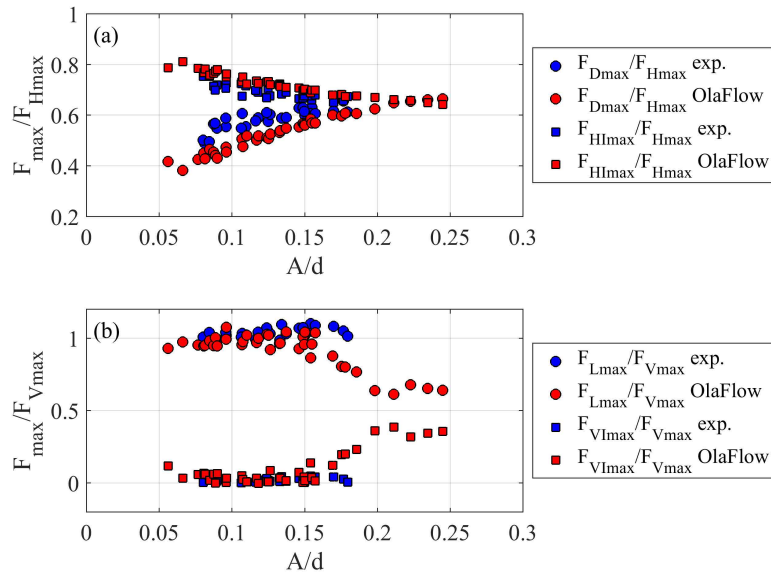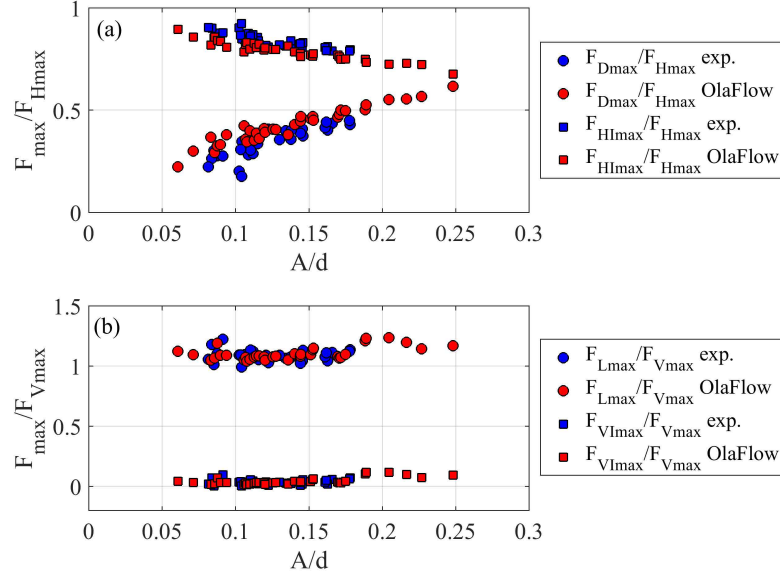

Figure 6.43: *(a) Peaks of Morison force components deduced from experiments and OlaFlow vs. A/d $(e/D = 0)$: drag F_{Dmax} and inertia F_{HImax}; (b) Peaks of transverse force components deduced from experiments and OlaFlow vs. A/d $(e/D = 0)$: lift F_{Lmax}, inertia F_{VImax}.*

6.6 Application of Gurnari and Filianoti equation

The solitary wave loads on a submerged horizontal circular cylinder are also studied by comparing the new semi-analytical method proposed by Gurnari and Filianoti with the experimental data. As mentioned in section 3.6.1, this formulation is based on the concept that a solitary wave is subjected to a slowdown passing over the cylinder. To apply the semi-analytical method, it is necessary to calibrate the horizontal hydrodynamic force (see Eq. 3.8) by calculating the speed drop factor, F_r. The experimental evaluation of F_r is possible considering the phase difference between the wave pressures using a couple of points horizontally aligned. The speed drop factor is generally defined as:

$$F_r = \frac{c_{\Delta p}}{\underline{c}_{\Delta p}} \tag{6.8}$$

The value of $c_{\Delta p}$ was deduced from the time series of surface elevations measured by the wave gauges as a function of the phase shifts and the mutual spatial locations. The obtained wave celerity in free stream conditions proved to be very close to the theoretical value given by Eq. 2.1, with a relative mean error of about 2% for all tests. With a reasonable approximation, the mentioned analytical expression of celerity was then considered in evaluating the speed drop factors. However, a slight reduction of c, probably due to the resistance offered by the side walls to the propagation of the solitary wave along the plane channel, was observed. The speeds of dynamic pressures propagating across the cylinder, $\underline{c}_{\Delta p}$, were evaluated considering the position of the six couples of transducers (Fig. 4.5d) at the same water depth located at the front and rear

side of the cylinder (1-12, 2-11, 3-10, 4-9, 5-8 and 6-7) and the related phase shift, Δt, given by the time series of recorded pressures. Owing to the variability of the speed drop factor along the vertical section of the cylinder because of the different horizontal distance of the mentioned couples of pressure sensors, the reference value of F_r for each experimental test is determined as a weighted average over all sensor positions with respect to $cos\beta$. Under this assumption, the speed drop factor for the sensors located at a greater distance have an higher weight in calculating the resulting value of F_r with respect to the couple of sensors placed at a lower distance. This is for avoiding very large speed drop factors due to the short phase shifts measured by the transducers close to the upper and lower side of the cylinder. Since three couples of transducers are placed at the same vertical position, the speed drop factor F_r results:

$$F_r = \frac{cos\frac{\pi}{12}\left(F_{r3-10} + F_{r4-9}\right) + cos\frac{\pi}{4}\left(F_{r2-11} + F_{r5-8}\right) + cos\frac{5\pi}{12}\left(F_{r1-12} + F_{r6-7}\right)}{2\left[cos\frac{\pi}{12} + cos\frac{\pi}{4} + cos\frac{5\pi}{12}\right]}$$

(6.9)

where the subscripts in the local values of F_r refer to the position of the transducers illustrated in Fig. 4.5d.

The speed drop factor obtained with the procedure above explained is respectively calculated for $e/D = 1$ and 0 and shown in Fig. 6.44 as a function of A/d. The experimental values of F_r show a slight decreasing trend when A/d increases for both cases. It is interesting to notice that the order of magnitude of F_r is comparable (on average, slightly higher) with the values of inertia coefficient, C_{MH}, in the Morison equation obtained by the same experimental dataset and numerical simulations.
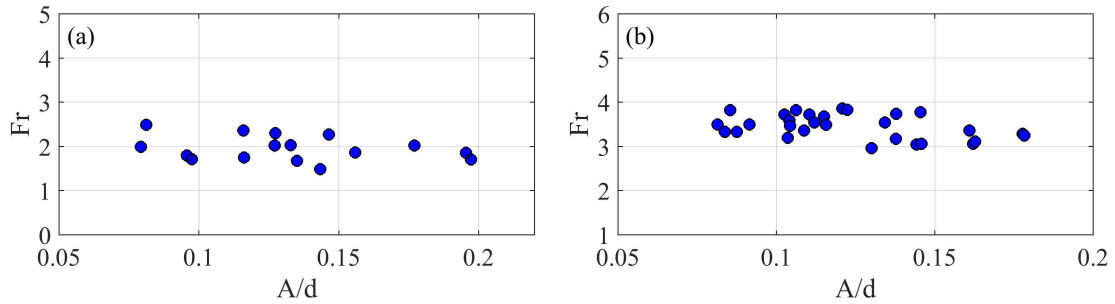

Figure 6.44: *Experimental speed drop factor Fr vs. A/d. (a) e/D = 1, (b) e/D = 0.*

After the calibration of the coefficient F_r, it is possible to apply the Gurnari and Filianoti semi-analytical model (GF2017). For two representative test cases (14A and 30E), the comparisons between the experimental horizontal force and the GF2017 equation (3.14, 3.15) are shown in Fig. 6.46. The semi-analytical model adequately follows the trend of the experimental force only for the positive values. Indeed, the experimental force exhibits a marked difference between maximum and minimum, with the latter systematically lower (in absolute value) and flatter than the first. Considering the overall dynamics, we can observe that all the positive half-wave is well interpreted by the model, while, concerning the half-negative, we can observe that only the duration is comparable, being the minimum force about 4 times greater (in absolute value) than the measured value in the first case (Fig. 6.46a) and 2 times greater in the second case

(Fig. 6.46b). However, the above results can be considered satisfactory by the engineering viewpoint since the maximum horizontal peak is well modeled by the GF2017 equation.
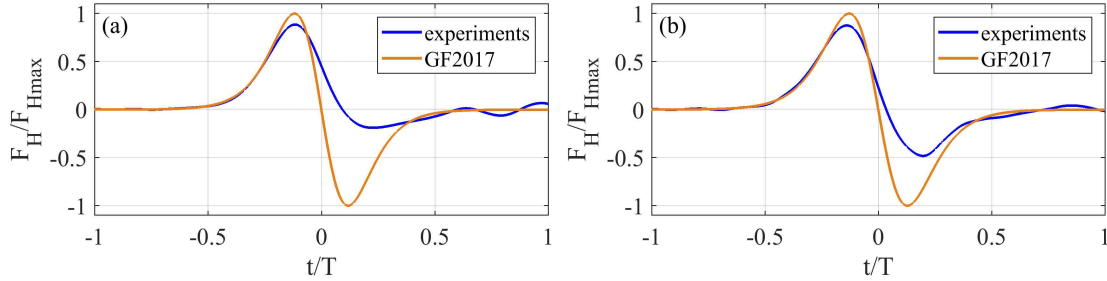

Figure 6.45: *Time variation of the experimental horizontal force and the GF2017 model. (a) test no. 14A, e/D = 1, (b) test no. 30E, e/D = 0.*

A comparison in terms of the maximum values of the horizontal force F_H between the GF2017 solution and the experiments is shown in Fig. 6.46. The values obtained in the wave flume are represented by the blue dots, while the values obtained by means of the semi-analytical model are represented by orange dots. The peaks of the present semi-empirical method were calculated using as an input the weighted average value of speed drop factor F_r obtained experimentally by Eq. 6.44 for a given value of A/d. The force peaks are normalized with respect to the maximum positive peak of the horizontal force, $F_{Hmax}*$. The general agreement is beyond initial expectations considering the simplicity of the model. In addition, to highlight the little discrepancy in term of magnitude between the experimental values and the analytical solution, Figs. 6.46c and 6.46d show the relative error for both the analyzed cases ($e/D = 1$ and $e/D = 0$). The semi-analytical model GF2017 produces a good estimate of the positive peak with a mean relative error of 10% in the case of $e/D = 1$ and a mean error of 12% in the case where the cylinder is placed on the bottom. Although the model tends to overestimate the negative peak of the horizontal force, this simplified method can be used alternatively to Morison to calculate with a good accuracy the positive peak of the horizontal force. Moreover, to apply the GF2017 it is necessary to calibrate only one coefficient which compared to the two coefficients of Morison equation represents an advantage. Nevertheless, this semi-analytical solution is suitable only to estimate the horizontal force and is not applicable to calculate the vertical one. As previously observed, when the cylinder is placed at half water depth, the weight of vertical force with respect to horizontal one reaches about 30% for the higher wave attacks. Reducing the distance between the bottom of the flume and the position of the cylinder, the vertical component tends to grow and, for the higher values of A/d, the vertical force results bigger with respect to the horizontal one. Therefore, to estimate the maximum hydrodynamic force induced by the solitary wave when the cylinder is far from the bottom, the alternative model GF2017 is applicable. If the cylinder is placed on the bottom or in proximity to it, is better to calculate the hydrodynamic forces with the classical Morison and transverse equations.
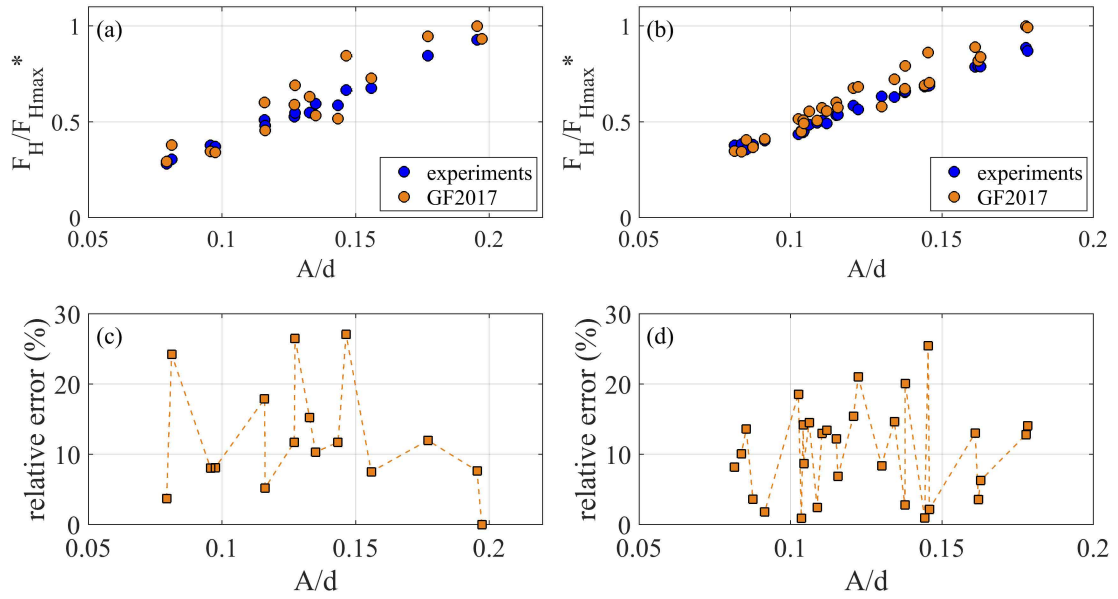
Figure 6.46: *Maximum positive peaks of experimental and GF2017 hydrodynamic forces vs. A/d. (a) e/D = 1; (b) e/D = 0; (c) relative error (e/D = 1), (d) relative error (e/D = 0).*

Conclusions

THE thesis presented a two-dimensional experimental and numerical modeling of the horizontal and vertical hydrodynamic forces induced by tsunami-like solitary waves on a horizontal circular cylinder placed at different gap-to-diameter ratios, i.e. e/D = 0, 0.1, 0.25, 0.5 and 1. By the experimental viewpoint, small-scale laboratory tests were performed in a 2D wave flume equipped with a piston-type wavemaker. Simultaneously, Lagrangian and Eulerian numerical approaches were used to simulate the experimental wave forces in a more extended range with respect to the experimental one and study the near flow field. Firstly, for e/D = 1 a diffusive weakly-compressible SPH model including a packing algorithm to avoid spurious flow field near the cylinder and a procedure to filter the raw pressure field was adopted. For the other water depths, the open source numerical model OlaFlow, based on the well-known OpenFOAM solver, was applied, enabling a less time consuming compared to SPH.

On the basis of the experimental and numerical results in the involved flow regime (A/d ranging from about 0.05 to 0.25, Re of order of 10^4 and low KC numbers), the peaks and the shapes of the total wave forces in both directions were influenced by different force components as a function of e/D. For e/D = 1, the wave loads were largely influenced by the inertia components and the maximum vertical loads showed values ranging from 14% to 27% of those of the maximum horizontal loads and therefore quite smaller for stability analysis purposes. The deviation from a fully inertia regime due to the occurrence of the contributions of drag and lift forces, representative of all adopted water depths, was highlighted for e/D = 1 through SPH by the occurrence of a pair of asymmetric vortices behind the cylinder after the passage of the solitary wave crest. For the other gap-to-diameter ratios, the resulting horizontal force was still strongly influenced by the inertia component proportional to the horizontal acceleration, even if a significant contribution of the drag force was observed when the cylinder is near the bottom and for high values of A/d. At the same time, the vertical force was characterized by a relevant contribution of the lift force when the cylinder was placed near the bottom or, in particular, attached to it. The shape of the vertical force strongly changes from e/D = 1 and e/D = 0. Indeed, for e/D = 1 it resembles the shape of the

vertical acceleration, while for $e/D = 0$ it follows the shape of the horizontal velocity. Moreover, the weight of the vertical force compared to the horizontal one tends to grow when e/D tends to 0 and for high values of A/d. A forward shift of the vertical loads was noticed for the cases of e/D equal to 0.1 and 0.25.

The good agreement between laboratory experiments and numerical simulations in terms of incident flow field (surface elevation at the vertical section of the cylinder and free stream kinematic field at the transversal axis of the cylinder) and wave loads allowed the calibration of the hydrodynamic coefficients. These parameters, representative of the flow field around the cylinder, are involved in the canonical Morison and transverse equations, and in the new semi-empirical models, i.e. the modified lift equation for $e/D = 0.1$ and 0.25, and the GF2017 equation for the horizontal loads. Paying attention to the peaks of the wave loads and the related phase shifts, the calibration of the Morison and transverse formulas has been executed using the weighted least square method with $k = 1$ and through a weighted average of the dynamic pressures for the GF2017 model.

With the aim of giving practical indications for the stability analysis of horizontal cylinders placed in marine areas subjected to seismic risk, the analysis of the hydrodynamic coefficients, i.e. C_D, C_L, C_{MH} and C_{MV}, showed particular features on the basis of A/d and e/D. For $e/D = 1$, C_D initially increases and then decreases when A/d increases, while C_{MH}, C_L and C_{MV} tend conversely to decrease. A general decrease proportionally to A/d was noticed for C_{MH}, while C_D, C_L and C_{MV} showed an inverse tendency for $e/D = 0.5$. For $e/D = 0.25$, the inertia coefficients decreases when A/d increases, C_D increases, while C_L shows an initial increase followed by a successive decrease. For $e/D = 0.1$, C_D and C_L increases proportionally to A/d, C_{MH} decreases, while C_{MV} is characterized by an initial increase and a successive decrease. For the last depth, i.e. $e/D = 0$, C_D and C_{MV} tend to rise when A/d increases, while C_{MH} and C_L present an inverse feature. In reference to the calibrated speed drop factor, F_r, in the GF2017 formula, this coefficient tends to decrease when A/d increases. The order of magnitude of F_r is comparable with the values of C_{MH} in the Morison equation. For all the investigated depths of the cylinder, the application of Morison, transverse and GF2017 schemes led to a good assessment of the maximum peaks and the associated phase shifts of the horizontal and vertical hydrodynamic forces with errors less that 10% both through the experiments and the numerical simulations.

Further experimental and numerical investigations will deal with the study of solitary wave forces at cylinders placed close the free surface and at submerged barriers with square and rectangular section.

Associated Publications

- Tripepi, G., "An experimental study on solitary waves forces at horizontal cylinder". *PhD Days di Ingegneria delle acque*, Napoli, 4-6 Luglio, 2016.

- Aristodemo, F., Tripepi, G., Meringolo, D.D., Veltri, P., De Napoli, F., "Numerical and experimental study of solitary waves on horizontal cylinders". *XXXV Convegno Nazionale di Idraulica e Costruzioni Idrauliche*, Bologna, 14-16 Settembre, 2016.

- Veltri, P., Aristodemo, F., Tripepi, G., "Impatto di onde di tsunami su strutture cilindriche sommerse". *XXXVIII Corso di aggiornamento in tecniche per la difesa del suolo e dall'inquinamento*, Guardia Piemontese Terme, 22 Marzo, 2017.

- Tripepi, G., Aristodemo, F., Veltri, P., Pace, C., Solano, A., Giordano, C., "An experimental and numerical investigation of tsunami-like waves on horizontal circular cylinders". *36th International Conference on Ocean, Offshore & Arctic Engineering (OMAE)*, Trondheim (Norvegia), June 25-30, 2017.

- Filianoti, P., Aristodemo, F., Tripepi, G., Gurnari, L., "Wave flume tests to check a semi-analytical method for calculating solitary wave loads on horizontal cylinders". *36th International Conference on Ocean, Offshore & Arctic Engineering (OMAE)*, Trondheim (Norvegia), June 25-30, 2017.

- Aristodemo F., Tripepi G., Meringolo D.D., Veltri P., "Solitary wave-induced forces on horizontal circular cylinders: Laboratory experiments and SPH simulations". *Coastal Engineering* vol. 129 pgs. 17-35, 2017.

- Tripepi, G., Aristodemo, F., Veltri., "On-bottom stability analysis of cylinders under tsunami-like solitary waves". *Water* vol. 10 (4), 487, 2018.

- Tripepi, G., Aristodemo, F., Algieri Ferraro, D., Veltri, P., De Napoli, F., "Solitary waves loads at bottom-mounted cylinders". *XXXVI Convegno Nazionale di Idraulica e Costruzioni Idrauliche*, Ancona, 12-14 Settembre, 2018.

- Aristodemo, F., Tripepi, G., Algieri Ferraro, D., Veltri, P., "Experimental and numerical modeling of solitary wave forces on horizontal cylinders near the bed".

29th International Ocean and Polar Engineering Conference (ISOPE), Honolulu, Hawaii (USA), June 16-21, 2019 (Abstract submitted).

- Aristodemo, F., Tripepi, G., Algieri Ferraro, D., Veltri, P., "An experimental and numerical study on solitary wave loads at cylinders near the bed". *Ocean Engineering*, 2019 (Paper submitted).

Bibliography

[1] Altomare, C., Domínguez, J.M., Crespo, A.J.C., González-Cao, J., Suzuki, T., Gómez-Gesteira, M., Troch, P. Long-crested wave generation and absorption for sph-based dualsphysics model. *Coastal Engineering*, 127:37–54, 2017.

[2] Antuono, M., Colagrossi, A., Marrone, S. Numerical diffusive terms in weakly-compressible sph schemes. *Comput. Phys. Commun.*, 183:2570–2580, 2012.

[3] Antuono, M., Colagrossi, A., Marrone, S., Molteni, D. Free-surface flows solved by means of SPH schemes with numerical diffusive terms. *Computer Physics Communications*, 181:532–549, 2010.

[4] Aristodemo, F., Meringolo, D.D., Groenenboom, P., Lo Schiavo, A., Veltri, P., Veltri, M. Assessment of dynamic pressures at vertical and perforated breakwaters through diffusive sph schemes. *Math. Prob. Eng.*, (ID 305028):1–10, 2015.

[5] Aristodemo, F.; Tomasicchio, G.R.; Veltri, P. Modelling of periodic and random wave forces on submarine pipelines. *In Proceedings of the 25th International Conference on Mechanics and Arctic Engineering, Hamburg, Germany*, pages 1–10, 2006.

[6] Aristodemo, F., Tomasicchio, G.R., Veltri, P. New model to determine forces at on-bottom slender pipelines. *Coast. Eng.*, 58:267–280, 2011.

[7] Aristodemo, F., Tomasicchio, G.R., Veltri, P. Wave and current forces at a bottom-mounted submarine pipeline. *J. Coast. Res.*, 65:153–158, 2013.

[8] Belytschko, T., Krongauz, Y., Dolbow, J., Gerlach, C.,. On the completeness of meshfree particle methods. *Int. J. Numer. Methods Eng.*, 43:785–819, 1998.

[9] Boccotti, P. *Wave Mechanics for Ocean Engineering*. Elsevier, 2000.

[10] Bouscasse, B., Colagrossi, A., Marrone, S., Souto-Iglesias, A. Sph modelling of viscous flows past a circular cylinder interacting with a free surface. *Comput. Fluids*, 146:190–212, 2017.

[11] Boussinesq, M.J. *Théorie de l'intumescence liquide, appelée onde solitaire ou de translation, se propageant dans un canal rectangulaire.* C.R. Acad. Sci., 72, 1871.

[12] Boussinesq, M.J. *Essai sur la theorie des eaux courantes*. Memoires presentes par divers savants a l'Academie des Sciences de l'Institut National de France, XXIII, 1877.

[13] Bryndum, M.B., Jacobsen, V., Brand, L.P. Hydrodynamic forces from wave and current loads on marine pipelines. *Offshore Technology Conference, Houston, Paper OTC 4454*, pages 95–102, 1983.

[14] Bryndum, M.B., Jacobsen, V., Tsahalis, D.T. Hydrodynamic forces on pipelines: Model tests. *J. Offshore Mech. and Arctic Eng.*, 114:231–241, 1992.

[15] Chakrabarti, S.K. *Hydrodynamics of offshore structures*. Computational Mechanics Publications, Springer Verlag, 1987.

[16] Cheong, H.F., Jothi-Shankar, N., Subbiah, K. Inertia dominated forces on submarine pipelines near seabed. *J. Hydraul. Res.*, 27(1):5–22, 1989.

[17] Chevalier, C.; Lambert, E.; Bélorgey, M. Efforts sur une conduite sous-marine en zone côtière. *Revue Française de Génie Civil*, 5:995–1014, 2001.

[18] Colagrossi, A., Bouscasse, B., Antuono, M., Marrone, S. Particle packing algorithm for sph schemes. *Comput. Phys. Commun.*, 183:1641–1653, 2012.

[19] Colagrossi, A., Landrini, M. Numerical simulation of interfacial flows by smoothed particle hydrodynamics. *J. Comp. Phys.*, 191:448–475, 2003.

[20] Crespo, A.J.C., Altomare, C., Domínguez, J.M., González-Cao, J., Gómez-Gesteira, M. Towards simulating floating offshore oscillating water column converters with smoothed particle hydrodynamics. *Coast. Eng.*, 126:11–26, 2017.

[21] Daily J.W., Stephan S.C. The solitary wave: its celerity, internal velocity and amplitude attenuation in a horizontal smooth channel. *Proc. 3rd Conf. Coastal Eng.*, pages 13–30, 1952.

[22] Di Risio, M., De Girolamo, P., Bellotti, G., Panizzo, A., Aristodemo, F., Molfetta, M.G., Petrillo, A.F. Landslide-generated tsunamis runup at the coast of a conical island: New physical model experiments. *J. Geophys. Res.-Oceans*, 114(C1):1–16, 2009.

[23] Dingemans, M.W. *Water Wave Propagation Over Uneven Bottoms*. Advanced Series on Coastal Engineering, World Scientific, 1997.

[24] Farge, M. Wavelet transforms and their applications to turbulence. *Annu. Rev. Fluid Mech.*, 24:395–458, 1992.

[25] Filianoti, P., Aristodemo, F., Tripepi, G., Gurnari, L. Wave flume test to check a semi-analytical method for calculating solitary wave loads on horizontal cylinders. *Proceedings of the 36th International Conference on Ocean, Offshore and Arctic Engineering, Trondheim, Norway*, pages 25–30, 2017.

[26] Filianoti, P., Di Risio, M. Solitary wave loads on submerged breakwater: laboratory tests. *Proc. of 22nd Int. Offshore and Polar Engineering Conf., Rhodes*, pages 1–6, 2012.

[27] Filianoti, P., Piscopo, R. On the tsunami wave-submerged breakwater interaction. *Proceedings of MERCEA, Seismic Engineering International Conference commemorating the 1908 Messina and Reggio Calabria Earthquake*, pages –, 2008.

[28] Franklin, G.F., Powell, D.J., Emami-Naeini, A. Feedback control of dynamic systems. *4th ed. Upper Saddle River, NJ, Prentice Hall PTR*, pages –, 2001.

[29] Goring, D.G. *Tsunamis - The propagation of long waves onto a shelf.* PhD thesis, California Institute of Technology, 1978.

[30] Grace, R.A.; Zee, G.T.Y. Wave forces on rigid pipes using ocean test data. *J. Waterw. Port Coast. Ocean Eng.*, 107:71–92, 1981.

[31] Gsell, S., Bonometti, T., Astruc, D. A coupled volume-of-fluid/immersed-boundary method for the study of propagating waves over complex-shaped bottom: Application to the solitary wave. *Comput. Fluids*, 131:56–65, 2016.

[32] Guizien, K., Barthélemy, E. Accuracy of solitary wave generation by a piston wave maker. *J. Hydraul. Res.*, 40(3):321–331, 2002.

[33] Gurnari, L., Filianoti, P. A semi-analytical model to calculate forces exerted on horizontal cylinder by a solitary wave. *Proc. of 36th Int. Conf. on Ocean, Offshore and Arct. Eng., Trondheim, Norway*, pages 1–8, 2017.

[34] Higuchi, H., Lewalle, J., Crane, P. On the structure of a two-dimensional wake behind a pair of flat plates. *Phys. Fluids*, 6(1):297–305, 1994.

[35] Higuera, P. *Application of computational fluid dynamics to wave action on structures.* PhD Thesis, University of Cantabria, 2015.

[36] Higuera, P., Lara, J.L., Losada, I.J., . Simulating coastal engineering processes with openfoam. *Coastal Engineering*, 71:119–134, 2013.

[37] Higuera, P., Lara, J.L., Losada, I.J. Three-dimensional interaction of waves and porous coastal structures using openfoam Ⓡ. part i: Formulation and validation. *Coastal Engineering*, 83:243–258, 2014.

[38] Honji, H. Streaked flow around an oscillating circular cylinder. *J. Fluid Mech.*, 107:509–520, 1981.

[39] Huang, C.-J., Dong, C.-M. On the interaction of a solitary wave and a submerged dike. *Coast. Eng.*, 43:265–286, 2001.

[40] Justesen, P. Hydrodynamic forces on large cylinders in oscillatory flows. *J. Waterw. Port Coast. Ocean Eng.*, 115(4):497–514, 1989.

[41] Korteweg, D.J., de Vries, G. On the change of form of long waves advancing in a rectangular canal, and on a new type of long stationary waves. *Philosophical Magazine Series*, 39(240):422–443, 1895.

[42] Lee, J.J., Skjelbreia, J.E., Raichlen, F. Measurements of velocities in solitary waves. *J. Waterw. Port Coast. Ocean Eng.*, 108:200–218, 1982.

[43] Lin, M.Y., Liao, G.Z. Vortex shedding around a near-wall circular cylinder induced by a solitary wave. *J. Fluids Struct.*, 58:127–151, 2015.

[44] Longoria, R.G., Beaman, J.J., Miksad, R.W. An experimental investigation of forces induced on cylinder in random oscillatory flow. *J. Offshore Mech. Arct. Eng.*, 113:275–285, 1991.

[45] Lynett, P.J., Liu, P.L.F., Losada, I.J., Vidal, C. Solitary wave interaction with porous breakwater. *J. Waterw. Port Coast. Ocean Eng.*, 126(6):314–322, 2000.

[46] Madsen, P.A.Fuhrman D.R., Schäffer H.A. On the solitary wave paradigm for tsunamis. *J. Geophys. Res.*, 113(C12012):1–22, 2008.

[47] Marrone, S., Antuono, M., Colagrossi, A., Colicchio, G., Le Touzé. δ-SPH model for simulating violent impact flows. *Computer Methods in Applied Mechanics and Engineering*, 200:1526–1542, 2011.

[48] Marrone, S., Colagrossi, A., Antuono, M., Colicchio, G., Graziani, G. An accurate sph modeling of viscous flow around bodies at low and moderate reynolds numbers. *J. Comp. Phys.*, 245:456–475, 2013.

[49] Mattioli, M.; Mancinelli, A.; Brocchini, M. Experimental investigation of the wave-induced flow around a surface-touching cylinder. *J. Fluids Struct.*, 37:62–87, 2013.

[50] Meringolo, D.D., Aristodemo, F., Veltri, P. Sph numerical modeling of wave-perforated breakwater interaction. *Coast. Eng.*, 101:48–68, 2015.

[51] Meringolo, D.D., Colagrossi, A., Marrone, S., Aristodemo, F. On the filtering of acoustic components in weakly-compressible sph simulations. *J. Fluids Struct.*, 70:1–23, 2017.

[52] Molteni, D., Colagrossi, M. A simple procedure to improve the pressure evaluation in hydrodynamic context using the sph. *Comput. Phys. Commun.*, 180:861–872, 2009.

[53] Monaghan, J.J. Simulating free surface flows with sph. *J. Comp. Phys.*, 110:399–406, 1994.

[54] Morison, J.R., O'Brien, M.P., Johnson, J.W., Schaaf, S.A. The forces exerted by surface waves on piles. *Petroleum Trans.*, 189:149–156, 1950.

[55] Neill, I.A.R.; Hinwood, J.B. Wave and wave-current load on a bottom-mounted circular cylinder. *Int. J. Offshore Polar*, 2:122–129, 1998.

[56] O'Dwyer, A. *Handbook of PI and PID Controllers Tuning Rules*. 3rd ed. Covent Garden, Imperial College, 2009.

[57] Qu, K., Ren, X.Y., Kraatz, S., Zhao, E.J. Numerical analysis of tsunami-like wave impact on horizontal cylinders. *Ocean Engineering*, 145:316–333, 2017.

[58] Quinlan, N.J., Basa, M., Lastiwka, M. Truncation error in mesh-free particle methods. *Int. J. Numer. Methods Eng.*, 66:2064–2085, 2006.

[59] Rayleigh, L. *On waves*. Phil. Mag., 1, 1876.

[60] Romano, A., Guerrini, M., Bellotti, G., Lie-hong, J. Laboratory generation of solitary waves: an inversion technique to improve available methods. *China Ocean Eng.*, 28:57–66, 2014.

[61] Russel, J.S. Report on waves. *Proc. 14th Meeting, Brit. Ass. Adv. Sci.*, pages 311–390, 1845.

[62] Sarpkaya, T., Isaacson, M. *Mechanics of Wave Forces on Offshore Structures*. Van Nostrand Reinhold Company, 1981.

[63] Sarpkaya, T.; Rajabi, F. Hydrodynamic drag on bottom-mounted smooth and rough cylinders in periodic flow. *In Proceedings of the 11th Annual Offshore Technology Conference, Houston, TX, USA*, pages 219–226, 1980.

[64] Schimmels, S.; Sriram, V.; Didenkulova, I. Tsunami generation in a large scale experimental facility. *Coast. Eng.*, 110:32–41, 2016.

[65] Seiffert, B., Hayatdavoodi, M., Ertekin, R.C. Experiments and computations of solitary-wave forces on a coastal-bridge deck. part i: Flat plate. *Coast. Eng.*, 88:194–209, 2014.

[66] Seo, S., Mun, H., Lee, J., Kim, J. Simplified analysis for estimation of the behavior of a submerged floating tunnel in waves and experimental verification. *Marine Structures*, 44:142–158, 2015.

[67] Sibley, P., Coates, I.E., Arumugam, K. Solitary wave forces on horizontal cylinders. *Appl. Ocean Res.*, 4(2):113–117, 1982.

[68] Skorpa, L. Developing new methods to cross wide and deep norwegian fjords. *Procedia Engineering*, 4:81–89, 2010.

[69] Sumer, B.M., Fredsoe, J. *Hydrodynamics around cylindrical structures*. Advanced Series on Coastal Engineering, World Scientific, 2006.

[70] Sumer, B.M., Jensen, B.L., Fredsoe, J. Effect of a plane boundary on oscillatory flow around a circular cylinder. *J. Fluid Mech.*, 225:271–300, 1991.

[71] Sumer, B.M., Kozakiewicz, A. Visualization of flow around cylinders in irregular waves. *International Journal of Offshore and Polar Engineering*, 5(4):270–272, 1995.

[72] Sun, J.L., Wang, C.Z., Wu, G.X., Khoo, B.C. Fully nonlinear simulations of interactions between solitary waves and structures based on the finite element method. *Ocean Eng.*, 108:202–215, 2015.

[73] Sun, P., Ming, F., Zhang, A. Numerical simulation of interactions between free surface and rigid body using a robust sph method. *Ocean Eng.*, 98:32–49, 2015.

[74] Torrence, C., Compo, G.P. A practical guide to wavelet analysis. *Bull. Am. Meteorol. Soc.*, 79:61–78, 1998.

[75] Violeau, D., Rogers, B.D. Smoothed particle hydrodynamics (sph) for free-surface flows: past, present and future. *J. Hydraul. Res.*, 54(1):1–26, 2016.

[76] Wei, Z., Dalrymple, R., Hérault, A., Bilotta, G., Rustico, E., Yeh, H. Sph modeling of dynamic impact of tsunami bore on bridge piers. *Coast. Eng.*, 104:26–42, 2015.

[77] Wei, Z., Dalrymple, R.A. Numerical study on mitigating tsunami force on bridges by an sph model. *J. Ocean Eng. and Marine Energy*, 2(3):365–380, 2016.

[78] Williamson, C.H.K. Sinusoidal flow relative to circular cylinders. *J. Fluid Mech.*, 155:141–174, 1985.

[79] Wolfram, J., Naghipour, M. On the estimation of morison force coefficients and their predictive accuracy for very rough circular cylinders. *Appl. Ocean Res.*, 21:311–328, 1999.

[80] Wu, N-J., Tsay, T.-K., Chen, Y.-Y. Generation of stable solitary waves by a piston-type wave maker. *Wave Motion*, 51:240–255, 2014.

[81] Xiao, H., Huang, W., Tao, J., Liu, C. Numerical modeling of wave-current forces acting on horizontal cylinder of marine structures by vof method. *Ocean Eng.*, 67:58–67, 2013.

[82] Zhao, M., Cheng, L., Teng, B. Numerical simulation of solitary wave scattering by a circular cylinder array. *Ocean Eng.*, 34:489–499, 2007.